論文 / 著書情報
Article / Book Information

題目(和文)	超広帯域双方向チャネルサウンダを用いた屋内電波伝搬特性の実験的解析およびモデル化
Title(English)	Experimental analysis and modeling of indoor radio wave propagation using ultra wideband double-directional channel sounder
著者(和文)	羽田勝之
Author(English)	katsuyuki haneda
出典(和文)	学位:博士（工学）, 学位授与機関:東京工業大学, 報告番号:甲第6841号, 授与年月日:2007年3月26日, 学位の種別:課程博士, 審査員:
Citation(English)	Degree:Doctor of Engineering, Conferring organization: Tokyo Institute of Technology, Report number:甲第6841号, Conferred date:2007/3/26, Degree Type:Course doctor, Examiner:
学位種別(和文)	博士論文
Type(English)	Doctoral Thesis

Doctoral Dissertation
Experimental Analysis and Modeling of Indoor Radio Wave Propagation Using Ultra Wideband Double-Directional Channel Sounder

March 2007

Advisors Professor Jun-ichi TAKADA and
Professor Shinobu Yume YAMAGUCHI

Department of International Development Engineering
Graduate School of Engineering
Tokyo Institute of Technology
Katsuyuki HANEDA

Acknowledgment

During my study in Tokyo Tech, I am greatly obliged to Professor Jun-ichi Takada. His encouragement and invaluable comments not only as a research supervisor, but also as a personal advisor, has been the most precious and warmest input throughout my study. I also would like to express my gratitude to Professor Shinobu Yume Yamaguchi for giving me many opportunities where I could be involved in the international development project. Without the precious opportunities, I could not acquire many professional skills both as a researcher and as an educator. My sincere gratitude also goes to Japan Society for Promotion of Science for their appreciation of my research works and financial support.

I also would like to thank Professor Kiyomichi Araki, Professor Yukihiko Yamashita, and Professor Atsuhiro Nishikata as referees of my thesis to discuss the appropriateness of the contents. In order to accomplish my thesis works, my sincere gratitude also goes to Professor Takehiko Kobayashi from Tokyo Denki University for providing me a great opportunity to work in the NiCT UWB Consortium. In the Consortium, I could learn a lot with many researchers from several external institutions, such as Dr. Ken-ichi Takizawa, Mr. Iwao Nishiyama, Dr. Yuko Rikuta, and Dr. Honggang Zhang from NiCT, Dr. Makoto Yoshikawa, Mr. Naoto Takahashi, and Mr. Fumio Ohkubo from NTT-AT Corp., Mr. Takahiro Miyamoto from NEC Engineering, and Professor Ryuji Kohno, the leader of the project. I would like to thank all the members for their invaluable comments and helps both in discussions and experiment. In my early years of study, Professor Kei Sakaguchi from Tokyo Tech and Dr. Ichiro Ida from Fujitsu Ltd. encouraged me a lot in constructing fundamentals of my research works, and therefore, I would like to express my gratitude to both of them.

It was a great opportunity to get to know many European researchers in COST273 meetings, which have eventually created my carrier path in the future in Helsinki University of Technology. Among many discussions and group meetings, I especially thank Professor Pertti Vainikainen and Mr. Lasse Vuokko from Helsinki University of Technology, and Professor Andy Molisch from Lund University. The two Professors were the Chairman of sub-working group 2.3 (Channel Sounding) and 2.1 (MIMO channels) respectively, where I was actively involved in, and intensive discussions there motivated me very much.

In my daily research life, I cannot forget all the memories shared and experienced with student members in laboratories. Especially the gratitude goes to my colleagues, Dr. Kei

Mizutani, Mr. Ching Gilbert Siy, Mr. Nobuo Ooka and many others for their precious encouragement that always makes me further proceed in my research activities. I would like to thank my former colleagues, namely Mr. Atsushi Honda from Fujitsu Ltd., Mr. Wataru Hachitani from Sharp Corp., Mr. Yoshitaka Umeda from Panasonic Corp., and Professor See Ho Ting from Nangyang University for the stimulation and encouragement. My sincere gratitude also goes to secretaries of laboratories, such as Ms. Yukiko Tanaka, Ms. Eriko Ando, and Ms. Kazuyo Fujimoto for supporting my research works very much. I am really thankful to all the members whom I got to know and share the same time during my study for 9 years.

Finally, I would like to dedicate this thesis to my family, especially to my father and mother and thank them for all the time they have dedicated to me since my birth.

March 2007
Katsuyuki HANEDA

Abstract

This thesis presents an accurate and precise indoor channel measurement and modeling using a high-resolution multi-dimensional channel sounder. We introduced the concept of double-directional channels and ultra-wideband signals into the channel sounder to increase the angular and delay resolution capability, respectively. The methods also enables us to model propagation channels separately from antenna properties used in the measurements. As it is crucial to analyze, design, and optimize antenna systems in many physical layer schemes which are potential for the next generation indoor wireless systems, such as multiple-input and multiple-output and ultra-wideband systems, our results contributed to facilitate these tasks.

The main contribution of this thesis is summarized into the following three-fold: 1) development of the channel sounding and propagation modeling method which contributed to the high-resolution multi-dimensional angular-delay propagation modeling activities; 2) measurement and modeling of indoor radio channels in a Japanese wooden house to identify dominant propagation phenomena and to extract parameters that can be used in channel models; and 3) assessment of the accuracy of developed propagation modeling results for evaluation of data transmission performances. In developing the channel sounder, we incorporated the maximum-likelihood based propagation parameter extraction algorithms. The algorithm characterized measured data by a finite set of propagation paths so that the modeled results facilitates the intuititive understanding of wave propagation mechanisms. The performance of the channel sounder was assessed in an anechoic chamber, and theoretically derived performance measures such as angular and delay resolution capability were experimentally confirmed. The channel sounder was then used to measure and model actual propagation channels. The modeling of propagation paths was based on clustering approach, which is a common way in channel modeling activities. Properties of clusters were evaluated with respect to angular, delay and power aspects. The results were contributed to the COST273 channel model and approved as a parameter set representating home environment. Finally, the modeled results were used to reconstruct channel responses, and data transmission performances of ultra-wideband systems were evaluated using the channel. The results were compared with the data transmission performance derived from raw channel data, from which the channel models were developed. The comparison revealed that the modeling results were not always capable of predicting transmission performance derived from raw channel data accurately. However, further investigation revealed that the accuracy of BEP prediction improved by considering the residual components into simulations as diffuse paths. This suggested that the propagation modeling should be performed separately for discrete propagation paths and continuous multi-dimensional power angular/delay spectrum. Several important future research items are suggested at the end based on the context of this thesis.

Contents

Chapter1

Introduction

1.1 Challenges in Modeling Indoor Radio Wave Propagation

Demands for wireless system applications are tremendously increasing year by year, and innovations of technologies comprising the wireless system reflects these demands. These technologies are considered as core solutions that realize a ubiquitous world. In the near future, it is expected that every electronic equipment and a sensor surrounding us establishes wireless connection with one another, forms a wireless network, shares and exchanges data, acquires the environmental information, and finally adapts to the environment so that it provides a context-based communication system.

Nowadays the wireless network exists everywhere, different from twenty years ago when the first mobile phone came into practical use. Recently the importance of wireless networks is increasingly discussed for home security, human safety, and medical applications. Many of these applications are supposed to be achieved in indoor use. Particularly the wireless area network (WLAN) and wireless personal area network (WPAN) are the emerging short-range wireless applications in indoor scenarios. They are totally different from previous cell phone systems with respect to the communication distance. The WLAN system, represented by the IEEE802.11a/b/g standards and IEEE802.11n as future high-data rate standards [1], are practically being used with distances ranging from several meters to less than a few hundered meters. The WPAN systems are designed to cover smaller areas to the extent of several meters, and its standardization is actively being conducted by IEEE802.15 working groups [2]. The smaller coverage of indoor wireless systems is called “picocells”, and the wireless network covering small areas is called “piconets”.

In designing the wireless networks for indoor short-range communications, one should inevitably consider multipath channels. The modulated waveforms radiated from transmitters (Tx) reach the receiver (Rx) through many routes because of the interaction of propagating electromagnetic waves with scattering objects surrounding transmitting and receiving wireless terminals. Thus receiving waveforms contain many echoes leading to the distortion of transmitted waveforms and intersymbol interference. In the end, the system suffers from deterioration of bit error probability and data throughput. As the deterioration is much serious when the transmission data rate is higher than the available bandwidth, many solutions have been invented to combat this issue, such as waveform equalizers.

Normally the indoor environment reveals rich multipath scattering due to the dense surrounding objects around wireless terminals, such as wall, ceiling/floor, and furniture. In contrast to the outdoor environment where many researches have analyzed the multipath behavior, sufficient analysis have not been accumulated with regards to the indoor propagation mechanisms, mainly because 1) the needs of wireless communication in indoor environments have just started to prevail in recent years; and 2) characterizing the indoor multipath environment with sufficient resolution and accuracy is a challenging task given the dense multipath environments.

1.2 Ultra Wideband (UWB) Radio

1.2.1 Definition and Spectrum Mask of UWB Radio

Among the physical layer candidates of the indoor wireless communications, ultra wideband (UWB) radio have attracted a lot of attention due to the following advantages:

1. High data rate transmission systems;
2. Precise ranging and positioning capability [3]; and
3. Low power consumption transceivers.

Since the Federal Communication Commissions (FCC) of the USA released the microwave frequency bands to UWB applications in 2002 [4], quite many efforts have been made by researches both in UWB research and development. The UWB signal is defined either by the fractional bandwidth or absolute bandwidths of the transmitted signal as

$$\frac{2(f_\mathrm{H} - f_\mathrm{L})}{f_\mathrm{H} + f_\mathrm{L}} \times 100 > 20 \ [\%], \tag{1.1}$$

or

$$f_\mathrm{H} - f_\mathrm{L} > 500 \ [\mathrm{MHz}], \tag{1.2}$$

where f_H and f_L are the 10 dB bandwidth of the power spectrum density (PSD). They are the frequencies which give a PSD 10 dB lower than the peak PSD. Compared to the conventional wideband systems, definitions (1.1) and (1.2) inform us of the drastic change and even breakthrough in using frequency bands, which are precious resources of wireless communications. None of the existing wireless systems operated in the microwave band satisfies the definitions. The wideband code division multiple access deployed in the third generation mobile phones occupies 5 MHz bandwidths with its carrier frequency around 2 GHz, resulting in a fractional bandwidth of 0.25 %, which spans a much narrower bandwidth than UWB signals. The frequency band is densely occupied by various kinds of applications according to the present regulation, thus accommodating new systems into the frequency band is almost impossible. UWB radio can be deployed even in that situation, but coexistence with other wireless systems always becomes an important issue to avoid interference. Thus there is a strict restriction with regards to the transmission power from UWB devices.

The restriction of the power spectrum density is normally called a power spectrum mask, and is defined in each country depending on the frequency allocation for existing systems. The frequency allocation in Japan is managed by the Ministry of Internal Affair and Communications (MIC) [5]. The UWB spectrum mask in Japan, Europe and US is shown in Fig. 1.1. Since the FCC-defined spectrum mask was open to the public, modification of the FCC mask had been extensively discussed in Japan under the initiative of MIC. In the process, all institutions and private companies operating broadcasting, mobile phone, radio astronomy, and variety of radars such as planet exploration radars, meteorological radars, and radars for aircrafts and marine vehicle were involved. According to the Japanese regulation adopted on March 27 of 2006 [6], the whole frequency band was divided into low and high bands, and the 5 GHz band was not allocated for UWB systems for protection of WLAN systems operated in that band. The low and high bands span from 3.4 to 4.8 GHz and 7.25 to 10.25 GHz, respectively. The maximum radiation power is -41.3 dBm/MHz, but a functionality to avoid interference to other systems, namely detection and avoidance (DAA) is required. In the second low band occupying from 4.2 to 4.8 GHz, DAA techniques are not necessary, but the radio license for the band is allowed until the end of 2008. Outband emission is strictly prohibited to protect GPS, cellular, and other radar systems. The microwave band is allowed for indoor use only, but allocation of quasi-millimeter wave band from 24 to 29 GHz will be discussed in MIC, targeting both indoor and outdoor applications. One example of outdoor application covers collision avoidance systems for car parking. The frequency band from 100 to 960 GHz is available for UWB communications, but only in the US.

The wide frequency band larger than 500 MHz is equivalent to a short pulse range in the temporal domain narrower than 2 ns, enabling us to resolve multipaths to the extent of nanoseconds. If the full band $(3.1 - 10.6$ GHz) is used for the pulse shaping in the temporal domain, it achieves a temporal multipath resolution of 0.13 ns corresponding to 4 cm in distance. The property of UWB radio also gives robustness to waveform distortion on the receiving side because each echo is distinct with each other. Furthermore, the available wide frequency range provides inherent “built-in diversity” so that UWB systems suffer from multipath fading less severely than the conventional narrow and wideband systems [7, 8].

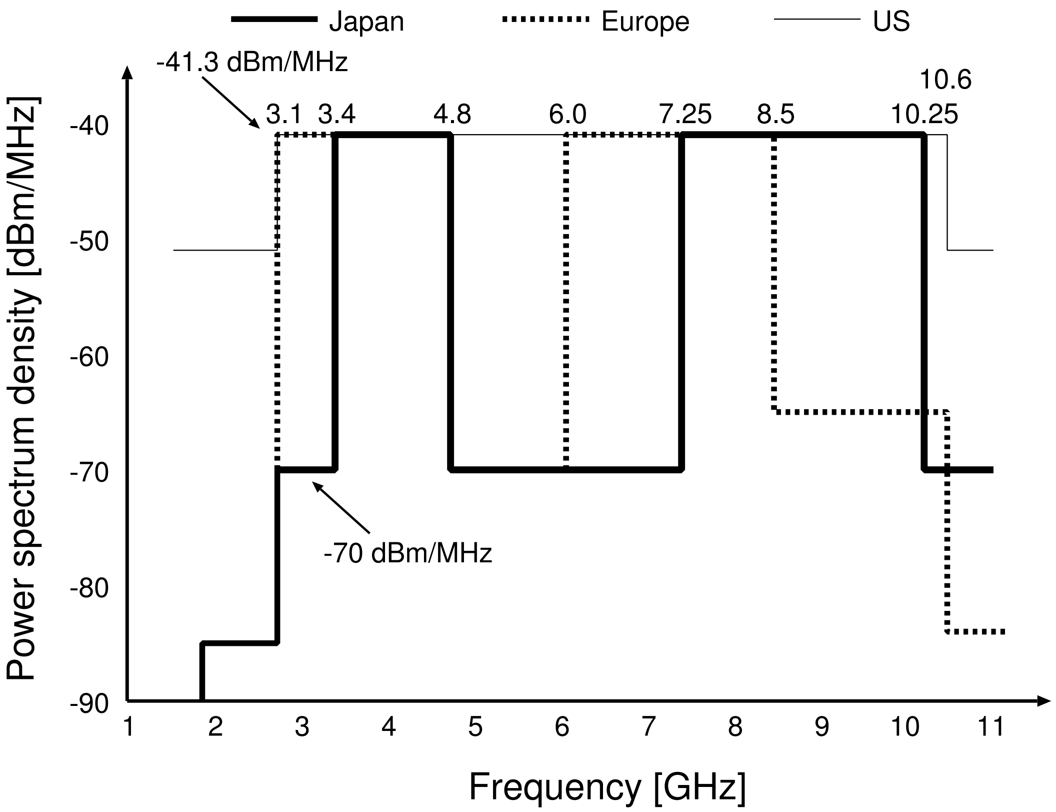

Figure 1.1 Spectrum mask for UWB in Japan, Europe, and US.

1.2.2 Application of UWB Radio

The application of UWB radio covers both high and low data rate systems. The high data rate system is mainly for realizing connection between consumer electronics, such as wireless video streaming and wireless universal serial bus (USB). Target data rate for wireless USB is as high as 480 and 100 Mbps for communication distances under 3 and 10 m, respectively. Low data rate applications can be an alternative to conventional low data rate applications, such as Bluetooth and infrared communications. The application for sensor networks are also undertaken using the low data rate specifications. One of the applications is for home security. The distributed sensors inside a room equip functionality to monitor a variety of environmental information, and form a network to share the collected data. The collected data are then integrated, often called data fusion, so that the network can respond to the environment to help the daily life of human activities. Automatic control of environment, such as temparature, brightness of the lighting, and alarm for fire and intruder are specifically taken into account [9]. As it is envisioned that the data traffic for the application is not high, the target data rate is ranging from several Mbps to kbps.

There are mainly two kinds of popular data transmission schemes in UWB communications realizing both high and low data rate transmissions: an impulse radio (IR) based technique and a multi-carrier oriented data transmission. The popular modulation formats based on the impulse radio are the direct sequence UWB (DS-UWB) [10]. The DS-UWB uses a pulse as a chip of spread sequences, accomplishing a large spreading gain over the wide bandwidth. The impulse radio based systems have a potential to realize simple transceiver architecture than the conventional carrier-based transmission schemes. Even the full-digital implementation is possible due to the simple signal generation and detection. In contrast, the multi-band orthogonal frequency division multiplexing (MB-OFDM) [11] is also widely used as a multi-carrier based transmission scheme. This scheme subdivides the bandwidths into 500 MHz so that clock speed of A/D converter can be much slower than other UWB systems. The OFDM technology has attracted much attention in these days for high data-rate communications, since it realizes high spectrum efficiency and robustness for peformance degradation due to multipath effects.

The design and optimization of both transmission schemes essentially require information on propagation channels [13]. In the impulse based data transmission, Rake reception is implemented to improve receiving signal-to-noise ratio. The Rake reception collects power distributed over distinct echoes of transmitted signal using a Rake finger. The duration of the impulse in the time domain, or equivalently the bandwidth of the transmitted signal determines how many distinct paths are expected, thus the relationship between multipath structure and system bandwidth is essentially important to design the number of Rake fingers. The MB-OFDM system inserts guard intervals after the data stream to prevent the receiver from interruption by multipath echoes. The design of length of the guard interval is essentially dependent on the delay property of propagation channels. In this way, propagation study is mutually inter-related with transmission schemes. Our UWB channel measurement, characterization and models shall be dedicated to the link-level design and evaluation of UWB communications and equipment.

1.3 Overview of Channel Sounding and Modeling

In this section, the basis for discussing channel sounding and modeling is presented. First mathematical expressions of radio channels are given, and then channel sounding techniques and modeling campagins are summarized by referring to previous studies. Finally, existing channel models are overviewed with the empahsis on purpose and advantages of each model.

1.3.1 Mathematical Characterization of Radio Channels

The multipath propagation environment is mathematically expressed as a multi-dimensional impulse response, $h_{\alpha\beta}(t, \tau, \mathbf{\Omega}^{\mathrm{Tx}}, \mathbf{\Omega}^{\mathrm{Rx}})$. The impulse response shows the relationship between input and output through the convolution operation. The impulse response depends on the measurement time instant t and the propagation delay time (DT) τ. As the electromagnetic waves propagates in the spatial medium, the impulse response also includes angular information on both the Tx and Rx sides, $\mathbf{\Omega}^{\mathrm{Tx}}$ and $\mathbf{\Omega}^{\mathrm{Rx}}$, respectively. In fact, $\mathbf{\Omega}^{\mathrm{Tx}}$ and $\mathbf{\Omega}^{\mathrm{Rx}}$ are inter-exchangable with one another because of the reciprocal nature of the propagation medium. Here we call $\mathbf{\Omega}^{\mathrm{Tx}}$ and $\mathbf{\Omega}^{\mathrm{Rx}}$ as direction-of-departure (DOD) and direction-of-arrival (DOA), respectively. The multi-dimensional impulse response including both DOD and DOA is referred to as the double-directional impulse response. α and β are the transmitted and received polarization states respectively, and is either the vertical or horizontal polarization ($\alpha, \beta = V$ or H). The double-directional impulse response is a complete form including all the relevant propagation parameters. It has a relationship with the non-directional impulse response $h_{\alpha\beta}(t,\tau)$ as follows.

$$h_{\alpha\beta}(t,\tau) = \int_{\mathbf{\Omega}^{\mathrm{Tx}}} \int_{\mathbf{\Omega}^{\mathrm{Rx}}} h_{\alpha\beta}(t,\tau,\mathbf{\Omega}^{\mathrm{Tx}},\mathbf{\Omega}^{\mathrm{Rx}}) * D_{\beta}^{\mathrm{Rx}}(\tau,\mathbf{\Omega}^{\mathrm{Rx}}) * D_{\alpha}^{\mathrm{Tx}}(\tau,\mathbf{\Omega}^{\mathrm{Tx}}) \mathrm{d}\mathbf{\Omega}^{\mathrm{Rx}} \mathrm{d}\mathbf{\Omega}^{\mathrm{Tx}}. \tag{1.3}$$

The operation denoted by $*$ corresponds to the convolution. $D_{\alpha}^{\mathrm{Tx\ or\ Rx}}$ is a complex directivity pattern for Tx or Rx antennas dependent on the polarization state. It is also a function of the DT due to antenna group delay characteristics, but the effect is negligible in narrowband and wideband systems. The response of the double-directional impulse response is summed up with the complex directivities of the Tx and Rx antennas, and then the non-directional impulse response is derived. Single directional impulse response is obtained by performing the marginal integration at either side of the link. Actual data measured from channel sounding campaign are expressed as a coherent summation of individual impulse responses with different combinations of transmitting and receiving polarization states,

$$h = h_{VV} + h_{HH} + h_{VH} + h_{HV}. \tag{1.4}$$

The formulation is defined in the delay domain, but is easily converted into the frequency domain expression using the Fourier Transform,

$$H_{\alpha\beta}(\nu,f) = \int_{\mathbf{\Omega}^{\mathrm{Tx}}} \int_{\mathbf{\Omega}^{\mathrm{Rx}}} H_{\alpha\beta}(\nu,f,\mathbf{\Omega}^{\mathrm{Tx}},\mathbf{\Omega}^{\mathrm{Rx}}) D_{\beta}^{\mathrm{Rx}}(f,\mathbf{\Omega}^{\mathrm{Rx}}) D_{\alpha}^{\mathrm{Tx}}(f,\mathbf{\Omega}^{\mathrm{Tx}}) \mathrm{d}\mathbf{\Omega}^{\mathrm{Rx}} \mathrm{d}\mathbf{\Omega}^{\mathrm{Tx}}, \tag{1.5}$$

and

$$H = H_{VV} + H_{HH} + H_{VH} + H_{HV}. \tag{1.6}$$

H is the transfer function, and is influenced by the doppler frequency ν. The doppler frequency constitutes a Fourier pair with the time snapshot t.

It is important to note that the non-directional and single directional impulse response is composed of the propagation impulse response as well as antenna properties at both or either side of the link. Schematic view of the relationship between single and double-directional, and radio channels are shown in Fig. 1.2.

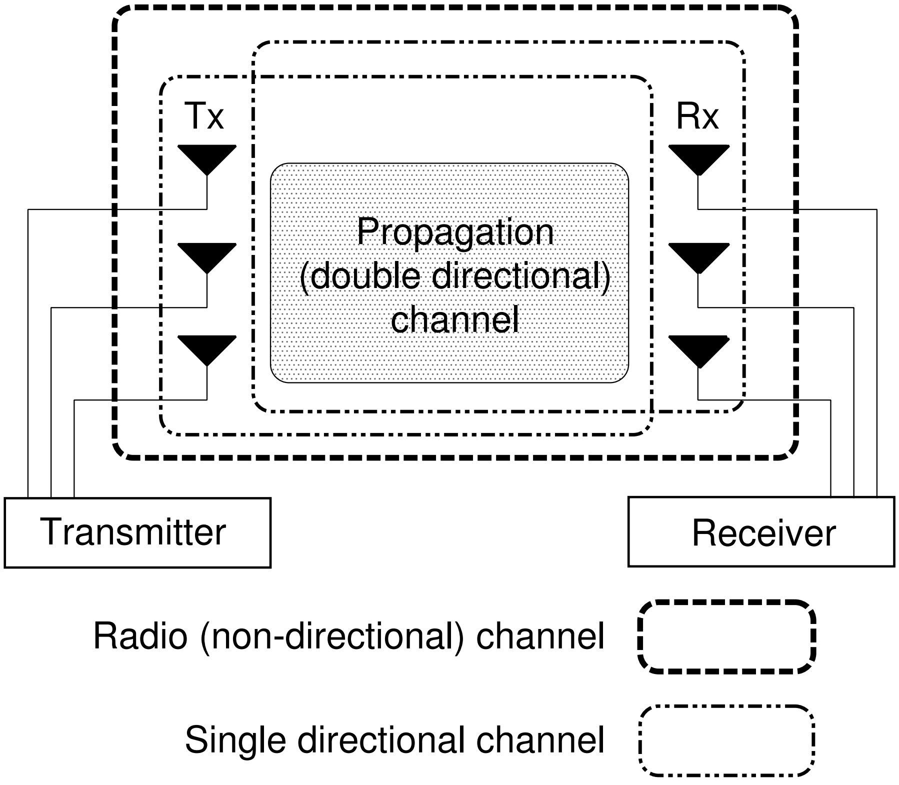

Figure 1.2 Schematic view of the relationship between double, single and non-directional channels.

1.3.2 Channel Sounding Techniques

1.3.2.1 Spatial and Temporal Channel Sounding

There have been enormous kinds of channel sounding techniques proposed and developed by many researchers to measure the impulse responses of radio channels. Furthermore, channel sounders often equip an array antenna at link ends in order to measure the angular properties of radio channels. Regardless of the investigated domains, the basic concept of the channel sounding techniques can be classified into two categories: a direct measurement and a method to utilize the Fourier pair of the domain of interests.

- Delay domain

    1. Direct measurement:

       The channel sounder transmits a certain waveform, and the receiver calculates the channel impulse response by correlating the received signal with the transmitted waveform. The transmitted waveform has to be available in the receiver in the correlation receivers. A pseudo-noise (PN) sequence or an impulse can be candidates for the transmitted signals. The delay resolution is determined by the chip rate of the PN sequences and the width of the impulse, respectively. The former method is often used in wideband channel sounding (*e.g*, [14–19]), whereas the impulse-based channel sounding is studied mostly within the context of UWB research (*e.g.,* [20–26]).

2. Using a Fourier pair:

   The channel sounding is performed using the frequency domain, and it is then converted to the delay domain by signal processing algorithms depending on the target delay resolution (see later sections for signal processing). The popular signals handled by the channel sounder is a multi-tone signal (*e.g.,* [27–35]). In this case, the power spectrum density of the transmitted signal should be as flat as possible in order to assure the dynamic range over the considered bands. Frequency-swept signal is also possible to obtain transfer function mainly by vector network analysers (*e.g.,* [36–52]). However, this method takes some time for sweeping the frequencies so that real-time measurment is prohibitive or the measurement environment should be quasi-static during the data acquisition.

In both measurement methods, syncronization between transmitter and receiver is crucial to determine the absolute delay time.

- Angular domain

  1. Direct measurement:

     Power angular profile is measured by rotating antennas which have narrower beamwidth (*e.g.,* [19,36]). The 3-dB beamwidth of the antenna determines the angular resolution. For example, parabolic antennas have a potential to realize narrow beamwidth, but sometimes the size of the antenna is so large especially when the frequency is low that it is not feasible to rotate it inside rooms.

  2. Using a Fourier pair:

     Spatial distribution of the impulse response is measured, and then it is converted into angular response using the Fourier transform or other signal processing algorithms based on the required angular resolution (see later sections for the algorithm). To measure the spatial distribution of the impulse response, there are two ways: 1) using a real array (*e.g.*, [14–18, 21, 27–30, 32, 34, 35, 38, 49, 85]), and 2) using a synthetic array (*e.g.*, [22, 37, 41, 43, 46]). Angular measurement using real array antennas sometimes require sophisticated radio frequency (RF) technologies: development of compact array antennas and array calibration techniques. As it is commonly known, the inter-element spacing of antenna array have to be less than half of the wavelength in order to avoid aliasing in the angular domain. For a carrier frequency of 5 GHz, the inter-element spacing corresponds to 30 mm, and it is clear that fabricating antenna elements as close as 30 mm is a challenging task. Still, a real antenna array for channel sounding in 4.5 and 5.3 GHz band is available [18, 35], but it simultaneously requires a antenna array calibration in order to compensate for electro-magnetic mutual coupling between antenna elements and characteristics of RF cables and switches constituting the antenna [53].

In contrast, the synthetic antenna array provides a more cost-effective method to achieve array measurement in the spatial domain. The array is realized by moving an antenna element/array over the spatial areas, and measuring the data in each spatial positions. This enables us to realize an antenna array even with a single element antenna, and complicated procedure of the antenna array calibration can be avoided. Disadvantages of the synthetic array are measurement time and accuracy of antenna alignment. In most cases, moving antennas in an accurate manner requires a certain time so that the method is not applicable for measurement involving fast doppler frequency estimation. Furthermore, a care must be taken in the accuracy of the alignment in the synthetic array, since it largely determines the angular estimation error.

In both ways of angular estimation, it is required that the propagation environment is quasi-static during the whole measurement. It is generally observed that the use of Fourier pair is more flexible in deriving angular profile than the direct measurement since various kinds of angular resolution can be achieved using different types of signal processing.

1.3.2.2 Spatio-Temporal Channel Sounding

Incorporation of more than one channel sounding domain in spatial and/or temporal domains in measurements is advantageous in realizing better path resolution. This method is called spatio-temporal channel sounding, or simply multi-dimensional channel sounding. Among many measurements taking this strategy, the value of double-directional channel sounding is becoming a popular concept [28]. The concept involves angular domain channel sounding both on Tx and Rx sides, which is advantageous in the following two sense, in addition to the improvement of path resolution: 1) since the channel sounding estimates both the DOD and DOA on Tx and Rx sides respectively, antenna gain can be separated from the path gain using the angular information. The resultant path gain expresses propagation characteristics only, so that characterization of pure propagation phenomena is possible. The propagation modeling results enables us to design and evaluate antenna systems in multipath environment [81]; and 2) identification of major scattering objects which cause reflection, diffraction, and penetration can be performed [14, 15, 32, 34, 41, 46, 49, 50, 82], helping us determine dominant propagation phenomena in that environment. It contributes mainly to the prediction of transmission performance (*e.g.*, [83]) and to the development of a site-specific propagation simulator (*e.g.,* [70]). Most of the double-directional channel sounding and propagation modeling have been done in wideband systems.

1.3.2.3 Algorithms to Convert Parameter Domains

When channel sounding measures the corresponding Fourier pair of the domain of interests, it is necessary to convert the data into the right domain using signal processing algorithms. The most primitive, but still the most reliable method is the Fourier Transform. However, as it accomplishes only limited resolution, it is often preferable to introduce algorithms that realize better resolution than the Fourier Transform. MUSIC [55] and ESPRIT [32, 56, 57] are based on the subspace-based approach, which decompose channel impulse response into discrete paths using an eigen analysis. The algorithms reveal drastic improvement of resolution with reasonable calculation load particulaly when the number of data samples are small. In contrast, a drawback of the algorithms lie in the treatment of coherent multipaths. The subspace-based algorithm cannot resolve coherent multipaths, without the help of spatial smoothing preprocessing. In channel sounding, each multipath component is radiated from an identical source, thus we always have to deal with this problem. Another limitation of subspace-based algorithms is their applicability only for narrowband systems.

Another group of algorithms showing better resolution than the Fourier transform is based on the maximum-likelihood (ML) estimation. The algorithm estimates the set of discrete paths that most likely reconstructs the measured data. Theoretically the estimator provides the most reliable results, but practical implementation of the original ML estimation is prohibitive particulaly in multi-dimensional channel sounding, due to the excessive amount of calculation. To cope with this issue, expectation-maximization (EM) [58] algorithm and the Space-Alternating EM (SAGE) [59] algorithm have been developed and widely used. Unlike the subspace-based algorithms, the ML-based approach does not need a special measure even for resolving coherent multipath signals. Recently, a sophisticated ML-based algorithm has been developed [27,53], which incorporates the proper calibration of antenna arrays as well as reliable and computationally feasible peak finding method applicable for multi-dimensional channel sounding.

The ML-based parametric channel estimation methods are based on the frequency domain and narrowband/wideband data processing. In contrast, there is also a parametric channel estimation algorithm employing the time domain processing, namely the Sensor CLEAN algorithm [22,43]. The algorithm is originally used in the radio astronomical data processing, but Cramer et. al [22] introduced it to the channel sounding purposes. The algorithm is advantageous when it is used with ultra-wideband channel sounding data which shows fine temporal resolution. The ML-based algorithm and the Sensor CLEAN algorithm differs in the data processing domain, that is, in frequency or time domain, but the fundamental concept of both algorithms are essentially the same.

1.3.3 Channel Sounding Campaigns and Modeling

There have been enormous number of channel sounding campaign performed in indoor environment using the methods described in the previous section. Next, it is also necessary to process the measured data in various manners depending on channel modeling purposes. In the following, important parameters of radio channels, which are to be characterized from the measured data, are summarized. Justification to introduce the parameters are also given by describing the relevance of the parameters with transmission performance.

1. Path loss, shadowing, and small-scale fading [7, 8, 24–26, 33, 42, 44, 47, 48]

   The fundamental characteristics of the radio wave propagation is path loss. It is derived by calculating $\int |h(\tau)|^2 \mathrm{d}\tau = \int |H(f)|^2 \mathrm{d}f$. Derivation in the frequency and time domains provides the same result due to the Parseval's equation (*e.g.*, [60]). Shadowing and small-scale fading are modeled separately from the path loss. Shadowing refers to the fluctuation of received power around the path loss, observed across several tens of wavelengths. The main reason for shadowing is the obstruction of the Fresnel zones in propagation paths due to surrounding objects. Especially obstruction of line-of-sight (LOS) path causes large shadowing. The small-scale fading looks further detailed fluctuation of the received power around the realization of shadowing. It occurs within the scale of a wavelength, and even shows much wider dynamic range of fluctuation compared to the shadowing. Modeling these characteristics are obviously important in designing link budget and receiver sensitivity of wireless systems.

2. Delay properties [7, 8, 15, 17, 20, 22, 23, 25, 30, 33, 35, 36, 42–45, 47, 48, 51, 52]

   Characterization of multipath channels in the delay domain is important in wideband systems. The time-dispersiveness causes the waveform distortion and intersymbol interference on the receiving side, ending up with the degradation of transmission performance. Generally the larger the delay spread, the more severe the transmission performance suffered from the interference. The most popular condensed parameter for the delay dispersion properties of radio channels is the delay spread. It is the second-order moment of the power delay profile. Furthermore, it was found through many measurements that modeling of the power delay profile can be performed using a superposition of clusters having an exponentially decaying shape. Here clusters are defined as the group of paths having almost the same delay time. The necessary information to specify the power delay profile is a model-parameter of clusters, such as decay constant of exponents, and the base delay time where clusters appear. Statistical analyses to derive these model-parameters have been performed by many researchers through extensive channel sounding campagigns.

3. Angular properties [17,19,22,30,34–36,41,43,46,49,52]

   Angular information has recently been actively used in wireless communications targeting for efficient use of radio spectrum and for interference cancellation, such as by smart antennas and by multiple-input multiple-output (MIMO) systems. Different from the delay domain, angular spread, showing the second order moment of the power angular profile, is not a popular measure for characterizing angular properties. Here it is also convenient to introduce clusters. In the angular domain, cluster is also defined by the group of paths coming from almost the same angles, and angular spread is derived within clusters called cluster angular spread. The larger the angular spread, the more effectively diversity works contributing to the increase of received signal strength and spectrum efficiency. The MIMO eigenmode transmission is one of the multimode transmission in the spatial domain [61].

1.3.4 Channel Models

Based on the channel sounding campaigns mentioned above, several channel models have been developed. These models differ in its purpose, thus the application and usage is also different. In this subsection, several recently developed channel models are reviewed, and their purpose and usage are summarized.

1.3.4.1 Stochastic Channel Models

Stochastic channel models are used to compare performances of transmission schemes, such as modulation and coding. The model is advantageous in its simple descriptions, but in downside, it is not applicable for simulating specific propagation environment, so often it is called site-general models. The model consists of model structure to express radio channels together with parameters that constitutes the model structure. Different propagation scenarios can be realized by adjusting the propagation parameters. The propagation parameters were developed by aggregating them from many different measurement campaigns, and therefore, each parameter is described by a statistical distribution. For indoor use, IEEE 802.11 working group developed a spatial MIMO channel model for WLAN design [62]. The spatial channel model defined the clustered multipath structures both in angular and delay domains, and provides the parameters that determines the cluster properties. Implementation of the channel model was accomplished using the tapped delay line models. Other standard channel models for indoor environment have been elaborated by the IEEE802.15.3a/4a task groups. They individually developed different channel models targeting WPAN application, and covering UWB frequency range [63–65]. Different from the IEEE802.11n model, the IEEE802.15.3a/4a models do not include angular characteristics, since UWB system does not intend to exploit spatial information. Instead, the model provides detailed description of path loss, shadowing, small-scale fading, and cluster properties in the delay domain applicable for wide frequency range. The IEEE 802.15.3a defined only four scenarios for channel realization ranging from LOS to NLOS environment revealing a severe multipath scenario. Later, the model was refined into the 4a model by including more frequency bands and scenarios, such as industrial and farm environments. Furthermore, the IEEE802.15.4a model defined antenna terms separately from the channel model descriptions, emphasizing a philosophy that propagation channels should be modeled separately from antenna properties. The philosophy is also common in the IEEE802.11n and the COST273 channel model [66]. The COST273 model was developed within the framework of COST273 activities, which is the European Forum for cooperative scientific research [67]. The model has the following characteristics: 1) it covers all the environment of interests ranging from outdoor macro and microcells to indoor picocells with the same description [68]. Different environments can be realized just by modifying model parameters. The concept is distinct from the COST259 channel model, where generation of channel response is different for macro, micro, and picocells [69]; 2) it consists of two kinds of parameters: external and stochastic parameters. The former specifies the environmental condition, such as carrier frequency, room size, antenna height/orientation, and moving direction of terminals. Path loss model belongs to this parameter. While the latter describes shadowing properties and the spatio-temporal behavior of multipath components based on the cluster model.

In any channel model, huge number of channel sounding campaigns have been carried out to collect radio channel impulse responses. Extensive data analyses have also been performed to characterize and model the impulse response.

1.3.4.2 Site-Specific Channel Models

While most of the stochastic channel models are used for standardization activities, there is another demand in simulating propagation channels. When product vendors need to have their developed equipment tested under real scenarios where the equipment is likely to be installed, the channel model should be as realistic as possible. The stochastic channel models, which is advantageous in its small number of parameters describing channel models, are in turn not suitable for simulating specific propagation scenarios due to its limited number of model parameters (although it is still possible to do that). In contrast, a tool for site-specific propagation channel simulation is widely used for its convenience to include structures of the environment under consideration. The most popular method for site-specific propagation prediction is the ray-optical simulations *e.g.*, [70]. The method introduces approximation of electromagnetic wave propagation based on the high-frequency assumption that the radio channel can be expressed as the superposition of discrete optical rays [71]. This method drastically reduces the calculation load compared to solving the original Maxwell's equation, contributing to the efficient use of computational resources and time. However, it is often reported that the simulated results by ray-tracing methods revealed large gaps compared to the measured results. The gap stems mainly from the ray-optical approximation resulting from high-frequency assumption and insufficient description of the environment inputted to the simulation. Particularly, it is articulated that non-specular scattering caused from the surface roughness of scattering objects affected the gap, since ray-optical simulations are not capable of generating the phonemena accurately in most cases [72, 73]. To include the non-specular scattering into ray-optical simulations, a hybrid method incooperating with stochastic treatment of microscopic scattering phenoemena is possible [74]. Numerical approach to simulate radio propagation using the finite difference time domain method is also used, but is still prohibitive for large scale simulations.

1.3.4.3 Stored Channel Models

Stochastic channel models provide a model description and parameters that constitute the model, and site-specific channel models are capable of generating radio channel impulse response based on the physical properties of the environment. In contrast to these models, the stored channel model does not provide structure of the models and subsequent model parameters; rather, it is a database of the measured channel response. It can be seen that the stored channel models are purely the site-specific model. The database can be applicable for many kinds of use ranging from further channel modeling under the definition of a certain model structure to the evaluation of data transmission performance considering a specific system. However, the model is inflexible in terms of antennas; in contrast to the models enabling us to include antenna properties at link ends separetely of propagation channel responses, the stored channel model hardly realizes the separated treatment of antennas and propagation. Available stored channel models, such as the ones developed by University of Southern California [75], provide UWB and MIMO measurement data covering huge environmental samples, but still includes antenna effects inside.

1.4 Outline and Contributions of Thesis

Having summarized the demands and technical challenges in modeling indoor radio wave propagation, existing channel sounding technique, channel properties to be analyzed and characterized, and available channel models for indoor environment, this thesis aims at summarizing further contributions to them. The main contributions consist of the following four-fold:

1. Developing a channel sounding method realizing accurate and high angular-delay resolution particularly suitable for indoor channel modeling;

2. Modeling indoor radio channels using the developed method with the emphasis of separating propagation from antenna properties;

3. Contributing to channel model standardization activities by dedicating channel modeling results; and
4. Assessing accuracy of channel modeling results and its applicability for link-level data transmission purposes.

Specifically, this thesis is organized into the following six Chapters.

Chapter1 Introduction, this chapter, summarizes background information related to this research, simultaneously clarifying the motivation of this research.

Chapter2 UWB Double-Directional Channel Sounder presents the concept of the channel sounder followed by theoretical characterization of the channel modeling method. The design of the channel sounder introduced both the double-directional concept and UWB signal, achieving resolution of propagation paths which have not been realized in the past activities. Furthermore, an algorithm that enables us to characterize the propagation behavior as a set of discrete propagation paths were developed. The concept of the channel sounder and the path extraction algorithm had been published in

> K. Haneda, J. Takada, and T. Kobayashi, "A parametric UWB propagation channel estimation and its performance validation in an anechoic chamber," *IEEE Transactions Microwave Theory and Techniques*, vol. 54, no. 4, pp. 1802–1811, April 2006.
>
> K. Haneda and J. Takada, "An application of SAGE algorithm for UWB propagation channel estimation," in *Proceedings of the IEEE Conference on Ultra Wideband Systems and Technologies (UWBST 2003)*, pp. 483–487, Reston, VA, USA, November 2003.

Chapter3 Verification of the UWB Double-Directional Channel Sounder in an Anechoic Chamber covers the results from experiments to assess the performances of the proposed sounder. Particular focus was laid on the verification of the angular and delay resolution of propagation paths, as well as the robustness of a wavefront model. Spherical wavefront model was introduced to estimate angular information, and was proven to be more suitable for indoor channel modeling than the conventional plane wavefront model. Results from the experiment also revealed that the parameter estimates of propagation paths were accurate enough, and the path resolution capability in the angular and delay domains were as fine as the Fourier resolution. The outcomes had been published in

> K. Haneda, J. Takada, and T. Kobayashi, "A parametric UWB propagation channel estimation and its performance validation in an anechoic chamber," *IEEE*

Transactions Microwave Theory and Techniques, vol. 54, no. 4, pp. 1802–1811, April 2006.

K. Haneda, J. Takada, and T. Kobayashi, "Experimental evaluation of a SAGE algorithm for ultra wideband channel sounding in an anechoic chamber," in *Proceedings of the International Workshop on Ultra Wideband Systems Joint with the Conference on Ultra Wideband Systems and Technologies (Joint UWBST & IWUWBS 2004)*, pp. 66–70, Kyoto, Japan, May 2004.

Chapter4 Cluster-based Analysis and Modeling of UWB Double-Directional Radio Channels in Home Environments covers results from UWB double-directional channel sounding campaigns conducted in various scenarios of home environments. Throughout this Chapter, propagation mechanisms were investigated based on the cluster treatment of multipaths both in the angular and delay domains, assuring the consistency with the recent channel modeling activities. First, propagation mechanisms of the LOS environment, where Tx and Rx antennas are placed in the same room, are investigated. Identification of scattering objects as well as derivation of scattering coefficients for the identified objects were performed. Next, environmental difference of cluster parameters are analyzed. Several environmental samples, such as room-to-corridor, inter-room, inter-floor, and outdoor-to-indoor scenarios were considered. Results revealed that the number of clusters differed from 4 to 9, where the smallerst and largest number of clusters arose from indoor-to-outdoor and inter-floor scenarios, respectively. Furthermore, dynamic range of paths, stochastic modeling of path variance in the angular and delay domains were performed. The results for LOS channel characterization and the comparison of cluster properties in different scenarios had been published in the following journal papers, respectively.

K. Haneda, J. Takada, and T. Kobayashi, "Double directional ultra wideband channel characterization in a line-of-sight home environment," *IEICE Transactions on Fundamentals*, vol. EA–88, no. 9, pp. 2264–2271, September 2005.

K. Haneda, J. Takada, and T. Kobayashi, "Cluster properties investigated from a series of ultra wideband double directional propagation measurements in home environments," *IEEE Transactions on Antennas Propagation*, vol. 54, no. 12, pp. 3778–3788, December 2006.

Furthermore, the parameters for clusters derived by this measurement and analysis had been submitted to the IEEE802.15.4a channel modeling subcommittee as a contribution document, and also approved as a representative channel parameters constituting the COST273 channel models [66].

> K. Haneda, J. Takada, and T. Kobayashi, “Spatio-temporal UWB propagation channel characterization,” IEEE 802.15-04-0112-01-004a, Orlando, FL, USA, Mar. 2004.

> L. Correia (eds.), *Towards mobile broadband multimedia networks – COST 273; European co-operation in mobile radio research,* Elsevier, Oxford, UK, March 2006.

Chapter5 Verification of UWB Double-Directional Propagation Modeling for Evaluating UWB Transmission Performance investigates the effectiveness of the results from UWB double-directional channel characterization for data transmission simulations. Comparison of bit error probability (BEP) was evaluated using two kinds of channels: one was the measured data in the experiment, and the other was the synthesized data from the channel modeling results. Results from two simulations revealed that the modeling results were not always capable of simulating transmission performance accurately. This was mainly due to the limitation of the propagation modeling, resulting in the production of “residual components” that were not modeled as discrete propagation paths. However, further investigation showed that the accuracy of the BEP prediction improved by taking into account a diffuse path, which was generated by the modeled residual components. Reasons giving rise to the limitation and countermeasures to overcome the limitations will be carefully discussed. The simulation results as well as discussions described in Chapter5 will be presented at the following international conference.

> K. Haneda, J. Takada, and T. Kobayashi, “Applicability of UWB double directional propagation modeling or evaluating UWB transmission performance,” *IEEE 65th Vehicular Technology Conference (VTC 2007 Spring)*, Dublin, Ireland, April 2007.

Finally, **Chapter6 Conclusion** summarizes the conclusions obtained from these research activities and future research items pending for further investigation, improvement, and extension.

Chapter2

UWB Double-Directional Channel Sounder

Based on the summary of spatial and temporal channel sounding techniques in Chapter1, this thesis proposes to incorporate the UWB signal with the double-directional channel sounding. The expected benefit of the incorporation is: 1) it drastically improves the resolution of physical propagation paths by virtue of multi-dimensional sounding, which is especially a suitable method for indoor channel sounding given the rich multipath environment; 2) it provides the whole spatio-temporal information of radio channels, namely DOD, DOA, and DT information; 3) it enables us to de-embed antenna properties in link ends so that antenna-independent channel models can be constructed, and applied to antenna evaluation in UWB systems. The evaluation of antennas in UWB systems is essential since antennas are the source of waveform distortion [76]. Thus far, there have been very few studies conducting UWB channel sounding which incorporates with spatial domain sounding [22, 36, 43]. Consequently, UWB channel sounding techniques incorporating the double-directional concept have not yet been investigated.

This Chapter presents the composition of the proposed UWB double-directional channel sounder. Frequency domain channel sounding was employed for data acquision, since 1) the antenna deconvolution process was easier than in the time domain, and 2) off-the-shelf equipment enabling wide frequency sweeping range and easy synchronization between Tx and Rx sides were available. Next, the most primitive way of evaluating angular and delay properties applied to our measurement data, namely the spatio-temporal beamforming is described. Furthermore, an ML-based algorithm is formulated to characterize the propagation channel as a set of discrete propagation paths. The algorithm finds the parameters of discrete paths that best fit the measured data, and is so called a parametric channel estimation algorithm. Conventionally the ML-based criterion is applied for wideband channel modeling [15, 21], but it can be modified to deal with UWB signals. Our proposed UWB channel sounding and parametric channel estimation have strengths in the following aspects: 1) to investigate frequency dependent effects of magnitude and phase in propagation paths, and 2) to incorporate the robust wavefront model of incident paths into the parametric UWB channel estimation.

The frequency dependent effects of magnitude and phase in propagation paths occur due to path loss, antenna directivities, reflection, diffraction, and penetration. To evaluate these effects, Qiu et al. [77] proposed to model the complex amplitude of each propagation path using a frequency dependence factor. Theoretically, the factor takes different values depending on the interactions that the propagation path experienced. However, meaningful values of the factor was hardly obtained according to the simulation results presented in [77] because the detected propagation paths in most cases were not “a single path” due to the limited resolution of the channel sounder. Hence our channel modeling approach deals with the modeling of frequency dependent effects using a non-parametric manner; that is, we treat the whole UWB band as a concatination of several subbands, and frequency dependent magnitude and phase is derived in each subband.

As to the robust wavefront model, we will introduce the spherical wavefront [46,78]. When estimating the directional information using antenna arrays, wavefronts of incident paths have to be determined beforehand. Plane wavefront is widely used, but it assumes that the sources are infinitely away from the arrays. This model is not realistic in indoor environments where many scattering objects are placed close to the antenna arrays. On the contrary, the spherical wavefront model can characterize the sources with finite length from the array, so improvement of the model-based estimation is expected.

Here we start from the description of measurement apparatus for UWB double-directional channel sounding.

2.1 Measurement Apparatus

The UWB double-directional channel sounder consists of a data measurement system and a parametric channel estimator. In the measurement system, frequency transfer functions of interests were obtained by a vector network analyzer (VNA). To ensure sufficient signal-to-noise ratio on the receiving side, a low-noise amplifier (LNA) with 30 dB gain was installed. The operational bandwidth of the amplifier must cover the bandwidth of interests. Only a single element antenna was installed at each link end, but a synthetic aperture was realized by moving the antenna with a spatial scanner. The synthetic aperture provides a simple and cost-effective method for DOD and DOA estimation. The basic structure of the measurement system is depicted in Fig. 2.1. This architecture has also been exploited by many researchers (*e.g.*, [37,38]).

In any measurements, it is necessary to conduct calibration before starting measurements. The calibration was normally performed using a function of VNA and back-to-back method. The calibration function of VNA compensates the transfer function of RF cables and LNA,

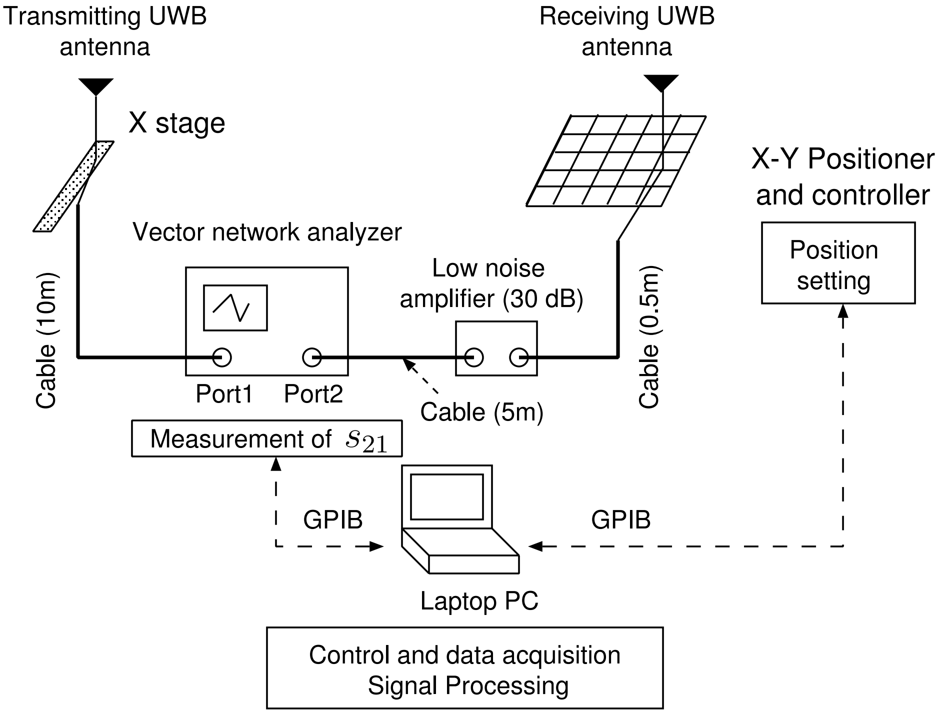

Figure 2.1 Basic structure of UWB spatio-temporal channel measurement system.

while the back-to-back calibration removes impedance mismatch between cables and antennas. The back-to-back calibration was done on-site with the antenna separation of 1 m, and electromagnetic absorbers were used to isolate the Tx and Rx antennas from surrounding objects, so that only the direct path existed. The antennas used in the link ends were UWB monopole antennas. Directivities and group delay characteristics of the antenna were measured prior to the experiment. Fluctuation of the group delay for broadside direction is small enough, less than 0.1 ns, within the considered bandwidth [79]. The antennas reveal omni-directional radiation patterns in the azimuthal plane, so that wider spatial areas can be illuminated.

2.2 Mathematical Formulation of Spatio-Temporal UWB Propagation Paths

This section first describes the underlying models to characterize the spatio-temporal radio channels together with model parameters, such as angular, delay, and polarization parameters. After the underlying models are described, general formulation of the channel transfer function is given using the defined model and model parameters. The general form is then written down to consider a specific physical arrangement of antenna arrays to be applicable for the measurement data from our channel sounding.

2.2.1 UWB Path Model

Under an assumption that electromagnetic propagation behaviors in UWB bands can be characterized by ray-path models according to the Fermat's Principle (*e.g.*, [71]). We can then define that one propagation path has direction-of-departure (DOD), $\mathbf{\Omega}^{\mathrm{Tx}}$, direction-of-arrival (DOA), $\mathbf{\Omega}^{\mathrm{Rx}}$, and delay time (DT), τ, which do not depend on frequency and polarization, and has a frequency dependent polarimetric gain. Assuming that only a single Tx antenna element is excited, we can define $D_V^{\mathrm{Tx}}(f, \mathbf{\Omega}^{\mathrm{Tx}})$ and $D_H^{\mathrm{Tx}}(f, \mathbf{\Omega}^{\mathrm{Tx}})$ as radiation patterns defined by complex amplitude for vertical and horizontal polarizations, respectively. On the receiving antenna side, $D_V^{\mathrm{Rx}}(f, \mathbf{\Omega}^{\mathrm{Rx}})$ and $D_H^{\mathrm{Rx}}(f, \mathbf{\Omega}^{\mathrm{Rx}})$ are defined as radiation patterns for a single antenna element for each polarization. The radio channel consists of antennas at link ends and propagation, and its transfer function is a multiplication of transfer functions from all of them. Using the notations defined above, the transfer function $s(f)$ of the radio channel is expressed as Eq. (2.1) in the equivalent baseband form,

$$s(f) = \alpha(f, \tau) \begin{bmatrix} D_V^{\mathrm{Rx}}(f, \mathbf{\Omega}^{\mathrm{Rx}}) \\ D_H^{\mathrm{Rx}}(f, \mathbf{\Omega}^{\mathrm{Rx}}) \end{bmatrix}^H \begin{bmatrix} r_{VV}(f) & r_{VH}(f) \\ r_{HV}(f) & r_{HH}(f) \end{bmatrix} \begin{bmatrix} D_V^{\mathrm{Tx}}(f, \mathbf{\Omega}^{\mathrm{Tx}}) \\ D_H^{\mathrm{Tx}}(f, \mathbf{\Omega}^{\mathrm{Tx}}) \end{bmatrix}, \tag{2.1}$$

where $\cdot^H$ denotes an Hermitian transpose. The terms $\alpha(f, \tau)$ and $r(f)$ represent the transfer function during propagation, and $\alpha(f, \tau)$ is a complex gain in free space denoted by

$$\alpha(f, \tau) = \frac{1}{4\pi f \tau} \exp\left(-\mathrm{j}2\pi f \tau\right). \tag{2.2}$$

Equation (2.2) is the Friis' transmission formula [80] for complex amplitude assuming a constant aperture size of the receiving antennas. The matrix with elements $r(f)$ expresses scattering loss from reflection, diffraction, and penetration in complex amplitude. The diagonal elements denote scattering coefficients for co-polarization, while the non-diagonals represent a polarization rotation effect.

2.2.2 Subband Model

As the antenna directivity and propagation loss including scattering loss and free space path loss does not drastically change within a limited bandwidth, we can divide the whole band into equally spaced I subbands, and $s(f)$ within the band can be modeled as constant. The i-th subband have center frequency f_{ci}, bandwidth of B, and constant transfer function s_i.

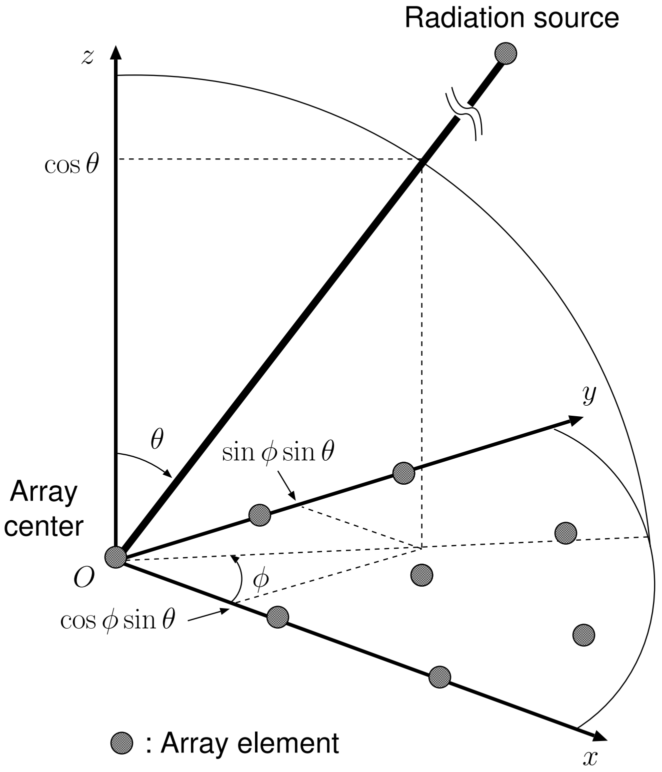

Figure 2.2 Definition of coordinate system in considered model.

2.2.3 Wavefront Models

Wavefront is an aperture consisting of a constant phase in wave propagation. It is necessary to introduce a wavefront model of incident paths to estimate its directional information using array antennas. The wavefront model determines the phase differences between antenna elements of the array. As the phase difference contains directional information, we can extract directional information by measuring the phase differences. Here, we will introduce two wavefront models, *i.e.,* spherical and plane wave models.

The spherical wave model [78] can be expressed mathematically by using azimuthal and polar angles ϕ and θ, and the curvature radius from a point source to the array center, R. The coordinate system is defined in Fig. 2.2. A position vector from the array center to the source point, $\mathbf{r}_{\text{source}}(\mathbf{\Omega}_{\text{sp}})$, is expressed as

$$\mathbf{r}_{\text{source}}(\mathbf{\Omega}) = \left[R\cos\phi\sin\theta \;\; R\sin\phi\sin\theta \;\; R\cos\theta\right]^T,$$

where $\mathbf{\Omega}_{\text{sp}} = [\phi, \theta, R]$, and $\cdot^T$ denote a transpose operation. A position vector of each antenna element, $\mathbf{r}_{\text{array}}$, is expressed as

$$\mathbf{r}_{\text{array}} = \left[d_x \;\; d_y \;\; d_z\right]^T,$$

where d_x, d_y, and d_z denote the distance from the array center to the antenna elements on x, y, and z coordinates, respectively. The phase difference between the array center and k-th antenna element, ψ_k, can be derived by the difference of distances between source to array center and source to k-th antenna element. As the distance from source to array center is R, and that from source to k-th antenna element is $||\mathbf{r}_{\text{source}} - \mathbf{r}_{\text{array},k}||$, the resulting phase difference yields

$$\psi_k(f, \boldsymbol{\Omega}) = \frac{2\pi f}{c} \left(||\mathbf{r}_{\text{source}} - \mathbf{r}_{\text{array},k}|| - R \right). \tag{2.3}$$

In case of the plane wavefront model, the dimension of $\boldsymbol{\Omega}$ is reduced to two, namely $\boldsymbol{\Omega}_{\text{pl}} = [\phi, \theta]$. The phase difference can be obtained for the plane wavefront model as in Eq. (2.4),

$$\psi_k(f, \boldsymbol{\Omega}) = \frac{2\pi f}{c} \langle \mathbf{r}_{\text{plane}},\ \mathbf{r}_{\text{array},k} \rangle, \tag{2.4}$$

where $\langle\ \cdot\ \rangle$ denotes an inner product and $\mathbf{r}_{\text{plane}}$ corresponds to the directional cosines of a unit vector,

$$\mathbf{r}_{\text{plane}}(\boldsymbol{\Omega}_{\text{pl}}) = [\cos\phi \sin\theta \quad \sin\phi \sin\theta \quad \cos\theta]^T. \tag{2.5}$$

It should be noted that the plane wavefront is equivalent to the spherical wavefront with infinite curvature radii. As the model order of the spherical wavefront model is one-dimension larger than that of plane wavefront model due to the curvature radii, the spherical wavefront model has the potential to characterize physical phenomena more precisely than the plane wavefront model.

In contrast, it must be noted as a downside of the spherical wavefront that it cannot be applicable for simultaneous DOD and DOA estimation. This is because the spherical wavefront model assumes radiation from point sources, which contradicts the use of an array on both sides of the link as depicted in Fig. 2.3.

2.2.4 Formulation of Transfer Functions Using Specific Arrays

If we assume L waves are propagating from element k_1 of the Tx array to element k_2 of the Rx array, the transfer function observed at frequency f_{k_3} within the i-th subband, $H_{k_1k_2k_3,i}$ ($1 \le k_1 \le K_1$, $1 \le k_2 \le K_2$, $1 \le k_3 \le K_3$), can be expressed as

$$\begin{aligned} H_{k_1k_2k_3,i} &= \sum_{l=1}^{L} s_{l,i} \exp\left\{-\mathrm{j}\psi^{\text{Tx}}_{k_1,l}(f_{k_3,i})\right\} \exp\left\{-\mathrm{j}\psi^{\text{Rx}}_{k_2,l}(f_{k_3,i})\right\} \exp\left(-\mathrm{j}2\pi f_{k_3,i}\tau_l\right) && (2.6) \\ &\equiv \sum_{l=1}^{L} h_{l,k_1k_2k_3,i}. && (2.7) \end{aligned}$$

In later descriptions, we call $s_{l,i}$ as the reference transfer function of the l-th wave in the i-th subband. It is called "reference" because it expresses the transfer function between the array centers of the Tx and Rx.

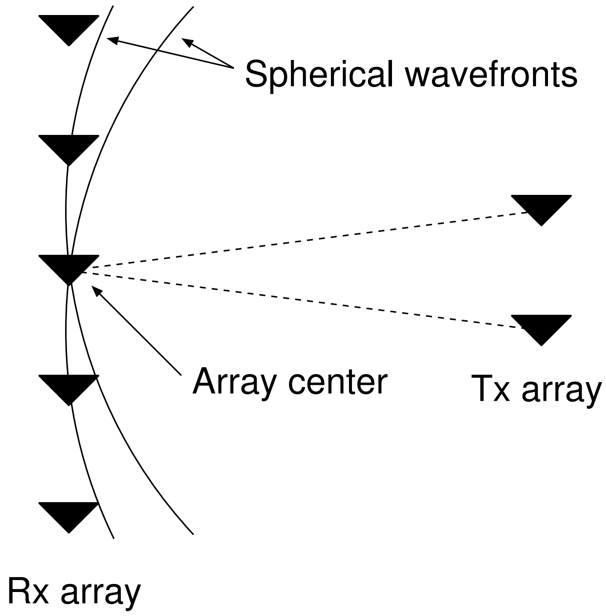

Figure 2.3 Spherical wavefront model is incompatible with simultaneous DOD and DOA estimation: Different radiation sources in Tx array result in different shapes for spherical wavefronts in Rx array.

For convenience of the notation, we vectorize the channel transfer function in i-th subband as

$$\mathbf{H}_i = \sum_{l=1}^{L} \mathbf{h}_{l,i} = \mathbf{A}_i \mathbf{s}_i \in C^{K\times 1} \tag{2.8}$$

where $K = K_1 K_2 K_3$ and

$$\begin{aligned}
\mathbf{s}_i &= [s_{1,i} \cdots s_{l,i} \cdots s_{L,i}], \in C^{L\times 1}, && (2.9)\\
\mathbf{A}_i &= [\mathbf{a}_{1,i} \cdots \mathbf{a}_{l,i} \cdots \mathbf{a}_{L,i}] \in C^{K\times L}, && (2.10)\\
\mathbf{a}_{l,i} &= \mathbf{a}_{l,i}^{\mathrm{Tx}} \otimes \mathbf{a}_{l,i}^{\mathrm{Rx}} \otimes \mathbf{a}_{l,i}^{\mathrm{Fr}} \in C^{K\times 1}, && (2.11)\\
\mathbf{a}_{l,i}^{\mathrm{Tx}} &= \left[\exp\left\{-\mathrm{j}\psi_{1,l}^{\mathrm{Tx}}(f_{1,i})\right\} \cdots \exp\left\{-\mathrm{j}\psi_{k_1,l}^{\mathrm{Tx}}(f_{k_1,i})\right\} \cdots \exp\left\{-\mathrm{j}\psi_{K_1,l}^{\mathrm{Tx}}(f_{K_1,i})\right\}\right], && (2.12)\\
\mathbf{a}_{l,i}^{\mathrm{Rx}} &= \left[\exp\left\{-\mathrm{j}\psi_{1,l}^{\mathrm{Rx}}(f_{1,i})\right\} \cdots \exp\left\{-\mathrm{j}\psi_{k_2,l}^{\mathrm{Rx}}(f_{k_2,i})\right\} \cdots \exp\left\{-\mathrm{j}\psi_{K_2,l}^{\mathrm{Rx}}(f_{K_2,i})\right\}\right], && (2.13)\\
\mathbf{a}_{l,i}^{\mathrm{Fr}} &= [\exp(-\mathrm{j}2\pi f_{1,i}\tau_l) \cdots \exp(-\mathrm{j}2\pi f_{k_3,i}\tau_l) \cdots \exp(-\mathrm{j}2\pi f_{K_3,i}\tau_l)]. && (2.14)
\end{aligned}$$

The operation $\otimes$ denotes the Kronecker product. The vector/matrix composed of the phase difference terms are called array steering vector/matrix. Under the plane wavefront model, specific expression can be derived for the phase difference terms by considering typical antenna arrays, such as a uniform linear array (ULA) and a uniform rectangular array (URA) on the horizontal plane as follows:

$$\begin{aligned}\exp\left\{-\mathrm{j}\psi_{k_1,l}(f_{k_3,i})\right\} &= \exp\left[-\mathrm{j}\frac{2\pi f_{k_3,i}}{c}\Delta d m_1\cos\phi+\mathrm{j}\xi\right] \quad \text{(ULA)} \qquad (2.15)\\ &= \exp\left[-\mathrm{j}\frac{2\pi f_{k_3,i}}{c}\Delta d(m_1\cos\phi\sin\theta+m_2\sin\phi\sin\theta)+\mathrm{j}\xi\right]\\ &\quad \text{(URA)}. \qquad (2.16)\end{aligned}$$

m_1 and m_2 are the element indices on the x and y axes respectively ($1 \le m_1 \le M_1$, $1 \le m_2 \le M_2$). Δd denotes the inter-element spacing of the array. For the URA, we assume that Δd takes the same value for x and y axes for simplicity. Both ULA and URA are used in the measurements described in later chapters. ξ is an offset of the phase which should be taken into account when the array center is not located on the origin of the coordinates.

2.3 UWB Spatio-Temporal Beamforming

The most primitive methods to obtain angular-delay properties from the spatio-temporal measured data is the Fourier Transform. In the angular domain, it is alternatively called beamforming. Although this method is not a parametric algorithm which estimates the parameters of propagation paths, it is informative to consider this method since it provides us with the fundamental angular and delay resolution realized by antenna aperture size and signal bandwidth of the channel sounding, respectively.

As the measured data are discrete forms in the spatial-frequency domain, actual implementation of the method becomes the discrete Fourier Transform,

$$h(\mathbf{\Omega}^{\mathrm{Tx}},\mathbf{\Omega}^{\mathrm{Rx}},\tau)=\frac{1}{KI}\sum_{k_1=1}^{K_1}\sum_{k_2=1}^{K_2}\sum_{k_3=1}^{K_3 I}H_{k_1k_2k_3,i}\exp\left\{\mathrm{j}\psi^{\mathrm{Tx}}_{k_1,l}(f_{k_3,i})\right\}\exp\left\{\mathrm{j}\psi^{\mathrm{Rx}}_{k_2,l}(f_{k_3,i})\right\}\exp\left(\mathrm{j}2\pi f_{k_3,i}\tau_l\right) \qquad (2.17)$$

In the following, we investigate the beampatterns synthesized by ULA and URA. The Fourier resolution in the angular domain is determined in the analysis, which is one of the most important specification of the channel sounding.

2.3.1 Synthesized Beampattern

Array configuration is summarized in Table 2.1 together with the frequency range used for beam synthesis. For ULA, the number of antenna elements were 4, while the URA took two kinds of antenna configuration: 4 × 4 and 10 × 10. In all cases, inter-element spacings were set to 48 mm. It corresponds to 0.49λ in the lowest frequency, 3.1 GHz. Except for two arrays which are to be used in Chapter5, the array was used with full frequency band allowed for UWB systems in the microwave range, 3.1 – 10.6 GHz.

The synthesized beampatterns in the azimuthal domain using the Fourier Transform for arrays (a) to (d) are shown in Fig. 2.4. We could treat the beampattern on the Tx and Rx sides separately because they are independent of each other. An incoming plane wave was assumed from $\phi = 0$ deg and $\theta = 90$ deg. Definition of coordinates follows Fig. 2.2. In the beam synthesis, beampatterns of different frequencies are coherently summed by considering DT. The beampattern showed some sidelobes and grating lobes, but its response was at least 13 dB below the mainlobe. The 3-dB beamwidth of the mainlobe gave rise to the Fourier resolution of the array, and is summarized in Table 2.1. It was found that the larger size of the array led to narrower beamwidth, corresponding to better angular resolution. It also turned out that the beamwidth of pattern (d) was slightly wider than that of pattern (b) though the two arrays used the same aperture size. The difference stemmed from the difference of frequency range used in the beam synthesis. Generally higher frequency realizes narrower beamwidth given the constant physical size of antenna aperture, and therefore, summing beampatterns up until higher frequencies gave rise to the narrower beamwidth in pattern (b).

Both ULA and URA have uncertaintly in estimating angles, which is called "ambiguity". A horizontal URA cannot distinguish paths coming from $+z$ and $-z$ axis of the array, since the phase response of the URA between the two paths are identical. A ULA can cover angular estimation only for half the plane, thus the ambiguity of ULA is called "cone ambiguity". Assuming that a ULA is on the y-axis in the definition of coordinates depicted in Fig. 2.2, it can cover $-90 \leq \phi \leq 90$ [deg], and paths coming from $-180 \leq \phi \leq -90$ [deg] and $90 \leq \phi \leq 180$ [deg] are treated equivalently as path incidence from $-90 \leq \phi \leq 0$ [deg] and $0 \leq \phi \leq 90$ [deg], respectively. Furthermore, the ULA is not capable of resolving paths in the endfire directions, ±90 deg since the effective size of antenna aperture is the smallest in that direction. In contrast, the finest resolution is realized in the broadside (0 deg) incidence, which is shown in Table 2.1. It can be seen that the azimuthal resolution of the ULA is the same as that of URA, as far as the path incident from the broadside was concerned. To estimate angular information without ambiguities, antenna arrays having a volume of aperture is necessary, such as spherical and cube antennas.

The synthesized beampattern for polar angle is shown in Fig. 2.5. In this analysis, calculation of the angular resolution was done for the plane wave incidence from $\theta = 90$ deg, that is from the horizontal plane. Since Tx and Rx antennas were placed almost at the same height in most of our channel sounding campaigns, we expect many paths incident from this angle. However, paths coming from $\theta = 90$ deg is endfire incidence, resulting in a poor path resolution capability. When beampattern of array (b) was calculated for paths coming from 65 deg, it intersected with the beampattern from incident angles 90 deg with -3 dB of the normalized gain. Thus it can be seen that the path resolution in the polar domain was 25 deg. As similar to the resolution in the azimuthal domain, the worse polar resolution was obtained for smaller size of the antenna aperture, *i.e.,* array (b).

Table 2.1 Specifications of Array Configuration in Channel Sounding Campaigns.

	Chapter in this thesis	Types of the array	# of elements (Spacings [mm])	Frequency range [GHz]	Angular resolution [deg]	Notes
(a)	Chapter3	Horizontal rectangular	10×10 (48)	3.1 to 10.6	6 (Az) 25 (El)	
(b)	Chapter4	Horizontal rectangular	4×4 (48)	3.1 to 10.6	18 (Az) 40 (El)	Rx side
(c)	Chapter4	Horizontal linear	4 (48)	3.1 to 10.6	18 (Az)	Tx side
(d)	Chapter5	Horizontal rectangular	4×4 (48)	3.1 to 5.0	20 (Az) 40 (El)	Rx side
(e)	Chapter5	Horizontal linear	4 (48)	3.1 to 5.0	20 (Az)	Tx side

2.3.2 Delay Resolution

The delay resolution can also be determined from the spatio-temporal beamforming results in the same manner as angular resolution. It was found that the delay resolution is solely dependent on the signal bandwidths used in the channel sounding, and specifically, the inverse of the bandwidths gives the delay resolution. In arrays (a) to (c), the delay resolution was 0.13 ns corresponding to 40 mm resolution of path length. In arrays (d) and (e), 0.5 ns delay resolution was accomplished, equivalent to 150 mm resolution in distance.

2.4 ML-based Estimator for UWB signals

Next, a maximum-likelihood (ML) based algorithm is introduced to characterize the angular-delay behavior of propagation channels. Different from the spectrum-based characterization of propagation channels, the ML-based approach enables us to characterize propagation behavior as a set of discrete propagation paths. The ML estimation finds parameters of propagation paths that maximize the likelihood function by considering a certain signal model, and therefore, this method is called parametric channel estimation. The signal model and its parameters are defined in Chap. 2.2. The likelihood function in our case is the conditional probability of measured data, given a model of signal components, its model parameters, and the probability density function of the noise. The noise components are assumed to follow identically and independently distributed complex gaussian distribution where its mean and power equal to 0 and σ^2.

In the vectorized notation, the measured data in experiments are composed of the transfer functions perturbed by thermal noise $\mathbf{n}_i \in C^K$,

$$\mathbf{y}_i = \mathbf{H}_i + \mathbf{n}_i = \sum_{l=1}^{L} \mathbf{h}_{l,i} + \mathbf{n}_i, \tag{2.18}$$

and then the data vector composed of the whole measured data and the tranfer function vector yields

$$\begin{aligned} \mathbf{y} &= \left[\mathbf{y}_1^T \ \mathbf{y}_2^T \cdots \mathbf{y}_I^T\right]^T \in C^{KI\times 1}, && (2.19)\\ \mathbf{H} &= \left[\mathbf{H}_1^T \ \mathbf{H}_2^T \cdots \mathbf{H}_I^T\right]^T, && (2.20)\\ \mathbf{h}_l &= \left[\mathbf{h}_{l,1}^T \ \mathbf{h}_{l,2}^T \cdots \mathbf{h}_{l,I}^T\right]^T. && (2.21) \end{aligned}$$

Furthermore, we define a model parameter set $\boldsymbol{\mu}$ as Eq. (2.22).

$$\boldsymbol{\mu} = \left[\left\{s_{l,i}\right\}_i, \boldsymbol{\Omega}_l^{\mathrm{Tx}}, \boldsymbol{\Omega}_l^{\mathrm{Rx}}, \tau_l\right]_{l=1}^{L}. \tag{2.22}$$

Using the notations defined above, the likelihood function is expressed as Eq. (2.23),

$$p(\mathbf{y}|\boldsymbol{\mu}) = \prod_{k_1=1}^{K_1} \prod_{k_2=1}^{K_2} \prod_{k_3=1}^{K_3} \prod_{i=1}^{I} \left[\frac{1}{\pi\sigma} \exp\left(-\frac{|y_{k_1k_2k_3,i} - H_{k_1k_2k_3,i}|^2}{\sigma^2}\right)\right]. \tag{2.23}$$

By taking the logarithm of Eq. (2.23), the log-likelihood function is simplified as follows.

$$\log\left[p(\mathbf{y}|\boldsymbol{\mu})\right] = -KI \log \pi\sigma - \frac{||\mathbf{y} - \mathbf{H}(\boldsymbol{\mu})||^2}{\sigma^2} \tag{2.24}$$

Thus the ML estimation of parameters which maximize the likelihood function in Eq. (2.23) is

$$\hat{\boldsymbol{\mu}} = \arg\max_{\boldsymbol{\mu}} p(\mathbf{y}|\boldsymbol{\mu}) = \arg\min_{\boldsymbol{\mu}} ||\mathbf{y} - \mathbf{H}(\boldsymbol{\mu})||^2, \tag{2.25}$$

where $\hat{\cdot}$ means that the parameter is estimated. Finding $\boldsymbol{\mu}$ in Eq. (2.25) is computationally prohibitive due to the large simultaneous search dimensions. Here we introduce the expectation and maximization (EM) algorithm [58] to mitigate the computational load by reducing the simultaneous search dimension. The EM algorithm first estimates the transfer function of each path perturbed by noise, $\mathbf{x}_l$, from the measured data, $\mathbf{y}$ as Eq. (2.26),

$$\mathbf{x}_l = \mathbf{h}_l + \beta_l\left(\mathbf{y} - \mathbf{H}\right), \tag{2.26}$$

where β_l has a constraint

$$\sum_{l=1}^{L} \beta_l = 1, \quad \beta_l > 0 \ \text{ for all } l. \tag{2.27}$$

Equation (2.26) means that the expectation of the noise for each path is expressed as a part of the measured noise component. Practically $\beta = 1/L$ for all l which maximizes the conditional fisher information of the estimated $\mathbf{x}_l$ [15]. The log-likelihood function for $\mathbf{x}_l$ is analogous to Eq. (2.25),

$$\hat{\boldsymbol{\mu}}_l = \arg\min_{\boldsymbol{\mu}_l} ||\mathbf{x}_l - \mathbf{h}(\boldsymbol{\mu}_l)||^2, \tag{2.28}$$

where $\boldsymbol{\mu}_l$ is a set of model parameters for the l-th wave,

$$\boldsymbol{\mu}_l = \left[\{s_{l,i}\}_i, \boldsymbol{\Omega}_l^{\mathrm{Tx}}, \boldsymbol{\Omega}_l^{\mathrm{Rx}}, \tau_l\right]. \tag{2.29}$$

Equation (2.28) corresponds to the maximization step of the EM algorithm. The simultaneous search dimension is reduced to the set of single waves. Using the array steering vector defined in the previous section, Eq. (2.28) can be rewritten as

$$\hat{\boldsymbol{\mu}}_l = \arg\min_{\boldsymbol{\mu}_l} \sum_{i=1}^{I} ||\mathbf{x}_{l,i} - s_{l,i}\mathbf{a}_{l,i}(\boldsymbol{\mu}_l')||^2, \tag{2.30}$$

where $\mathbf{x}_{l,i}$ is the estimated data of the l-th path in the i-th subband, and

$$\boldsymbol{\mu}_l' = \left[\boldsymbol{\Omega}_l^{\mathrm{Tx}}, \boldsymbol{\Omega}_l^{\mathrm{Rx}}, \tau_l\right]. \tag{2.31}$$

Equation (2.30) is a procedure that finds the model parameters $\boldsymbol{\mu}_l'$ which extract the largest power from $\mathbf{x}_l$. Thus we can reorganize the procedure by a matched filter approximation,

$$\hat{\boldsymbol{\mu}}_l' = \arg\max_{\boldsymbol{\mu}_l'} \sum_{i=1}^{I} ||\mathbf{a}_{l,i}^H(\boldsymbol{\mu}_l')\mathbf{x}_{l,i}||^2. \tag{2.32}$$

The maximization procedure can be further reduced to one-dimensional sequential search using the space alternating generalized EM (SAGE) algorithm [59]. The search is conducted parameter by parameter, and iteratively updating the parameters. During a search of one parameter, other parameters are kept fixed. As it is verified that the log-likelihood function is monotonically increasing in the sequential search, an iteration of the set of sequential search can reach a certain maximum value of the log-likelihood function.

After $\boldsymbol{\mu}_l$ is estimated, the reference transfer functions, $s_{l,i}$, can then be obtained by utilizing a part of the likelihood function within the i-th subband. It is derived as a maximum value of the matched filter output,

$$\hat{s}_{l,i} = \frac{\mathbf{a}_{l,i}^H(\hat{\boldsymbol{\mu}}_l')\mathbf{x}_{l,i}}{\mathbf{a}_{l,i}^H(\hat{\boldsymbol{\mu}}_l')\mathbf{a}_{l,i}(\hat{\boldsymbol{\mu}}_l')}, \tag{2.33}$$

where the i-th subband spans the frequency band between $(f_{ci} - \frac{B}{2})$ and $(f_{ci} + \frac{B}{2})$, and f_{ci} denotes the center frequency of the i-th subband. $\hat{\boldsymbol{\mu}}_l'$ denotes an estimated result of model parameters which is common over the whole frequency band. Here, if we assume that the reference transfer function of each subband is represented by that at the center frequency of the subband, we can derive the reference transfer function at any frequency using Eq. (2.33) by shifting the subband, namely shifting the center frequency, with a constant B.

2.4.1 Consideration on Subbands

The bandwidth for subband B can be optimized in the implementation of the ML-based estimator. Let us assume two paths are $\Delta\phi$ and $\Delta\tau$ apart in the azimuthal and delay domains, respectively. Furthemore, we define Ξ_ϕ and Ξ_τ as a Fourier resolution of the estimator in the azimuthal and delay domains, which were determined in Chap. 2.3. In fact, the selection of the width of the subband indicates a tradeoff between accurate estimation of the reference transfer functions and achievable time resolution. The larger the bandwidth that is dedicated to achieve greater time resolution, the larger the error in the results of the estimated reference transfer functions. Therefore, the following criteria are recommended in selecting the optimum width of the subbands.

1. When $\Delta\phi > \Xi_\phi$:
   As the path is already resolved in the angular domain, the use of a narrower bandwidth is recommended where variations in antennas and propagation characteristics are reasonably small, in order to probe frequency dependent magnitude and phase accurately.

2. When $\Delta\phi < \Xi_\phi$:
   The value of B should be more than a fraction of the value $\Delta\tau$ in order to resolve two paths in the delay domain.

The criteria are summarized in Fig. 2.6.

2.4.2 Implementation of the ML-based Estimator

We implemented the ML-based estimator in a succesive interference cancellation (SIC) manner [21]. Although the main drawback of the SIC type path detection is error propagation, the fine time resolution offered by UWB signals can mitigate it, since the detection and removal of the paths are conducted in an accurate manner. The SIC type procedure is equivalent to the EM algorithm with the number of paths equals to one, and consists of the following steps:

1. Find value of model parameters of the strongest path, given the measured data $\mathbf{y}$ is substituted into Eq. (2.32);

2. Find the reference transfer function, $\{\hat{s}_i\}_{i=1}^{I}$, using the estimated model parameters and Eq. (2.33);

3. Reconstruct data of the strongest path, $\mathbf{h}_l$, using Eq. (2.6), and remove it from the original data $\mathbf{y}$;

4. Substitute the resultant data $(\mathbf{y} - \mathbf{h}_l)$ into $\mathbf{y}$, and return to step 1);

5. Continue the set of steps mentioned above until the number of paths reaches a predefined number, or power of detected path is below a certain threshould level, *e.g.*, the noise level.

In finding the value of model parameters in step 1), a combination of a coarse global mesh search based on the EM algorithm and a fine local search based on the SAGE algorithm was employed. In the coarse global mesh search, we identified the region which might include the values of parameters that gave the maximum value of the log-likelihood function. After the region was specified, fine local search was conducted inside the region to find the value of parameters accurately. The flow of the implemented ML-based algorithms are shown in Fig. 2.7. The path detection took different procedure for processing the full-band ($3.1-10.6$ GHz) and low-band ($3.1-5.0$ GHz) data. In the full-band implementation, path detection was done in the angular-delay domain, whereas angular domain was not incoporated in the low-band implementation. This difference is attributed to a relationship between delay resolution of the system and inter-element spacings. The full-band measurement had distance resolution of 40 mm, but this was even capable of resolving each element of antenna arrays on Tx and Rx sides, as we set the inter-element spacings to 48 mm. This prevented us from implementing the path detection using the simple power delay profile (PDP), because a single path might be detected several times due to the fine resolution. Angular estimation can compensate for this issue, since it utilizes the difference of the DT within antenna arrays to estimate angles. Hence this was incorporated with the DT estimation for the full-band data processing, necessitating the derivation of two-dimensional power angular-delay profile (PADP) for path detection. In contrast, the restriction for the relationship between delay resolution and inter-element spacings in the low-band measurement was relieved: the resolution in distance and the maximum size of the antenna aperture were about 160 mm and 200 mm, respectively. Thus the path detection was done simply in the delay domain, enabling us to reduce the computational time drastically without lossing the accuracy of the parameter estimates.

2.5 The Cramér-Rao Lower Bound (CRLB)

The CRLB, as the name suggests, provides the lower bound of variance in any biased and unbiased parameter estimates. Particularly, as the root of the CRLB, $\sqrt{\text{CRLB}}$ corresponds to the lower bound of the root mean square error (RMSE) of parameter estimates, it can be used as a criterion to evaluate the reliability of parameter estimates. We provide the derivation of CRLB for our channel modeling purposes. Specifically, the CRLB of parameter estimates from 1) double-directional channel modeling using the plane wavefront, and 2) single directional channel modeling using the spherical wavefront are presented. The CRLB is determined by the structure of available data samples, *i.e.,* the measured data.

2.5.1 CRLB of Parameter Estimates in the UWB Double-Directional Channel Sounding

In our UWB double-directional channel modeling described in later Chapters, the parameter estimation was 4-dimensional: simultaneous estimation of DOD azimuth ϕ^{Tx}, DOA azimuth ϕ^{Rx}, DOA polar θ, and DT τ. The CRLB is given by the inverse of the Fisher Information Matrix (FIM) which is Hermitian, positive definite, and has the dimension of $4L \times 4L$ where L denotes the number of waves,

$$\mathbf{F}_{\mathrm{dd}} = \begin{pmatrix} \mathbf{F}_{\phi^{\mathrm{Rx}}\phi^{\mathrm{Rx}}} & \mathbf{F}_{\phi^{\mathrm{Rx}}\theta} & \mathbf{F}_{\phi^{\mathrm{Rx}}\phi^{\mathrm{Tx}}} & \mathbf{F}_{\phi^{\mathrm{Rx}}\tau} \\ \mathbf{F}_{\theta\phi^{\mathrm{Rx}}} & \mathbf{F}_{\theta\theta} & \mathbf{F}_{\theta\phi^{\mathrm{Tx}}} & \mathbf{F}_{\theta\tau} \\ \mathbf{F}_{\phi^{\mathrm{Tx}}\phi^{\mathrm{Rx}}} & \mathbf{F}_{\phi^{\mathrm{Tx}}\theta} & \mathbf{F}_{\phi^{\mathrm{Tx}}\phi^{\mathrm{Tx}}} & \mathbf{F}_{\phi^{\mathrm{Tx}}\tau} \\ \mathbf{F}_{\tau\phi^{\mathrm{Rx}}} & \mathbf{F}_{\tau\theta} & \mathbf{F}_{\tau\phi^{\mathrm{Tx}}} & \mathbf{F}_{\tau\tau} \end{pmatrix}. \tag{2.34}$$

Each component of the submatrices in FIM is derived as

$$F_{\zeta,\xi\ (l,l')} = \sqrt{\gamma_l}\sqrt{\gamma_{l'}}\mathrm{Re}\left\{ \left(\left.\frac{\partial \mathbf{a}(\zeta)}{\partial \zeta}\right|_{\zeta=\zeta_l} \right)^H \left(\left.\frac{\partial \mathbf{a}(\xi)}{\partial \xi}\right|_{\xi=\xi'_l} \right) \right\} \tag{2.35}$$

where $\mathbf{a}$ is the array steering vector composed of all the array steering vectors in each subband $\mathbf{a}_i = \mathbf{a}_i^{\mathrm{Tx}} \otimes \mathbf{a}_i^{\mathrm{Rx}} \otimes \mathbf{a}_i^{\mathrm{Fr}}$,

$$\mathbf{a} = \left[\mathbf{a}_1^T \cdots \mathbf{a}_i^T \cdots \mathbf{a}_I^T\right]^T. \tag{2.36}$$

ζ and ξ can be either ϕ^{Tx}, ϕ^{Rx}, θ, or τ. Equation (2.35) is applied to the (l, l')-th component of the FIM submatrices. γ_l is the signal-to-noise ratio of the l-th path which has a relationship between the reference transfer function as

$$\gamma_l = \frac{1}{P_n}\sum_{i=1}^{I} |s_{l,i}|^2 \tag{2.37}$$

where P_n is the noise level relative to the transmitted power.

As we used ULA and URA for Tx and Rx arrays respectively, the partial derivative of Eq. (2.35) yields

$$\frac{\partial \mathbf{a}(\phi^{\mathrm{Rx}})}{\partial \phi^{\mathrm{Rx}}} = \left(\mathbf{B}^{\mathrm{Rx}}\mathbf{a}^{\mathrm{Rx}}\right) \otimes \mathbf{a}^{\mathrm{Tx}} \otimes \mathbf{a}^{\mathrm{Fr}}, \tag{2.38}$$

$$\frac{\partial \mathbf{a}(\theta)}{\partial \theta} = \left(\mathbf{B}^{\mathrm{Rx}'}\mathbf{a}^{\mathrm{Rx}}\right) \otimes \mathbf{a}^{\mathrm{Tx}} \otimes \mathbf{a}^{\mathrm{Fr}}, \tag{2.39}$$

$$\frac{\partial \mathbf{a}(\phi^{\mathrm{Tx}})}{\partial \phi^{\mathrm{Tx}}} = \mathbf{a}^{\mathrm{Rx}} \otimes \left(\mathbf{B}^{\mathrm{Tx}}\mathbf{a}^{\mathrm{Tx}}\right) \otimes \mathbf{a}^{\mathrm{Fr}}, \tag{2.40}$$

$$\frac{\partial \mathbf{a}(\tau)}{\partial \tau} = \mathbf{a}^{\mathrm{Rx}} \otimes \mathbf{a}^{\mathrm{Tx}} \otimes \left(\mathbf{B}^{\mathrm{Fr}}\mathbf{a}^{\mathrm{Fr}}\right), \tag{2.41}$$

where the diagonal matrices $\mathbf{B} \in C^{L\times L}$ are composed of the following elements:

$$\begin{aligned}
\mathbf{B}^{\mathrm{Rx}} &= \operatorname{diag}\left(-\mathrm{j}\frac{2\pi f_{k_3,i}}{c}\Delta d(-m_1 \sin\phi^{\mathrm{Rx}} \sin\theta + m_2 \cos\phi^{\mathrm{Rx}} \sin\theta)\right), && (2.42)\\
\mathbf{B}^{\mathrm{Rx}'} &= \operatorname{diag}\left(-\mathrm{j}\frac{2\pi f_{k_3,i}}{c}\Delta d(m_1 \cos\phi^{\mathrm{Rx}} \cos\theta + m_2 \sin\phi^{\mathrm{Rx}} \cos\theta)\right), && (2.43)\\
\mathbf{B}^{\mathrm{Tx}} &= \operatorname{diag}\left(-\mathrm{j}\frac{2\pi f_{k_3,i}}{c}\Delta d(-n \sin\phi^{\mathrm{Rx}})\right), && (2.44)\\
\mathbf{B}^{\mathrm{Fr}} &= \operatorname{diag}\left(-\mathrm{j}2\pi f_{k_3,i}\right). && (2.45)
\end{aligned}$$

Finally, the inverse of the FIM yields a matrix composed of CRLB,

$$\mathbf{CRLB}_{\mathrm{dd}} = \mathbf{F}_{\mathrm{dd}}^{-1}. \tag{2.46}$$

With the composition of FIM in Eq. (2.35), the CRLB for each parameter estimates is obtained in the diagonal elements of **CRLB** as follows.

$$\begin{aligned}
\mathrm{CRLB}(\phi_l^{\mathrm{Rx}}) &= \mathbf{CRLB}_{\mathrm{dd}(l,l)},\\
\mathrm{CRLB}(\theta_l) &= \mathbf{CRLB}_{\mathrm{dd}(L+l,L+l)},\\
\mathrm{CRLB}(\phi_l^{\mathrm{Tx}}) &= \mathbf{CRLB}_{\mathrm{dd}(2L+l,2L+l)},\\
\mathrm{CRLB}(\tau_l) &= \mathbf{CRLB}_{\mathrm{dd}(3L+l,3L+l)}.
\end{aligned}$$

The non-diagonal elements of **CRLB** represents the correlation of different parameter estimates. If two parameter estimates are uncorrelated, the value is 0.

2.5.2 CRLB of Parameter Estimates Using the Spherical Wavefront

As to the spherical wavefront model, we derive the CRLB for multidimensional parameter estimates composed of single directional angular information, such as azimuthal angle ϕ and polar angle θ, as well as the delay time τ and curvature radii R. The FIM is also $4L \times 4L$ dimensional in this case,

$$\mathbf{F}_{\mathrm{sp}} = \begin{pmatrix} \mathbf{F}_{\phi\phi} & \mathbf{F}_{\phi\theta} & \mathbf{F}_{\phi R} & \mathbf{F}_{\phi\tau} \\ \mathbf{F}_{\theta\phi} & \mathbf{F}_{\theta\theta} & \mathbf{F}_{\theta R} & \mathbf{F}_{\theta\tau} \\ \mathbf{F}_{R\phi} & \mathbf{F}_{R\theta} & \mathbf{F}_{RR} & \mathbf{F}_{R\tau} \\ \mathbf{F}_{\tau\phi} & \mathbf{F}_{\tau\theta} & \mathbf{F}_{\tau R} & \mathbf{F}_{\tau\tau} \end{pmatrix}. \tag{2.47}$$

Each component of the submatrices in FIM is given as Eq. (2.35). However, different from the plane wavefront model, the array steering vector $\mathbf{a} \in C^{K_1 K_3 I\times 1}$ has a more complicated form than the plane wavefront case, and cannot be expressed using the Kronecker product. When URA is considered, the element of the array steering vector yields

$$a_{k_1k_3,i} = \exp\left\{-\mathrm{j}\frac{2\pi f_{k_3,i}}{c}\left(||\mathbf{r}_{\text{source}} - \mathbf{r}_{\text{array},k_1}|| - R\right)\right\}\exp\{-\mathrm{j}2\pi f_{k_3,i}\tau\}. \tag{2.48}$$

The partial derivative of Eq. (2.48) is

$$\begin{aligned}
\frac{\partial a_{k_1k_3,i}}{\partial \phi} &= -\mathrm{j}\frac{2\pi f_{k_3,i}}{c} b^{\phi}_{k_1k_3,i}\cdot a_{k_1k_3,i}, &(2.49)\\
b^{\phi}_{k_1k_3,i} &= \frac{d_x\sin\phi(R - d_x\cos\phi\sin\theta) + d_y\cos\phi(d_y\sin\phi\sin\theta - R)}{||\mathbf{r}_{\text{source}} - \mathbf{r}_{\text{array},k_1}||}\sin\theta, &(2.50)\\
\frac{\partial a_{k_1k_3,i}}{\partial \theta} &= -\mathrm{j}\frac{2\pi f_{k_3,i}}{c} b^{\theta}_{k_1k_3,i}\cdot a_{k_1k_3,i}, &(2.51)\\
b^{\theta}_{k_1k_3,i} &= \frac{d_x\cos\phi(d_x\cos\phi\sin\theta - R) + d_y\sin\phi(d_y\sin\phi\sin\theta - R)}{||\mathbf{r}_{\text{source}} - \mathbf{r}_{\text{array},k_1}||}\cos\theta + \\
&\quad \frac{d_z(R - d_z\cos\theta)}{||\mathbf{r}_{\text{source}} - \mathbf{r}_{\text{array},k_1}||}\sin\theta, &(2.52)\\
\frac{\partial a_{k_1k_3,i}}{\partial R} &= -\mathrm{j}\frac{2\pi f_{k_3,i}}{c} b^{R}_{k_1k_3,i}\cdot a_{k_1k_3,i}, &(2.53)\\
b^{R}_{k_1k_3,i} &= \frac{R - d_x\cos\phi\sin\theta - d_y\sin\phi\sin\theta - d_z\cos\theta}{||\mathbf{r}_{\text{source}} - \mathbf{r}_{\text{array},k_1}||} - 1, &(2.54)\\
\frac{\partial a_{k_1k_3,i}}{\partial \tau} &= -\mathrm{j}2\pi f_{k_3,i}\cdot a_{k_1k_3,i}. &(2.55)
\end{aligned}$$

Finally, the CRLB for each parameter is obtained after inverting the FIM $\mathbf{CRLB}_{\text{sp}} = \mathbf{F}_{\text{sp}}^{-1}$,

$$\begin{aligned}
\text{CRLB}(\phi_l) &= \mathbf{CRLB}_{\text{sp}(l,l)},\\
\text{CRLB}(\theta_l) &= \mathbf{CRLB}_{\text{sp}(L+l,L+l)},\\
\text{CRLB}(R_l) &= \mathbf{CRLB}_{\text{sp}(2L+l,2L+l)},\\
\text{CRLB}(\tau_l) &= \mathbf{CRLB}_{\text{sp}(3L+l,3L+l)}.
\end{aligned}$$

2.6 Summary

This Chapter summarized the composition of the UWB channel sounder. Focus of the descriptions were laid on the measurement apparatus achieving either the double- and single-directional UWB channel sounding utilizing plane and spherical wavefronts, performance criteria of the proposed channel sounder, and the theoretical background of the parametric channel modeling algorithms based on the ML-estimator. Through the UWB spatio-temporal beamforming, the fundamental resolution in detecting paths for the angular and delay domains were given for the specific array configuration and signal bandwidth of the measurements. Furthermore, acutal implementation of the proposed ML-estimator was described.

Finally, the CRLB was derived as a basis to assess the reliability of parameter estimates for two types of wavefront models: plane and spherical wavefront models.

In the next Chapter, we experimentally evaluated the performance of the proposed UWB channel sounder in an anechoic chamber.

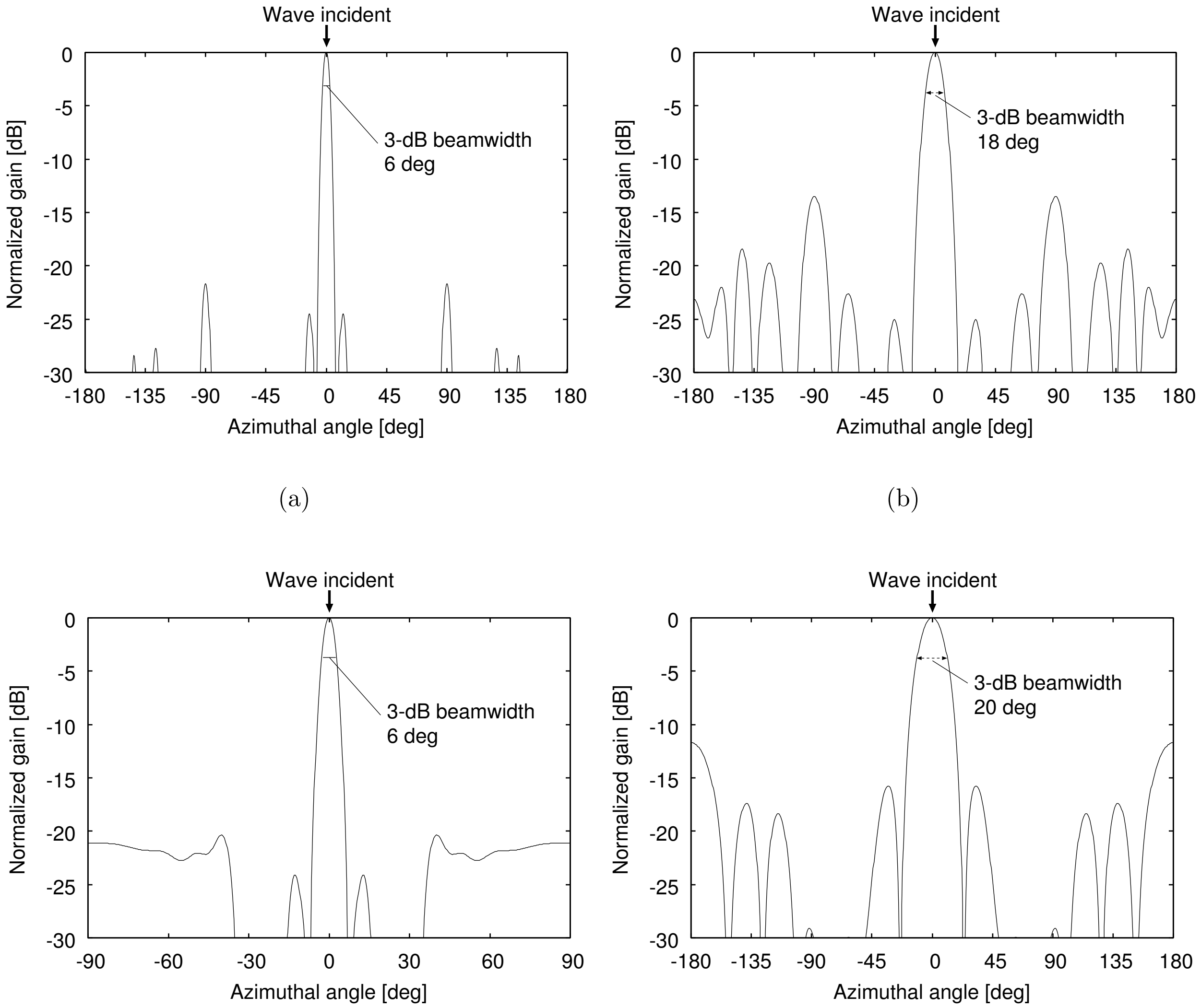

(a) (b)

(c) (d)

Figure 2.4 Synthesized azimuthal beampattern for arrays (a) to (d).

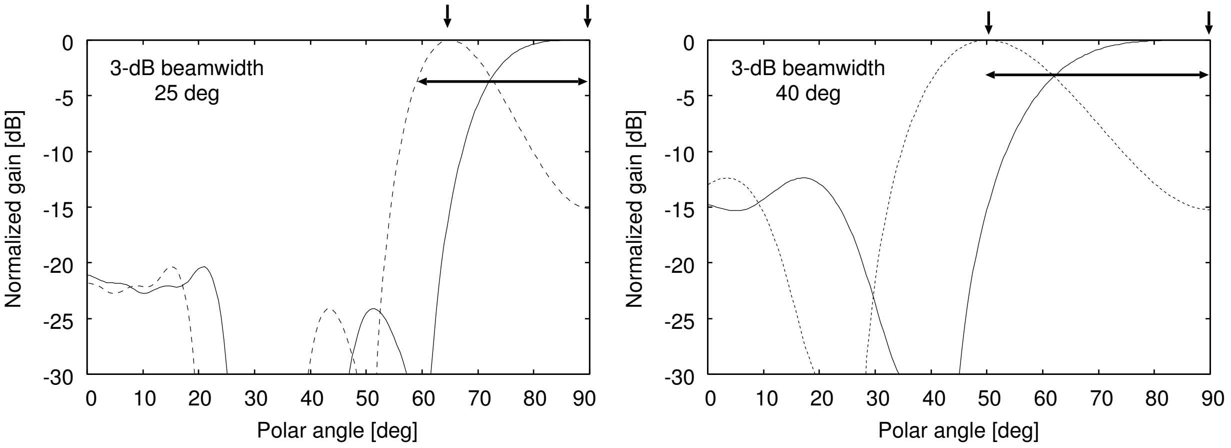

(a) (b)

Figure 2.5 Synthesized beampattern in the polar angles for arrays (a) and (b).

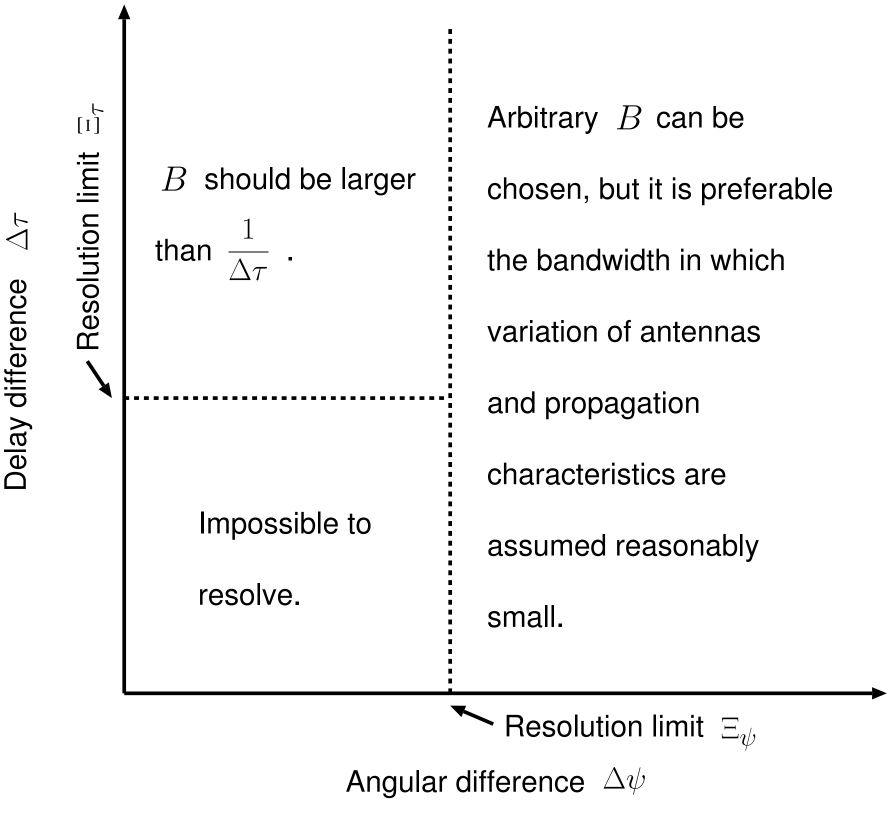

Figure 2.6 Appropriate subband B for separation of two paths which have $\Delta\phi$ and $\Delta\tau$ difference in angular and delay domains, respectively.

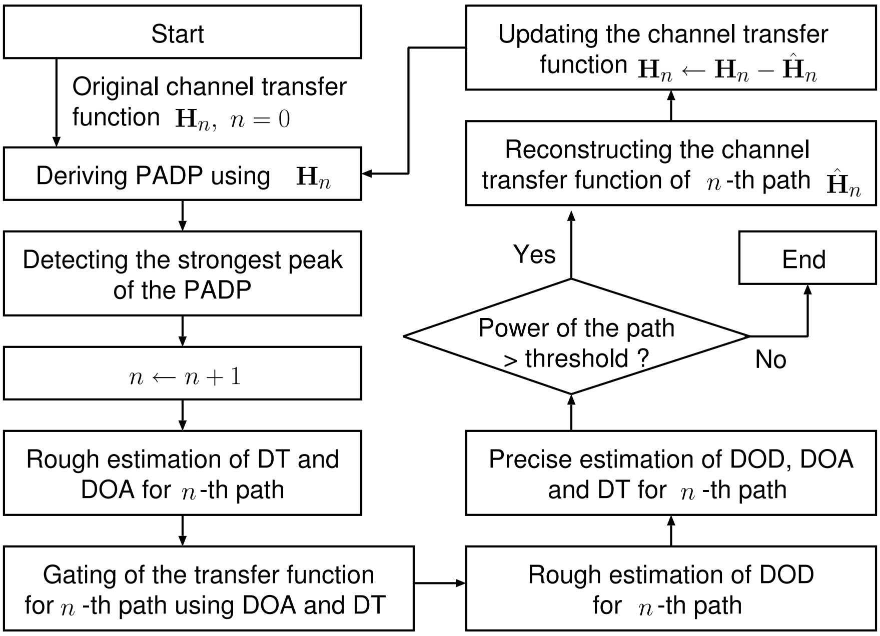

(a) Full-band case.

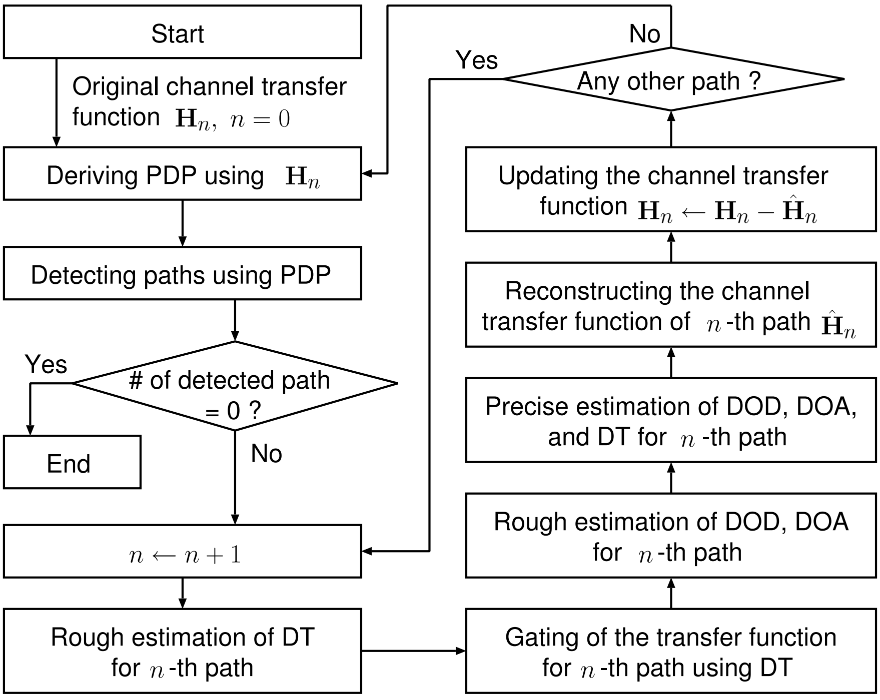

(b) Low-band case.

Figure 2.7 Flow of the ML-based estimator implemented for processing full- and low-band data.

Chapter3

Verification of the UWB Double-Directional Channel Sounder in an Anechoic Chamber

It is important to confirm the performance of the proposed UWB double-directional channel sounder before measuring and modeling actual propagation scenarios in order to assure the reliability of the resultant channel modeling results. To assesss the performance of our UWB channel sounder, measurements were conducted in an anechoic chamber [46]. Anechoic chamber is a room with its wall surrounded by electromagnetic absorber so that the propagation environment can be controlled, and even the simplest propagation scenario without multipath components *i.e.*, AWGN channels can be realized. The objectives of the measurement are:

1. To confirm the accuracy of parameter estimates using our UWB double-directional channel sounder,
2. To assess the angular and time resolution,
3. To validate the effectiveness of the subband in UWB path model to detect frequency dependent magnitude and phase in path loss, and
4. To evaluate the plane and spherical wavefront models and compare their results.

This chapter highlights the experimental specifications and results from the measurement. The following findings were obtained from each of the investigation items mentioned above:

1. The parameter estimates of propagation paths were accurate enough,
2. The path resolution capability in the angular and delay domains were as fine as the Fourier resolution,
3. The frequency dependent effect was accurately detected using the subband model, and

4. The spherical wavefront outperformed the plane wavefront in characterizing physical phenomena.

In the following, we first start from the description of the experimental setup.

3.1 Experimental Setup

Throughout the measurement campaigns presented in this Chapter, the data were collected with the measurement system depicted in Fig. 3.1. The system consisted of a VNA and a synthetic array on the Rx side. Two sources were realized on the Tx side by introducing a 3-dB power divider in assessing resolution. The relative position of the sources were arbitrarily configured. DOA of the sources was estimated on the Rx side. DOD angles were not estimated this time because of the limitation of spaces to create antenna array on the Tx side. However, as the performances of antenna array equipped on the Rx and Tx sides were independent, verification of the antenna array performance in one side of the link can also be applicable for antenna arrays equipped on another side.

The other specifications for the anechoic chamber tests are listed in Table I. The antennas used in the tests were UWB monopole antennas [79] whose characteristics were known prior to the experiment. Radiation patterns on the azimuthal plane are available in complex values. Fluctuation of the group delay is less than 0.1 ns within the measurement bandwidth. The antennas radiate vertical polarization, so the reference transfer function, Eq. (2.1), is approximately reduced as in Eq. (3.1), by substituting $D_H^{\mathrm{Rx}}(f, \mathbf{\Omega}^{\mathrm{Rx}}) = 0$ and $D_H^{\mathrm{Tx}}(f, \mathbf{\Omega}^{\mathrm{Tx}}) = 0$,

$$s(f) = \alpha(f, \tau) D_V^{\mathrm{Rx}}(f, \mathbf{\Omega}^{\mathrm{Rx}}) r_{VV}(f) D_V^{\mathrm{Tx}}(f, \mathbf{\Omega}^{\mathrm{Tx}}). \tag{3.1}$$

As back-to-back calibration was done, the impedance mismatch effects between the cables and antennas were negligible. In the following sections, all the results presented are after the removal of the antenna directivities. To remove the antenna directivities, the following procedure was carried out: 1) DOA was estimated for each path from the measurements; 2) DOD was calculated for each path after the measurements by using the antenna positions in the test scenarios; 3) complex antenna transfer function was determined for the Tx and Rx antennas using the DOD and DOA information; 4) and finally, the reference transfer function of paths obtained in the measurements were divided by the complex antenna gains, and only the propagation characteristics remain.

3.2 Evaluation of Angular Resolution

The element spacing of the synthetic array was 48 mm in the angular resolution test, which was equivalent to 0.49λ at the lowest frequency of the measurement. However, the element spacing was larger than half the wavelength in the higher frequency region which did not

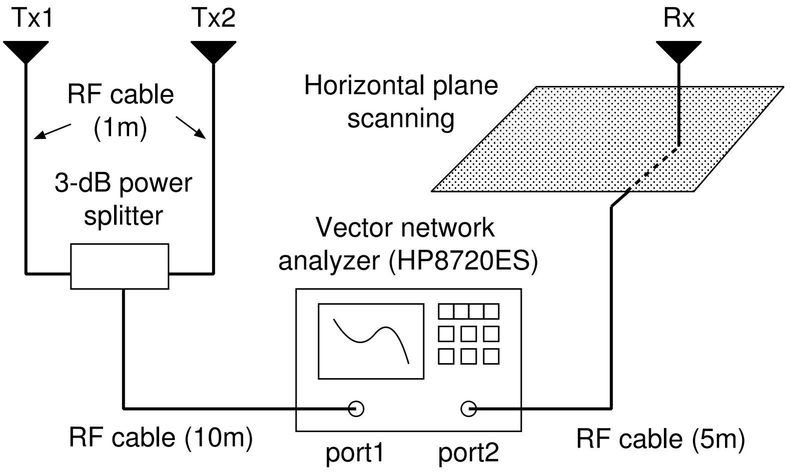

Figure 3.1 UWB spatio-temporal channel measurement system.

fulfill the sampling theorem in the spatial domain. It results in aliasing in the angular domain, but it cannot be a problem when the log-likelihood function is calculated with all the frequency domain data. As a result, angular resolution is restricted by the lowest frequency, because a constant physical aperture length corresponds to a smaller electrical aperture in the lower frequency region, ending up with a wider beamwidth and lower angular resolution. As the electrical aperture length of the synthetic array was 4.5λ at the lowest frequency, this corresponded to approximately 6 deg in the 3-dB beamwidth, which could be regarded as the inherent angular resolution of the array (see Chapter2 for the synthesized beampattern).

In the test, two paths with the same delay times and polar angles, but with 10 degrees of difference in the incident azimuthal angle of arrival were investigated for accuracy in resolution and detection. Eight hundred MHz was chosen for the subband, but almost the same results were obtained for an arbitrary bandwidth for the subbands. We assumed the spherical wavefront model to estimate the angles. The estimated parameters for the two paths are listed in Table II. The theoretical values are also listed in parenthesis, which were calculated from the Tx and Rx positions in the scenario. In Fig. 3.2, we can see the estimated reference transfer functions and theoretical values for each path. The theoretical characteristics were calculated from Friis' transmission formula described in Eq. (2.2). The estimated magnitude and phase of the spectrum agreed well with the theoretical characteristics. These results proved that the approach could achieve an angular resolution that is close to the Fourier resolution.

3.3 Evaluation of Temporal Resolution

Since the measurement system used the 7.5 GHz bandwidth, inherent Fourier resolution in the delay domain was 0.13 ns, which is equivalent to 4 cm. However, in the time resolution tests,

Table 3.1 Specifications for anechoic chamber tests.

Bandwidth	3.1 to 10.6 GHz.
Frequency sweeping points	801.
Spatial sampling	10 × 10 points in horizontal plane. Element spacing is 48 mm, which is less than half the wavelength at 3.1 GHz.
Estimated components	DOA azimuth, polar angles, curvature radius, delay time, and magnitude and phase of the reference transfer function.
Antennas	UWB monopole antennas [79].
Polarization	Vertical–vertical.
SNR at receiver	About 25 dB.
Calibration	Internal function of the VNA, Back-to-back, the distance between Tx and Rx is 5.0 m.

two different paths 0.67 ns (20 cm) apart were examined because the size of antennas prevented us from placing the antennas closer than that distance, and also to avoid electrical coupling of the two sources. Following the criteria in Fig. 2.6, the value of bandwidth for the subband B was selected as a fraction of the delay time difference, *i.e.,* $\frac{1}{\Delta\tau} = 1.5$ GHz. The results for estimating the parameters and spectrum are listed in Table III and Fig. 3.3, respectively. The results revealed that the two paths were accurately separated, while spectrum extraction partly failed in the highest and lowest frequency regions. This is due to the limited bandwidth of the measurement. As we stated before, estimation of the reference transfer function at a certain frequency $f_{\mathrm{c}i}$ requires log-likelihood function spanned in bandwidth $(f_{\mathrm{c}i} - \frac{B}{2}) \leq f_{\mathrm{c}i} \leq (f_{\mathrm{c}i} + \frac{B}{2})$. However, it is obvious that a sufficient bandwidth of subband B to resolve two paths is not assured if $f_{\mathrm{c}i}$ is within the highest and lowest frequency regions of $f_{\mathrm{min}} \leq f_{\mathrm{c}i} < (f_{\mathrm{min}} + \frac{B}{2})$ and $(f_{\mathrm{max}} - \frac{B}{2}) < f_{\mathrm{c}i} \leq f_{\mathrm{max}}$, respectively. f_{min} and f_{max} denote the lowest and highest frquency of the measurement frequency band. In the experimental results, the bandwidth where spectrum estimation was incorrect was $\frac{B}{2} = 0.75$ GHz and 1.2 GHz for the first and second detected paths, respectively. The wider bandwidth in the second path was due to over-estimating of the power for detecting the first path in the lowest and highest frequency regions. Furthermore, we conducted additional time resolution tests with $\Delta\tau$ varied from

Table 3.2 Parameters estimated in the angular resolution test. Theoretical values are shown in parentheses.

	Azimuth [deg]	Polar [deg]	Delay [ns]	Curvature radius [m]
#1	0.40	87.70	16.67	5.30
	(0.00)	(86.57)	(16.70)	(5.01)
#2	10.20	88.90	16.67	4.95
	(10.00)	(86.57)	(16.70)	(5.01)

Table 3.3 Parameters estimated in the time resolution test. Theoretical values are shown in parentheses.

	Azimuth [deg]	Polar [deg]	Delay [ns]	Curvature radius [m]
#1	0.30	87.90	16.00	4.75
	(0.00)	(86.42)	(16.03)	(4.81)
#2	0.30	88.80	16.67	5.10
	(0.00)	(86.57)	(16.70)	(5.01)

0.67 to 2.00 ns, *i.e.*, from 20 to 60 cm, and determined the bandwidth B_I where spectrum estimation failed. The result is shown in Fig. 3.4. The results indicated that the first detected path closely agreed with the $B_I = \frac{1}{2\Delta\tau}$, while those for the second path indicated larger values than for the first paths, but smaller than $B_I = \frac{1}{\Delta\tau}$.

3.4 Robustness of Wavefront Models

It is often the case in indoor scenarios that spherical incidence of paths seems more realistic than with the plane wavefront model. However, even if complicated signal models are used, there is always signal model error. The more the signal model deviates from the physical propagation phenomena, the more significant the errors in estimating model parameters. Specifically, the error appears as a spurious path, which cannot be identified in real environments. The spurious paths often prevent us from accurately detecting weaker paths, making it difficult to investigate the physical phenomena correctly.

Here we will present one example that estimates paths incident from azimuth 0 deg (#1) and 15 deg (#2). Plane and spherical wavefront models were assumed in estimating the angles, and their performance was evaluated and compared. Note that the power for source #2 was

20 dB weaker than that for point source #1 by using an attenuator for source #2. After the stronger path, #1, was successfully detected and removed, the log-likelihood function was calculated to detect source #2. Figure 3.5 plots the results of the calculation using both wavefront models. The peak appeared in the direction of the true source with the spherical wavefront model, while the plane wavefront model failed to detect source #2, due to its larger response at ±5 deg, which seemed to be the residual components of source #1. In this case, the parametric channel estimator regards the peak at 5 deg as the second strongest source, resulting in the production of a spurious path. Spurious paths were detected even for the third path, and finally the true source was detected in the fourth detection. This indicates that the spherical wavefront model expresses the physical propagation phenomena more precisely.

The robustness of the spherical wavefront model can also be evaluated with respect to the residual power after paths are detected and extracted. If the residual power is limited, this indicates that the signal model fits the measured data well. In contrast, greater amounts of residual power mean greater deviations in the signal model. We detected a single path by using antenna array with several aperture sizes in the anechoic chamber tests. Both spherical and plane wavefront models were used as signal models, and residual power after the extraction of the path was evaluated. The results are plotted in Fig. 3.6. We can see that the spherical wavefront model always accomplishes less residual power, regardless of the size of the array. Furthermore, the residual power increases monotonically as the array size increases, indicating that a larger array results in larger signal model deviations from the measured data.

It is again worth mentioning that the plane wavefront is considered as a special case in the spherical wavefront, since they are equivalent as curvature radii of the spherical model approaches infinity. However, estimating large curvature radii may result in large errors, due to the small gradient of the log-likelihood function. In iteratively calculating the log-likelihood in the ML-based estimator, a small gradient often results in more iterations until convergence to stationary points, which is burdensome in terms of calculations.

In order to assess the accuracy of parameter estimates depending on the curvature radius, we derived the $\sqrt{\mathrm{CRLB}}$ and corresponding RMSE for various length of curvature radii, and compared the results. The derivation was performed under the conditions that two resolvable paths are incident to URA. The two paths have different azimuthal angles by 10 deg and common polar angles, curvature radius, and delay time, which is the same condition as the angular resolution test reported in Chap. 3.2. Frequency range and array configuration were the same as anechoic chamber test (see specification of the test, Table 3.1). Other setup of parameters is summarized in Table 3.4. $\sqrt{\mathrm{CRLB}}$ was calculated using the formula established in Chap. 2.5.2, and RMSE were calculated based on Monte-Carlo simulations. The Monte-Carlo simulation here refers to trying the parameter estimation many times using snapshots generated by different realization of noise.

Figure 3.8 shows $\sqrt{\mathrm{CRLB}}$ and RMSE for the curvature radius ranging from 1 to 100 m. The values plotted in the figure were obtained from path #1. It was found that RMSE was always lower than $\sqrt{\text{CRLB}}$ because of the characteristics of the ML-based estimator. By taking fine local search in each parameter domain, resultant RMSE can be even lower than $\sqrt{\text{CRLB}}$ as reported in [21]. In our implementation of the fine local search, the interval of parameter search in each domain was set to 0.1 deg, 0.05 m and 0.01 ns in the angular, curvature radius, and delay domains.

Looking at Fig. 3.8, the curvature radii revealed large estimation variances and RMSE especially when $R > 10$ m, while other parameters had almost constant variance and RMSE regardless of the value of curvature radius. The mean RMSE for azimuthal and polar angles were 0.7 and 0.07 deg, and the mean RMSE for the delay time was 2.5×10^{-3} ns. The RMSE of the curvature radius for 10 m and 100 m was 1 m and 25 m respectively, but these values were largely dependent on the implementation of the estimator.

It can be seen from the results that the estimation error of curvature radius was not significant in most of the indoor radio channel modeling, since the distance between scattering objects and terminal antennas, or between terminal antennas were several tens of meters at most. Still, we must also bear in mind that the accurate results yielded by the spherical wavefront model are achieved at the expense of increasing the computational burden.

Table 3.4 Conditions of calculating CRLB and simulation RMSE.

	Path #1	Path #2
Azimuthal angle ϕ [deg]	180	170
Polar angle θ [deg]	80	80
Curvature radius R [m]	1 to 100	1 to 100
Delay time τ [ns]	30	30
Signal-to-noise ratio [dB]	30	30

3.5 Resolving Paths Exceeding the Inherent Fourier Resolution

It is a matter of interest how the algorithm behaves in the detection of two incident paths, which are closer in the angular-delay domain than the inherent Fourier resolution. For example, the results of estimating the spectrum for two paths, which have 5 deg different azimuthal incidences but no delay or polar differences, are plotted in Fig. 3.7. As the angular difference was less than the inherent Fourier resolution, the spectrum for the second path was underestimated, as a consequence of overestimating the power for the first path. However, angle and delay parameters were accurately estimated. Note that a multi-dimensional spatio-temporal channel estimation will offer much higher resolution than the single dimensional estimation. This is one of the advantages of using multi-dimensional channel estimation.

3.6 Accuracy of Parameter Estimates in Endfire Direction

By employing a horizontal synthetic array on the Rx side, paths may be incident from the endfire direction of the array. The endfire direction refers to the direction where the effective size of antenna aperture is minimum, resulting in the lowest capability to resolve paths and estimate parameters accurately due to the wide beamwidth. In case of a horizontal array, polar angle around 90 deg corresponds to the endfire direction. In fact, the results of anechoic chamber tests revealed deviating estimates of polar angles from theoretical values due to the endfire incidence of paths. $\sqrt{\text{CRLB}}$ and corresponding RMSE were again calculated for the parameter estimates by assuming endfire incident of propagation paths. Here it is also assumed that two resolvable paths having parameters in Table 3.6 are incident to URA. Frequency range and antenna configuration were the same as the anechoic chamber test.

Calculated $\sqrt{\text{CRLB}}$ and RMSE for angular parameters, curvature radius, and delay time are shown in Fig. 3.9. It was again found that RMSE was always less than $\sqrt{\text{CRLB}}$ due to the implementation of the ML-based estimator. As expected, large polar angles, *i.e.,* incidence of paths from endfire direction, resulted in large errors of parameter estimates. Theoretically the polar angle estimates around 90 deg revealed huge variance, but actually the RMSE was about 1 deg in our implementation, since the path was resolved in other parameter spaces. For other parameters, RMSE does not drastically change depending on polar angles, and the mean RMSE was 0.1 deg, 0.3 m, and 4.0×10^{-3} ns for the azimuthal angle, curvature radius, and delay time.

Table 3.5 Conditions of calculating CRLB and simulation RMSE.

	Path #1	Path #2
Azimuthal angle ϕ [deg]	180	170
Polar angle θ [deg]	70 to 90	70 to 90
Curvature radius R [m]	5	5
Delay time τ [ns]	30	30
Signal-to-noise ratio [dB]	30	30

3.7 Summary

This Chapter presented the results from anechoic chamber tests assessing the performances of the UWB channel sounder. The following aspects were confirmed from the tests:

1. Angular and time resolution of the sounding system approaches the inherent Fourier resolution of the measurement which are determined by the size of antenna aperture and signal bandwidths;
2. Frequency dependent magnitude and phase in path loss is accurately detected as long as paths were resolved; and
3. Spherical wavefront model can outperform the plane wavefront model given the short-range environment of anechoic chamber.

Using the sounder, it is possible to analyze the propagation phenomena in detail even in indoor propagation scenarios which reveal rich multipath environment. The fine angular-delay resolution capability sometimes achieves the detection of “a single wave”. The capability of the proposed channel sounding system and its results are to be dedicated to the channel modeling activities, as described in Chapter4.

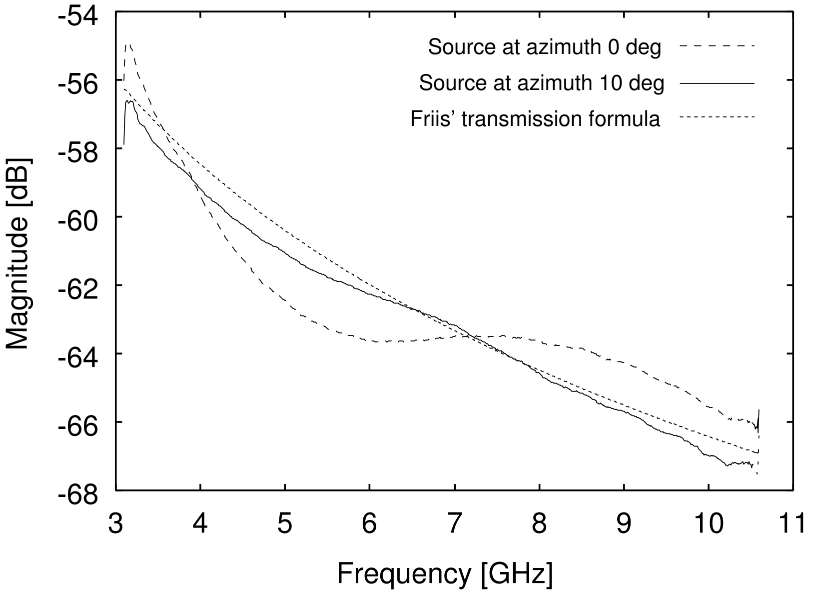

(a) Amplitude.

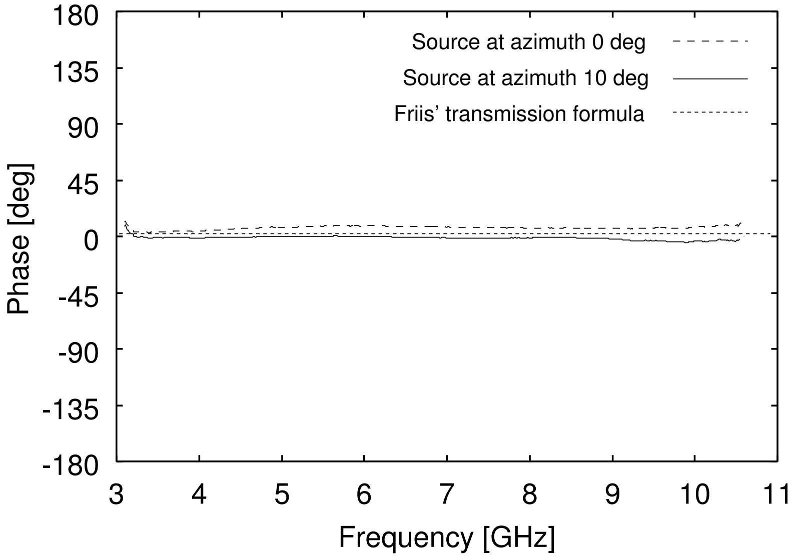

(b) Phase.

Figure 3.2 Results of estimating spectrum in the angular resolution test: two paths with the same delay times but 10-deg difference in DOA azimuthal angles.

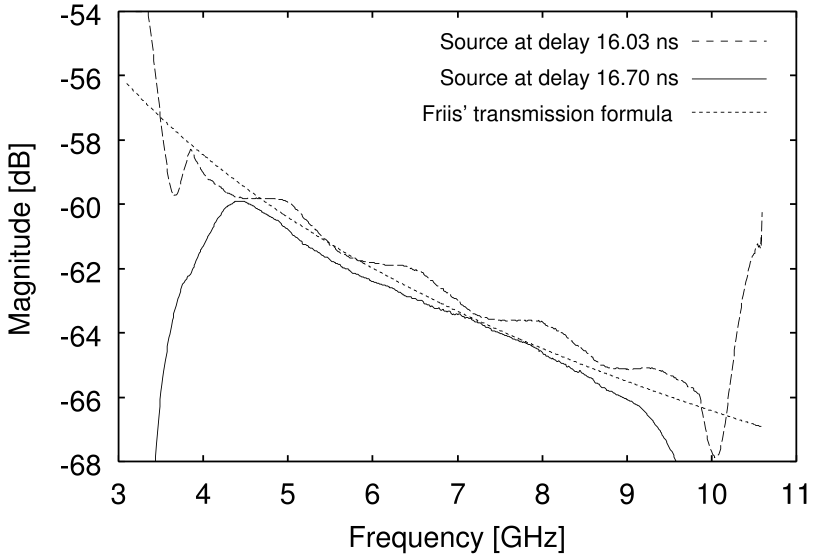

(a) Magnitude.

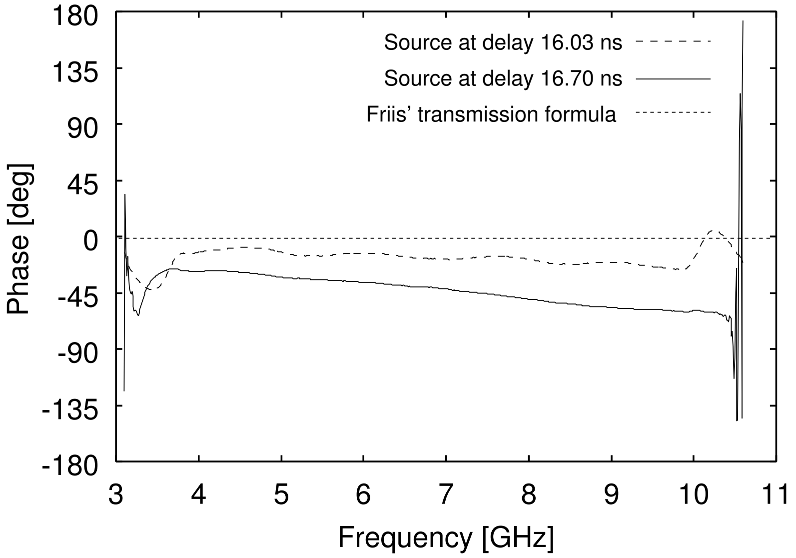

(b) Phase components.

Figure 3.3 Result of estimating parameters in the time resolution test: two paths with the same DOAs but different delay time of 0.67 ns.

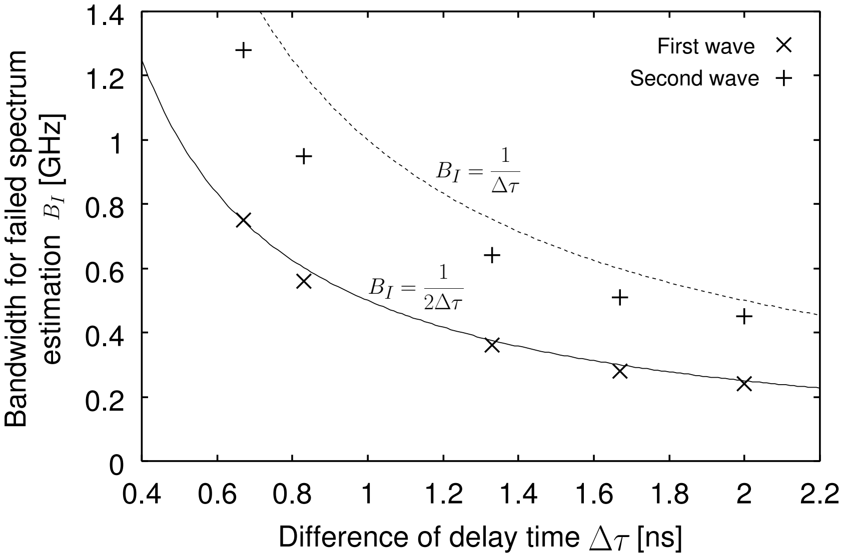

Figure 3.4 Relation between difference in delay time and bandwidth in which spectrum estimation fails.

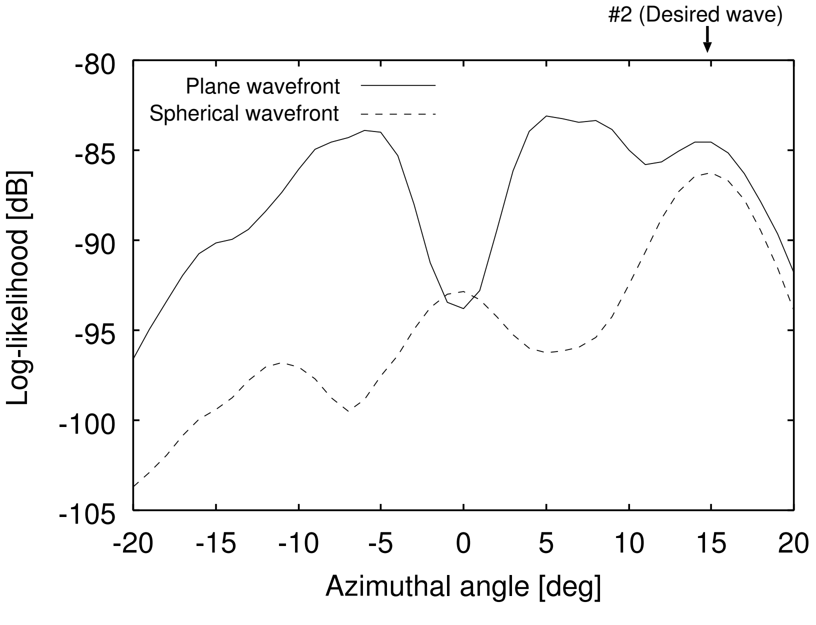

Figure 3.5 Log-likelihood spectrum in the angle domain for the detection of source #2 (weaker source).

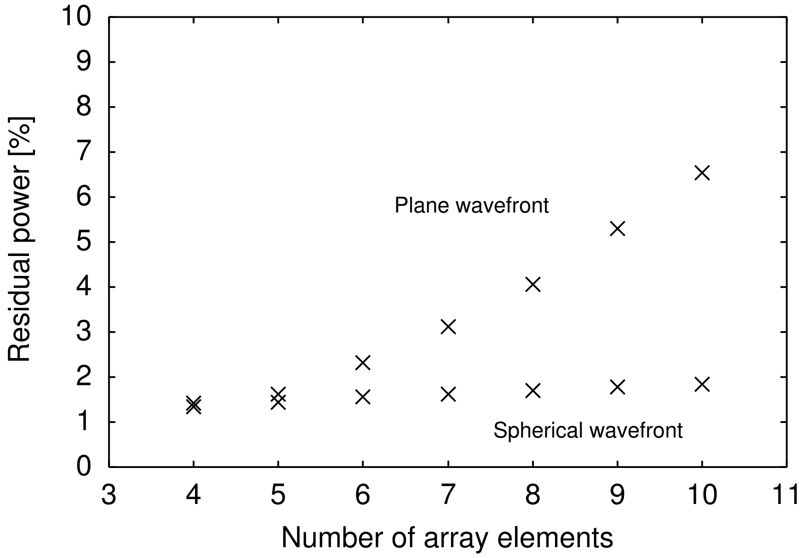

Figure 3.6 Residual power after detecting a single path.

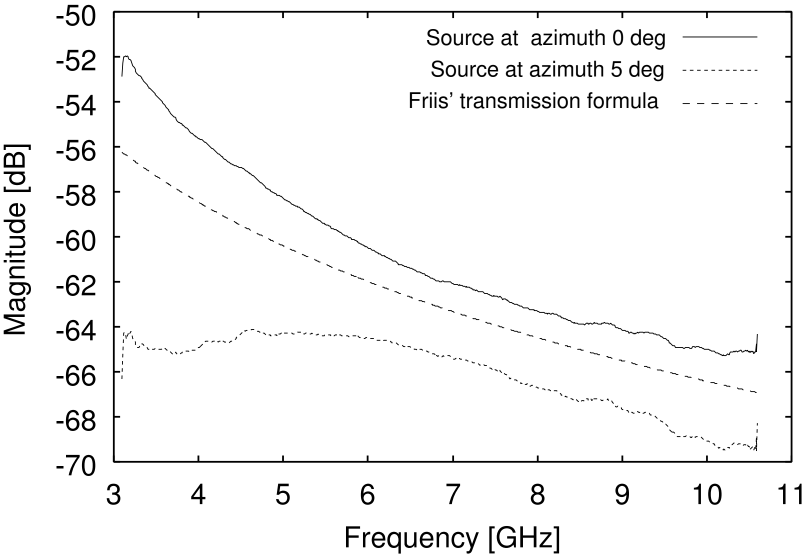

Figure 3.7 Estimated spectrum of two paths which have closer spatial characteristics than the inherent Fourier angular resolution, and no delay difference.

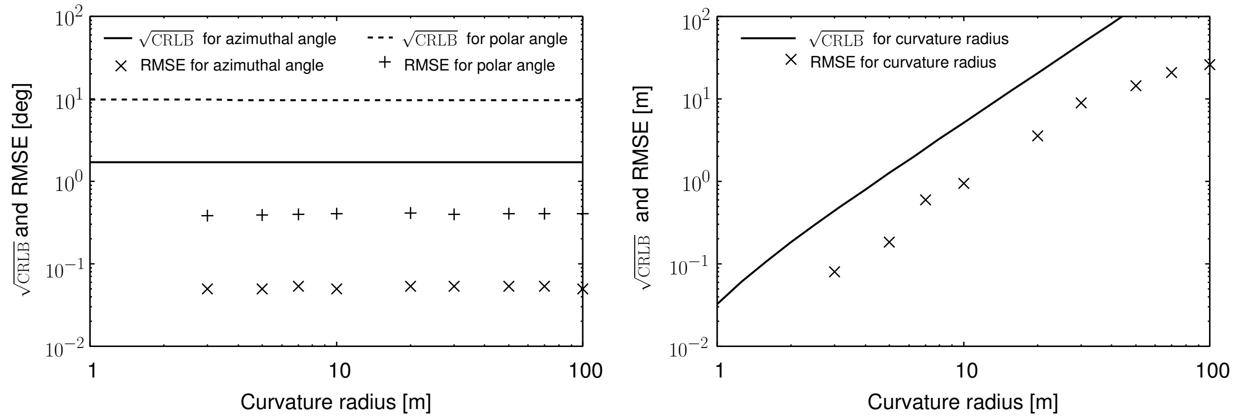

(a) Azimuthal and polar angles.

(b) Curvature radius.

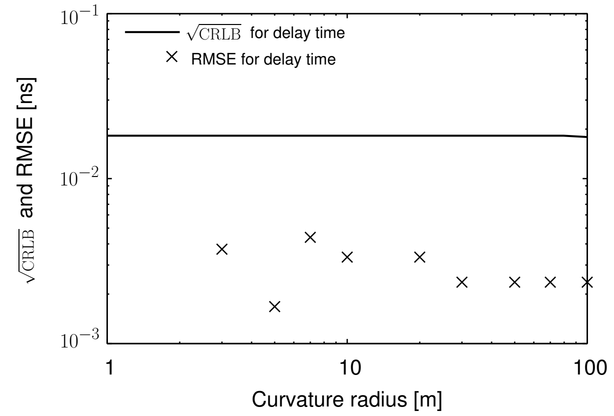

(c) Delay time.

Figure 3.8 $\sqrt{\mathrm{CRLB}}$ and RMSE for the curvature radius ranging from 1 to 100 m. Two resolvable paths were considered for the derivation.

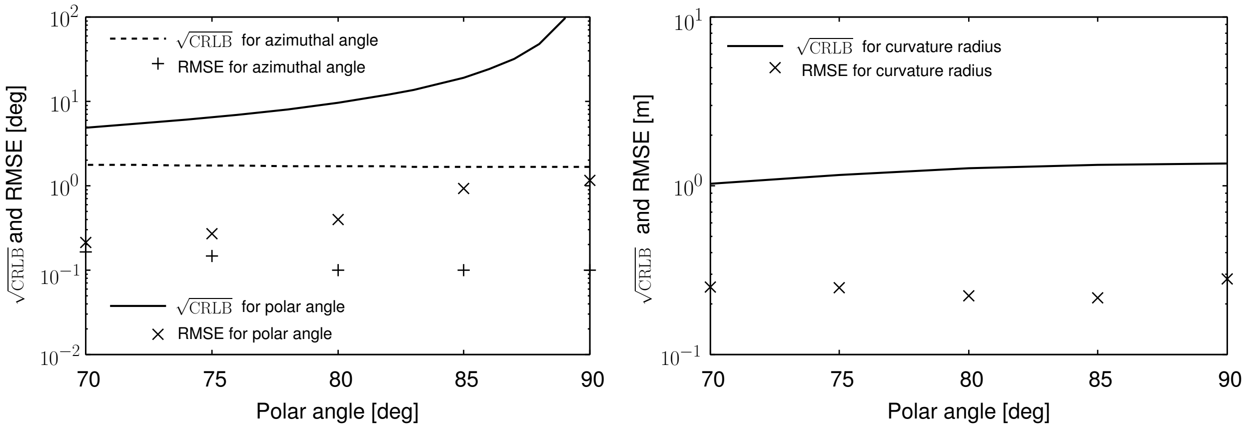

(a) Azimuthal and polar angles.

(b) Curvature raidus.

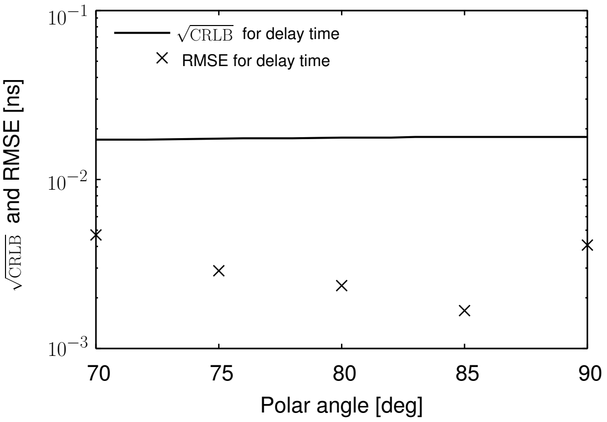

(c) Delay time.

Figure 3.9 $\sqrt{\mathrm{CRLB}}$ and RMSE for the polar angle ranging from 70 to 90 deg. Two resolvable paths were considered for the derivation.

Chapter4

Cluster-based Analysis and Modeling of UWB Double-Directional Radio Channels in Home Environments

Having confirmed the performance of the proposed UWB double-directional channel sounder, this Chapter presents the results from channel sounding and propagation modeling in a Japanese wooden house. Home environments are considered as one of the most popular scenarios where WPAN systems are to be installed. However, other propagation measurements and modeling targeting WPAN applications, namely covering UWB bands, mainly investigated office [20, 22–24, 36, 39, 43] and industrial [44, 47] environments, and therefore, it is obvious that channel measurements and propagation modeling is required in home environments. Another aspect that motivated our channel sounding campaign is related to the separation of propagation channels and antenna properties. Antennas are considered as a source of waveform distortion [76], necessitating propagation models that do not include antenna properties used in the channel sounding campaign. The double-directional channel sounding and propagation modeling is a known method to achieve separation of propagation behavior and antenna properties. The method enables us to develop channel models that expresses only propagation behavior. It is obvious that the double-directional sounding and propagation modeling is essential in UWB systems, but none of the measurements dedicating to the WPAN applications have tried this.

This measurement covered several scenarios in home environments: line-of-sight (LOS) scenario where Tx and Rx antennas were placed in the same room, and inter-room, inter-floor, room-to-corridor, and indoor-to-outdoor propagation channels revealing non-LOS (NLOS) scenarios. In all the measurement scenarios, the settings of the UWB double-directional channel sounder, such as the antenna configurations and bandwidth were common as shown in Table 4.1. Characterization and modeling of propagation phenomena were performed using clustering of propagation paths. As this method is the most popular way in characterizing angular-delay properties of propagation channels, the modeling results have a compatible form with many standardized channel models. Modeling results from our channel sounding and propagation modeling were contributed to the IEEE802.15.4a standard channel model [64] and COST273 MIMO channel model [66] as representative parameters for home environments.

First, this Chapter starts from introducing the environment where UWB double-directional channel sounding and propagation modeling were performed.

4.1 Environment under Consideration

The measurement was conducted inside a Japanese wooden house. The floor plan of the house is depicted in Figs. 4.1. Tx and Rx positions, definition of coordinates, and azimuthal angles are shown as well. The Tx URA was parallel to the x-axis when it was inside the house, and it was parallel to the y-axis when it was outdoor. The environment contained a small number of furnitures, such as desks and chairs. A total of seven environments were specifically considered, which included line-of-sight LOS, NLOS, and obstructed-LOS (OLOS) channels. The OLOS channel refers to the scenarios where only the first Fresnel zone spanned by the Tx–Rx line was shadowed by obstacles, and can be seen as scenarios in between the LOS and NLOS scenarios. These environments and measurement settings are described as follows.

- LOS environment (Tx1–Rx1)

  The antennas were placed in the same room of the first floor of the house. The Tx and Rx antennas were mounted 1.30 and 1.00 [m] respectively above the floor. Between the phase center of the Tx and Rx array was a horizontal distance of 5.00 m.

- Room to corridor environment (OLOS: Tx2–Rx1)

  The Tx antenna was placed in the corridor while the Rx antenna was located in a room with the door left opened. A wall slightly obstructed the line-of-sight path. The Tx and Rx antennas were mounted 1.30 and 1.00 [m] respectively above the floor, and the horizontal distance between the phase center of the Tx and Rx array was 5.59 m.

- Room to corridor environment (NLOS: Tx2–Rx1)

  The same channel in the room-to-corridor OLOS measurement except that the door was shut.

- Inter-room measurement (NLOS: Tx3–Rx2)

  A room-to-room propagation on the second floor of the house with all doors shut. The Tx and Rx antennas were mounted 1.30 and 1.00 [m] respectively above the floor, and the horizontal distance between the phase center of the Tx and Rx array was 5.00 m.

- Inter-floor measurement (NLOS: Tx4–Rx3)

  The Tx antenna was placed on the first floor while the Rx antenna was put on the second floor of the house. The Tx and Rx antennas were mounted 1.30 and 0.50 [m] respectively above each floor, and the horizontal and vertical distances between the phase center of the Tx and Rx arrays were 5.00 and 2.07 [m], respectively.

- Indoor to outdoor measurement without shutters (OLOS: Tx5–Rx4)

  The Rx antenna was placed on the first floor of the house, while the Tx antenna was located outside the house. The channel was OLOS due to the wall between the Tx and Rx. Metal shutters which cover sliding doors were not used in the measurement. Tx and Rx antennas were mounted 1.50 and 1.00 [m] above the road surface and the floor respectively, which results in 1.00 m difference of the absolute height between the Tx and Rx. The horizontal distance between the phase center of the Tx and Rx array was 5.00 m.

- Indoor to outdoor measurement with shutters used (NLOS: Tx5–Rx4)

  Metal shutters were used in the same settings as the indoor-to-outdoor OLOS measurement, so the channel became NLOS.

The walls inside the house are made of plaster boards, and contain metal reinforcements, while the windows and sliding doors consist of glass and metal frames. The measured channels can be representative scenarios in the deployment of UWB systems.

4.2 Propagation Paths Identification and Clusters

4.2.1 Extraction of Propagation Paths and Its Clusterization

From UWB double-directional sounding conducted in each scenario, more than 50 paths were extracted using the ML-based estimator. The SIC-type path detection can estimate quite large number of propagation paths, but it was found not all the detected paths were meaningful because 1) most of propagation paths after extracting 70 paths and more contained less than 0.1% of the total received power, which had no significant contribution to the power transmission from Tx to Rx; and 2) the parameter estimates of propagation paths were not always reliable due to the low signal-to-noise ratio and the error propagation in the SIC-based path detection. Thus we decided to use propagation paths having more than 0.1% of the total received power for the analysis of propagation paths.

After the antenna deconvolution conducted for each propagation path using directional information on both sides of the link, the paths were then classified into clusters. As commonly practiced in propagation modeling, we also found that distribution of propagation paths over the DOA azimuth – DOD azimuth – delay domain formed multiple clusters. A path distribution actually obtained from the NLOS inter-room scenario is shown in Fig. 4.2 for example.

Clusters were extracted by a heuristic approach to collect propagation paths having similar DOA azimuth, DOD azimuth, and delay time. In the exmaple, clusters A to E have no obvious boundary with each other on the DOA–DOD map so that they may be classified into an identical cluster. However, they were in fact distinct clusters if looking at different map, namely DOA–delay domain. By virtue of the multi-dimensional analysis, detailed classification of propagation paths into clusters were possible as shown in this example. DOA polar angles were not taken into consideration in the clusterization, because we used the URA on the Rx side resulting in the ambiguity of polar angles. Furthermore, if the detected cluster had less than 1.0% of the total power, it was not used for further analysis. In contrast, propagation paths that existed without associated paths and did not belong to any cluster, *e.g.*, direct waves in the LOS environment, were treated as "a singular path" as far as it had more than 1% of the total received power. In a later description of the measurement results, specific explanation will be given for singular paths.

Here we first discuss about the accuracy of the parameter estimates based on the CRLB. Next, we present clusterization and its path identification results on floor plans in each scenario. Finally, findings from path identification results are summarized.

4.2.2 Accuracy of the Parameter Estimates

Given the array structure on the Tx and Rx sides and available samples of transfer functions, we derived $\sqrt{\mathrm{CRLB}}$ for estimated parameters in our experiment by assuming that the parameters are unbiased. According to the formulation of CRLB in Chapter2, we obtained $\sqrt{\mathrm{CRLB}}$ as shown in Table 4.2. The values are the median of $\sqrt{\mathrm{CRLB}}$ derived from all propagation paths in each scenario. Table 4.2 shows that $\sqrt{\mathrm{CRLB}}$ is less than 4.0 deg and 1.5×10^{-2} ns in DOD/DOA azimuthal angles and delay time, respectively. Large $\sqrt{\mathrm{CRLB}}$ was observed in the indoor-to-outdoor measurements because some paths were estimated with signal-to-noise ratios of around 0 dB. However, more than 80 % of the paths revealed small $\sqrt{\mathrm{CRLB}}$ as the values indicate in Table 4.2. Practically, these values are accurate enough for propagation path identification, given the distance between Tx and Rx antennas and the surrounding objects in the measurement environments. In addition, considering that these values are as small as one-tenth of the angular and delay resolution of the channel sounder, obtained parameter estimates are sufficiently accurate that enable us to further conduct quantitative analyses on clusters in later subsections. In contrast, DOA polar angles revealed larger values because angle estimation was often conducted in endfire directions. Particularly, indoor-to-outdoor scenarios resulted in $\sqrt{\mathrm{CRLB}}$ greater than 10 deg, thus we excluded DOA polar angles in the subsequent cluster analyses.

4.2.3 Results from the LOS Scenario

Path identification results for the LOS scenario are shown in Fig. 4.3. The figures consist of propagation path distribution on the DOA–delay and DOA–DOD domain. In the path distribution map, extracted clusters are also identified by showing cluster boundaries. The total propagation paths were classified into 7 clusters. In Fig. 4.3(d), the strongest propagation paths belonging to the clusters are shown on the floor plan. It was found that all the strongest paths were made up of mirror-like specular reflection, and specular diffraction where the Keller's law held. Figure 4.3(c) is a colormap showing the power spectrum of the residual components after all propagation paths were subtracted. The spectrum revealed no significant peaks but still had wide dynamic range over the noise level. The power level of the spectrum was high where cluster existed in the corresponding DOA–delay domain. Accordingly, the power distribution of the residual spectrum and propagation paths had some correlation with each other. The residual component represents mainly signal components that was not fitted, modeled, and subtracted as propagation paths due to the finite angular-delay resolution and incompleteness of underlying signal models in the parametric propagation modeling algorithm. We can alternatively call the residual spectrum distributed diffuse scattering due to the dense multipath components having very weak power [53, 54].

4.2.3.1 Cluster Composition

Among the detected clusters, clusters A, B, and C were reflections from the window behind the receiving antenna. The strongest path in cluster B was first-order reflection, while other propagation paths belonging to the clusters might experience reflection more than once. Cluster A included propagation paths experiencing sliding door and window reflections. Cluster B contained window and ceiling / floor reflections, and cluster C was composed of display / window reflected waves. Even for the higher order reflections, the propagating paths were dominated by specular paths. Cluster D had one strong component associated with several weak paths and they arose from specular diffractions from the edges of the windows and displays. Cluster E had wider range of the azimuth angle of arrival corresponding to the distributions of reflection objects, *i.e.*, displays and small desks near the wall. Propagation paths having longer delay within cluster E experienced ceiling or floor reflections. Cluster F had the largest number of paths in the detected since it included several types of propagation paths, such as 1) reflection from the wooden door behind the transmitting antenna, 2) reflection from ceiling or floor, and 3) wooden door / ceiling twice-reflected waves. As they have the same incident azimuth angles and closer delays, it is difficult to divide them into different clusters without polar angles. Cluster G consisted of scattering from walls, glass, and the metal frames of the sliding door. As the reflection objects had spatially wide distribution, the range of incoming signals was also wider than other clusters, but was almost the same value as cluster B.

4.2.3.2 Cluster Properties

Table 4.3 lists cluster properties composed of 1) cluster DOA azimuthal angular spread, 2) cluster delay spread, 3) percentage of the cluster power relative to the total received power, 4) minimum scattering loss of propagation paths belonging to each cluster, and 5) scatterer identification result. The analysis revealed the following findings.

1. **Cluster angular and delay spread was less than 6 deg and 1.7 ns, respectively.**

   The DOA azimuthal angular spread and the delay spread are the second order moment of path distribution within the cluster. Ideally, angular and delay analysis should not be carried out individually since they were highly correlated. However, it was found that determining the probability density function (PDF) for the spatio-temporal cluster shape was impossible because 1) huge amount of cluster samples were required to derive it, while our data set was far from satisfactory to accomplish it; and 2) the derivation of the probability density function is a stochastic analysis so that the shape of every cluster reflecting the size and dimension of scatterer and the distance between the objects and antennas, were eventually vanished. It can thus be reasonable to treat the angular and delay domain properties individually in the stochastic analysis of clusters; while our analysis focused more on the derivation of cluster properties in a deterministic manner in order to relate the results with the physical phenomena. Based on the discussion, we decided to derive the general spread parameters for each cluster. It means that we did not consider any distribution function of paths within each cluster: The Laplacian distribution [30,52] and the exponential distribution [20,35] are the popularly used PDF to model intra-cluster path distribution in the angular and delay domains, respectively. However, we did not consider any specific PDF in our derivation because the distribution is obtained through stochastic approach, contradicting the treatment in a deterministic manner.

   According to the results from DOA angular spread, clusters B and E revealed larger values probably because the clusters arose from a single large object or distributed small scatterer. Most of the angular spread within the clusters was less than 5 deg and the delay spread was at a maximum of 1.5 ns. The spread parameters were also derived for other parameters, such as DOD azimuthal angles and DOA polar angles, but not being shown in the table. The results revealed that DOD azimuthal spread took almost the same range as DOA azimuthal spread. Whereas DOA polar spread showed much larger values because polar angles were not used for the cluster extraction, most of the clusters included both paths experiencing ceiling/floor reflection and paths without experiencing them. Ambiguity of polar angle estimates using URA also affected the large spread values.

2. **Clusters composed of single reflected propagation paths carried majority of**

power.

Table 4.3 also lists the percentage of power occupied by each cluster. The direct wave contains 28.3 % of the total received power. Clusters E and F had relatively stronger power than other clusters, since majority of propagation paths composed of the clusters were the single reflected paths. Other clusters revealing smaller power composition mainly consisted of propagation paths experiencing more than single bounce. The residual components after the subtraction of propagation paths still carried 23.0 % of the total received power, which was a comparable amount of power as the direct path. It should be noted that the sum of the percentage of power contained in each cluster did not always reach 100 % (in this case, 95.2 %). This was because the complex amplitude of propagation paths and residual components were coherently added when computing the total power, while the total in terms of percentage did not take phase components into consideration.

3. **It is reasonable to assume the scattering loss takes almost the same value over the considered bandwidth.**

We finally discuss scattering coefficient of propagation paths. Results from this measurement revealed that the path loss of the LOS component followed the Friis' transmission formula [80]. Applicability of the Friis' formula implies that each individual path detected in the experiment did not suffer from fading. From the observation, scattering losses of a single path which came from reflections, diffractions, and penetrations can be derived by removing the free space path loss from the gain of propagation paths obtained in the propagation modeling. Deconvolution of antenna gain was done in the final process of the propagation modeling.

Frequency characteristics of the scattering loss $L_{\mathrm{sc}}(f)$ is shown in Fig. 4.4. Among many propagation paths belonging to each cluster, we chose the paths showing the minimum scattering loss. Here we show only the magnitude, but the phase component was almost the constant characteristics over the considered band. In addition, the mean scattering loss was derived by integrating scattering loss over the considered bandwidth,

$$L_{\mathrm{sc,m}} = 10\log_{10}\left(\frac{1}{f_{\max} - f_{\min}}\int_{f_{\min}}^{f_{\max}} 10^{\frac{L_{\mathrm{sc}}(f)}{10}}\mathrm{d}f\right), \tag{4.1}$$

where $L_{\mathrm{sc,m}}$ and $L_{\mathrm{sc}}(f)$ are both in dB scale, and $f_{\min}$, $f_{\max}$ and τ denote the highest and lowest measurement frequencies and delay time, respectively.

In general, the frequency dependence of the scattering loss was found to be flat in the middle of the band, while fluctuation of the scattering loss was large around lowest and highest frqeuency regions. This was attributed to the limited availability of bandwidth in the regions, as confirmed in the anechoic chamber test (see Fig. 3.3 of Chap. 3.3). In cluster E, the notch of the scattering loss appeared in the middle of the bandwidth. This was probably an interference pattern between the path of interests and adjacent path on the angular-delay domain. It seems that the difference of delay time between two paths were closer than the delay resolution, although we used 3 GHz for bandwidth of subband, realizing 10 mm resolution of path length. In cluster C, frequency dependence of the scattering loss was observed, but specific reasons cannot be drawn for this.

In most cases, it seems reasonable to assume that the frequency characteristics are smooth in the middle of the bandwidth, where scattering loss is around the averaged value as listed in Table 4.3. This assumption led to a simple simulating process of generating scattering loss with reasonable accuracy.

4. **Properties of the scattering objects largerly determined the shape and power composition of clusters.**

   As to the comparison of scattering loss among clusters, it was found that cluster E showed the smallest value, while the largest loss was obtained in cluster G. It can be seen that the scattering loss of the display equipped on the wall was small. Among physical phenomena that affected the scattering loss of propagation paths, such as the length of propagation paths, the number of interactions with scattering objects, incident angles to the scattering objects, and properties of the scattering objects, it seemed that the properties of scattering objects, such as the size, material, and surface condition affected the scattering loss most. Possible obsevations supporting the observation are as follows: the strongest propagation path in cluster D experienced interaction with scattering objects twice, and one of the interactions were the specular diffraction due to the metal frame of sliding door. However, the scattering loss was still smaller than clusters F and G, which were composed of paths experienced only single bounce due to ceiling/floor (cluster F), and wall (cluster G). This can lead to the conclusion that the number of interaction with scattering objects were less important. As to the incident angles to the scatterers, it is impossible to draw any conclusion from the results obtained in this measurement since the number of samples were too few.

4.2.4 Results from the Inter-Room Scenario

Propagation modeling results in the inter-room scenario is shown in Fig. 4.6. According to the multi-dimensional clusterization of propagation paths, total 8 clusters were identified. Propagation path distributions on the DOA–delay and DOA–DOD map are shown in Figs. 4.6(a) and 4.6(b), respectively. Identification of the strongest path belonging to each cluster are shown in Fig. 4.6(d). Although there was a wall between the Tx and Rx antennas, obtained clusters still followed the specular reflections so that the path identification was straightforward.

4.2.4.1 Cluster Composition

Clusters A and B arose from one side of the wall, while clusters F and G came from the opposite side of the wall. Clusters A and B, F and G can be distinguished by considering whether they experience a reflection from the window of Tx side or not. It is interesting to point out that although the walls were symmetric with respect to the Tx–Rx line, the number of detected paths and their power levels in clusters A and B were slightly different from those in clusters F and G. Cluster D was associated with the paths around the shortest delay paths, as explained above. Ceiling or floor reflections appeared as cluster E. Cluster C revealed the same DOA and DOD as the shortest delay cluster and ceiling/floor reflection clusters (clusters D and E), but revealed longer delay. This corresponded to the reflection from the back of the Tx, *i.e.,* window reflections. Clusters H was from the back of the Rx, and contained three types of specular paths: a single bounced path from the window at the back of the Rx, and twice reflected paths experiencing wall reflection at the back of the Rx and side walls. Although the propagation mechanisms of the three paths were totally different with each other, they were detected as an identical cluster because of similar values of delay time and angular information. It implies that the propagation paths contained inside clusters do not necessarily experience the same scattering process, particularly when the cluster revealed longer delay time, corresponding to the longer path length. Compared to the reflection from the back of Tx, the number of paths coming from the back of Rx was few because the paths reflecting at the back of the Rx had longer delays, and suffered from greater path loss, resulting in a less possibility to be detected due to the low signal-to-noise ratio.

4.2.4.2 Findings on Cluster Properties

Cluster properties were analyzed for the extracted clusters as summarized in Table 4.4. The followings are the findings from the cluster properties.

1. **Different from the LOS channel, the shortest delayed path formed a cluster.**

   The only difference of propagation characteristics from the LOS channel was that the direct path in the LOS scenario was replaced by a cluster including the shortest delayed path, namely cluster E. Cluster E showed specific characteristics in its spread parameters; it had the largest azimuthal angular spread among clusters, and its value was more than twice as large as the values of other clusters as shown in Table 4.4. This was due to the wall, and more specifically, due to reinforcings inside the wall. It caused diffraction and produced propagation paths around the shortest delay paths. Seen from Tx and Rx antennas, the distribution of effective radiation sources on the wall was as wide as the area covered by the reinforcings, making the azimuthal angular spread much larger. Angular and delay spread of other clusters revealed almost the same values as that obtained from LOS scenario, and was ranging from 0.7 to 6.0 deg and from 0.05 to 1.70 ns, respectively.

2. **Modeled power as propagation paths was less than LOS channel mainly due to the wall separating Tx and Rx.**

   Table 4.4 also shows the power composition of clusters relative to the total received power. Among the detected clusters, the cluster enclosing the shortest delayed paths had the largest contribution to the total received power, 31.1 %. Cluster A accommodated the largest number of propagation paths coming from wall reflection, and carried 11.7 % of the total received power. Cluster G, forming the symmetrical angular position of the cluster A with respect to the Tx–Rx line, had the third largest power composition, 8.4 %.

   It was also found that the modeled power by propagation paths was slightly less than in the LOS scenario. It seemed that the wall separaing Tx and Rx affected this result. The reinforcings inside the wall caused many diffracted paths, but it is basically hard to characterize the diffracted paths completely mainly because of the following two reasons: 1) the wavefront of the diffracted paths follow complicated shapes, which are difficult to be modeled using plane and spherical wavefront models; and 2) the diffracted paths are incident to antenna arrays having shorter interval of the delay time or narrower separation of angles than the inherent resolution of the channel sounder, thus it is almost impossible to resolve all the incoming paths even with the fine resolution of our UWB channel souder.

3. **Wall penetration revealed** 3.6 **dB loss.**

   Figure 4.5 shows the power loss of wall penetration. As the distance between Tx and Rx was identical for the LOS and inter-room measurements, the penetration loss due to the wall can be derived by dividing the frequency spectrum of the shortest delayed path in the inter-room scenario by the spectrum of the direct path in the LOS measurement. The reslt showed that the penetration loss was larger in the higher frequency regions. The mean penetration loss averaged over the frequency band was 3.6 dB.

It must be noted that as the cluster properties of the inter-floor scenario revealed similar characteristics as the inter-room scenario, we do not show details of the result here.

4.2.5 Results from the Room-to-Corridor Scenario

In the room-to-corridor scenario, two realizations were measured. One scenario was with the door closed, while the other wad door opened. Propagation path distribution on the DOA–delay and DOA–DOD maps are shown in Fig. 4.7 so that we can compare the two realizations. In OLOS and NLOS realizations, there were 4 and 6 clusters detected, respectively.

4.2.5.1 Cluster Composition

Comparison of clusters between two realizations showed that there were three clusters shared among OLOS and NLOS path distribution. The clusters appeared at the same angular-delay positions on both maps, and they were specifically clusters A, C, and D. Cluster A was a reflection/diffraction from the wall and sliding doors of the room. Cluster C involved reflection or diffraction more than once, and experienced almost the same scattering process as Cluster D in the LOS scenario (see Fig. 4.3(d)). Cluster D included several propagation paths, but their power was so small that it contained only 1.0 % of the total received power. It seemed that the propagation path constituting the cluster D experienced scattering at the objects inside the strage room, but exact path identification was not accomplished due to the lack of angular information on the Tx side.

Other clusters appeared only in either realization of the measurements. However, interestingly, the clusters in OLOS and NLOS realizations were still inter-related with each other. For example, cluster B and the singular path Z in OLOS realization corresponded to clusters E, F, and G in NLOS realization. The path Z was the shortest delayed path which experienced penetration of the wall separating room and corridor. However, in the NLOS scenario, path Z formed cluster E by associating another path having delay time closer to itself. Clusters B, F, and G were composed of propagation paths coming into the room through the door or walls next to the door. However, cluster B was observed only in OLOS realization, and it was divided into two clusters, F and G in NLOS realizations

4.2.5.2 Findings of Cluster Properties

Properties of clusters were also analyzed in this scenario. Results are summarized in Table 4.5. We could obtain the following findings from the results.

1. **Change of scatterer positions inside the first Fresnel-zone led to different cluster properties.**

   For almost all the clusters, the door was located inside the first Fresnel zone of the propagation paths spanned from Tx to Rx antennas. It was found that changing the position of such scatterers can result in different compositions of propagation paths. Here two kinds of differences resulted: 1) propagation path distribution itself changed, and 2) propagation path distribution and cluster shape was maintained, but their power changed. In the former case, clustering results eventually became different as we can see in clusters B, Z, and E. Here several paths were newly created or shadowed by the movement of scatterers. As an example of the latter case, cluster C in OLOS realization contained three strong paths inside having power of more than -90 dB. However, in NLOS realization, the number of paths above the power was reduced to only one in that cluster. The total power contained in clusters was also influenced by this effect.

The absolute power and power composition relative to the total received power were different by 3 dB and 5 % respectively in cluster C. The same observations also held in cluster A.

2. **The complicated structure of the environment resulted in less number of clusters, larger scattering loss, and less modeled power.**

   Compared to the LOS and inter-room scenarios, the following observations of cluster properties were obtained: 1) clusters experienced longer delay due to the increase of Tx–Rx distance and additional scattering loss, thus the number of detectable clusters having sufficient signal-to-noise ratio were small; 2) scattering loss of clusters were also large due complicated scattering process. The mean scattering loss revealed about 10 dB larger values than that of LOS and inter-room scenarios; and 3) the amount of characterized power by propagation paths was much lower than LOS and inter-room scenarios. Both the OLOS and NLOS realizations of room-to-corridor scenario could characterize only half of the total received power, which was the lowest values among the measured environments. It can be seen that there were huge number of weak propagation paths that were difficult to be modeled as a finite set of propagation paths in this environment.

4.2.6 Results from the Indoor-to-Outdoor Scenario

As explained in the environmental description, we also examined two realizations of propagation channels in the indoor-to-outdoor scenario. One realization used metal shutters to cover sliding doors, and other did not use it. Propagation path distribution on the DOA–delay and DOA–DOD domains are compared for the two realizations as shown in Fig. 4.9.

4.2.6.1 Cluster Composition

In both OLOS and NLOS realizations, the number of extracted clusters was 4. Propagation path identification of the strongest paths belonging to each cluster is shown in Fig. 4.10. It was found that wall penetration and diffraction at the edge of windows and sliding doors were the dominant propagation mechanisms in this scenario. Cluster A consisted of the shortest delayed path which experienced wall penetration. Cluster B was also composed of wall penetrated paths, but additionally experiencing ceiling and floor reflection, thus revealing longer delay than Cluster A. Cluster C contained paths reflected on building surfaces located at the back of Tx outside. Paths Z1 and Z2 were identified as singular paths, and were diffracted paths from the metal frame of the sliding doors. The paths carried 1.2 and 2.0 % of the total received power, respectively. As the sliding doors were located symmetrically with respect to the Tx–Rx line, the DOD and DOA angular properties of the paths were also symmetrical. Clusters D contained scattered paths from the display at the back of Rx antenna located inside the house.

4.2.6.2 Findings on Cluster Properties

Cluster properties in two realizations are summarized in Table 4.6. The results revealed the following findings.

1. **Clusters contained shortest delayed paths carried most of propagating power.**

   The shortest delayed clusters occupied 58.3 and 67.6 % of the total received power in OLOS and NLOS realizations, respecitvely. The values were different by 10 %, but cluster power was exactly the same for two clusters. Therefore, the difference was attributed to the different total received power. The OLOS measurement obtained more power than NLOS scenario due to the existence of more propagation paths than NLOS scenario, as well as the higher noise level. It is worth noting that the transmission power contribution by the strongest clusters were much more dominant than other scenarios. It in turn means that clusters composed of scattered paths had only small contribution to the total received power.

2. **Use of the metal shutters did not affect the number of clusters.**

   Although the metal shutters shadowed some propagation paths including two singular paths Z1 and Z2, it did not result in the reduction of number of clusters in the NLOS scenario. Different from the room-to-corridor measurements, the metal shutters of this measurement was located outside of the first Fresnel zone in most clusters. Consequently, properties of detected clusters revealed almost the identical characteristics irrespective of the use of metal shutters.

3. **Wall penetration loss and diffraction loss at the edge of metal frame were about 5 and 18 dB, respectively.**

   Penetration loss was derived for the shortest delayed paths by using the same method as yielding scattering loss (see Sect. 4.2.3.2). It was found that the frequency characteristics of the penetration loss can be approximated as constant value, as we reported in the results from LOS scenario. The mean penetration loss averaged over whole frequency band was 5.3 dB. This value is slightly larger than the penetration loss derived from the inter-room scenario, 3.6 dB. The difference was probably because of the difference in structures for walls facing outdoor and for walls separating rooms.

   The scattering loss of two singular paths were also derived. These values correspond to the diffraction loss due to the metal frame of sliding doors, and are 19.4 and 17.2 dB for paths Z1 and Z2, respectively.

4.2.7 Findings from the Path Identification Results

According to the results of path identification, it turned out that all strongest paths in the dominant clusters followed specular reflections or specular diffractions. Here specular diffraction refers to the paths which satisfy Keller's law. This implies that the spatial and temporal behaviours of a cluster are no more independent, and relative position between antennas and scatterers, and the size of scatterers determined cluster properties. This findings are in line with the one pointed out by Cramer et al. [22]. In simulating this kind of propagation paths, the deterministic approach such as the ray-tracing technique (e.g., [70]) would be preferrable because it can handle specular phonemona well.

In the next section, we discuss the difference of cluster propeties by taking the propagation environments into accout in detail. Furthermore, stochastic modeling of cluster parameters is done by combining all the parameter sets obtained from the measurements.

4.3 Cluster Properties in Different Scenarios

4.3.1 Definition of Cluster Parameters

In this section, we analyze the following 6 types of cluster parameters. The parameters straightforwardly express the behaviour of clusters, helping us grasp the characteristics of propagation environments intuititively and to compare different environments clearly.

- N_{cluster}: *the number of clusters* in one measurement scenario;

- σ_ϕ, σ_τ: *cluster azimuthal angular and delay spread* within cluster in the DOD/DOA azimuthal and delay domains respectively;

- K_{cluster}: *cluster power ratio* refers to the ratio of power between the strongest cluster and other clusters (in dB scale). In the LOS scenario, the power of the strongest cluster was replaced by that of the strongest path, that is, the direct wave, so K_{cluster} is equivalent to the Rician K-factor [86];

- PCT: *percentage of the extracted power by the propagation paths within* P_{total}; from this value, the total diffuse power can be calculated by Eq. (4.2);

$$P_{\text{diffuse}}\ [\text{dB}] = P_{\text{total}} + 10\log_{10}\left(1 - \frac{PCT}{100}\right) \tag{4.2}$$

- P_{dyn}: *dynamic range of the propagation paths* is the difference of the power between the strongest path and weakest path, or equivalently, between the strongest path and diffuse paths. The smaller this value, the more diffuse the environment is.

4.3.2 Cluster Parameters in Different Scenarios

The cluster parameters derived from each scenario are summarized in Table 4.7. The results provide the following observations:

- N_{cluster}: *The number of clusters* varied from 4 to 9. In the inter-floor measurements, the largest value was observed possibly due to ceiling / floor penetration. Metallic reinforcement inside the walls, ceiling, and floor caused the wide distribution of effective radiation sources over the medium, thus resulting in many diffracted paths. Therefore, the distribution of the paths was wide in the angular domain and much closer to each other, compared to the LOS scenario. In other words, overlapping of clusters were frequently observed in the environment, ending up with cluster boundary uncertainties. Practically, however, the exact cluster boundary is not necessarily important in simulating channels. The indoor-to-outdoor scenario and room-to-corridor measurements with OLOS realization showed the smallest N_{cluster}. In the outdoor-to-indoor scenario, the number of clusters was kept regardless of the use of shutters, although some paths were shadowed when metal shutters were used. The less number of clusters than other scenarios was attributed to the few scatterers around the outdoor Tx antennas. Whereas the number of clusters were different between OLOS and NLOS realizations of room-to-corridor scenario. Altough the propagation path distribution was almost similar for two measurement results, use of the door located inside the first Fresnel-zone of many clusters have the propagation path distribution slightly changed, and it resulted the difference.

- σ_ϕ, σ_τ: *The cluster azimuthal angular and delay spread* revealed almost the same range in all measurement scenarios. In most cases, the deviation was less than 10 deg in the azimuthal domain and 2 ns in the delay domain. The cumulative distribution function (CDF) of the azimuthal and delay deviations are shown in Fig. 4.11. The number of samples used for the CDF was 84 and 42 in the azimuthal and delay domains, respectively. Each curve was fitted by a linear function, resulting in the following formula:

$$
\begin{aligned}
CDF(\sigma_\phi) &= \frac{0.85}{6.50}\sigma_\phi \quad (0 \le \sigma_\phi < 6.50), && (4.3)\\
&= \frac{0.15}{6.50}(\sigma_\phi - 6.50) + 0.85 && (4.4)\\
& (6.50 \le \sigma_\phi \le 13.0), &&\\
CDF(\sigma_\tau) &= \frac{\sigma_\tau}{1.95} \quad (0 \le \sigma_\tau \le 1.95). && (4.5)
\end{aligned}
$$

  The large standard deviation of azimuthal angles represented by Eq. (4.4) was mainly observed in NLOS scenarios. In inter-room and inter-floor measurements, clusters with the shortest delay revealed the largest azimuthal deviation due to the strong effects of diffraction caused by reinforcements inside the walls (see Cluster A of Fig. 4.6(a) for example).

- K_{cluster}: *The cluster power ratio* indicated less than 0 dB in indoor measurements, while indoor-to-outdoor scenarios revealed more than 5 dB. K_{cluster} with a positive sign indicates that the strongest cluster carries most of the propagating power. In indoor scenarios, OLOS and NLOS environments tend to have smaller K_{cluster}, which means the strongest clusters have less contribution to the total received power. As expected, most of the strongest clusters had the shortest delay. However, it did not hold in the results of inter-floor measurement.

- PCT: *The percentage of the extracted power* revealed more than 70 %, if the power of the strongest cluster was dominant, or if the power contribution from scattered paths was large. The former channel is represented by the indoor-to-outdoor environment, whereas the latter corresponds to the LOS and inter-room scenarios. On the other hand, only half of the received power was extracted as propagation paths in some OLOS and NLOS measurements. In such channels, dominant clusters did not exist or power contribution from scattered paths had less impact on the total received power. These channels can be seen as diffuse environments. It is worth mentioning that the NLOS measurements of indoor-to-outdoor scenario revealed about 5% larger values of PCT compared to the OLOS indoor-to-outdoor result. In room-to-corridor scenarios, NLOS measurements revealed a slightly larger value of PCT than OLOS results. This difference is probably due to the smaller number of multipaths existing in NLOS channels, which are effectively detected as propagation paths by the parametric channel estimation algorithm.

- P_{dyn}: *The dynamic range of the propagation paths* was small in the room-to-corridor and inter-floor environments, while the other scenarios revealed larger values. The largest value was observed in the indoor-to-outdoor measurement, while the inter-floor measurement revealed the smallest value. It can be concluded that OLOS and NLOS indoor channels tend to be diffuse environments in many cases. This is the same observation as what we obtained in the consideration of PCT. In particular, the structure of the objects which separate the Tx and Rx directly affects how diffuse the environments are. For instance, the more complicated the reinforcement structure inside walls, or the more the number of walls between Tx and Rx, the more diffuse the environments are.

The observations of the cluster parameters can also be interpreted with respect to the measurement environments as follows:

1. *In LOS scenarios*, power contribution from scattered paths is large due to the effective illumination of the Tx and Rx antennas on the scattering objects, which is represented by *large* PCT, P_{dyn}, *and* K_{cluster} *with the minus sign.*

2. *In many NLOS and OLOS scenarios*, propagation channels are diffuse where a huge number of weak paths aggregate. It results in cluster parameters with *small values of* PCT*,* P_{dyn} *and* K_{cluster}.

3. *In indoor-to-outdoor scenarios*, the strongest cluster carries most of the propagating power from Tx to Rx. It is reflected in the cluster parameters as *large* PCT*,* P_{dyn}*, and* K_{cluster} *with the positive sign.*

4.3.3 Stochastic Modeling of Scattering Loss

After scattering losses were derived for each path, we modeled it by sorting its magnitude in ascending order within each cluster. Path index is given to each path by its order of magnitude. Note that the path indices are almost independent of the relative angles and delay time within clusters.

The results are depicted in Fig. 4.12. From the figure, it can be seen that the scattering loss is proportional to the log-characteristics of its path index. In addition, the logarithmic curve of the scattering losses can clearly be classified into three types of behaviours. Each curve was fitted by log-functions as follows:

$$L_{\mathrm{sc}}(n) = 14.0\log_{10} n + 10.9, \qquad \text{(Type I)} \tag{4.6}$$

$$L_{\mathrm{sc}}(n) = 10.4\log_{10} n + 23.1, \qquad \text{(Type II)} \tag{4.7}$$

$$L_{\mathrm{sc}}(n) = 23.2\log_{10} n + 9.8. \qquad \text{(Type III)} \tag{4.8}$$

In Eqs. (4.6) to (4.8), n denotes the path index and $L_{\mathrm{sc}}(n)$ is in dB scale. The Type I model was obtained from all clusters in the LOS and inter-room measurements, and two clusters from room-to-corridor measurements. Other clusters in the room-to-corridor environment and all the clusters in the inter-floor measurement were classified into the Type II behaviour. Scattering losses from the strongest clusters in the indoor-to-outdoor measurements were exceptionally modeled as Type III because they revealed a marginal characteristic between Type I and Type II. Other clusters in the indoor-to-outdoor measurements were modeled as Type II.

Scattering loss represented by the Type I model shows smaller values than that of the Type II. As a result, the number of paths contained in Type I clusters tends to be larger than that of Type II clusters because of the wider dynamic range of the path power above the noise level. The Type I behaviour mainly represents the LOS propagation scenario and is dominated by single reflection, diffraction, and penetration mechanisms. In contrast, the Type II scenario arises from NLOS environments where propagation paths experience multiple reflection, diffraction, and penetration.

Table 4.1 Specifications of the Experiment.

Bandwidth	3.1 – 10.6 GHz.
Measurement equipment	Vector network analyzer (VNA), XY-positioner, and X-stage (spatial scanners).
Frequency sweeping points	801.
Spatial sampling	Transmitting array: Uniform linear array 4 points with 48-mm spacing. Receiving array: Uniform rectangular array 4 × 4 points in horizontal plane with 48-mm spacing.
Estimated parameters	DOD azimuthal angle, DOA azimuthal and elevation angles, delay time and frequency spectrum.
Antennas	UWB monopole antennas [79].
Polarization	Vertical–Vertical.
Bandwidth of subband	3 GHz.
Calibration	Internal function of VNA (port–port), Back-to-back at 1 m (antenna–antenna).
Signal-to-noise ratio at the receiver	At least 20 dB.

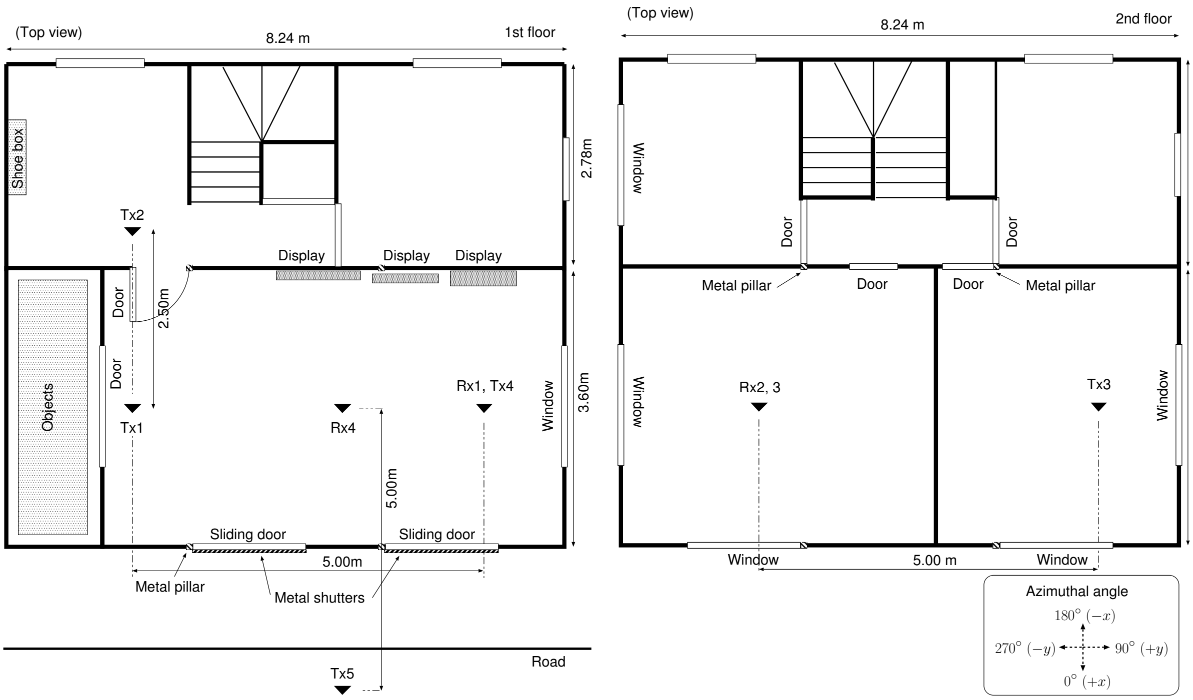

(a) Top view (First floor). (b) Top view (Second floor).

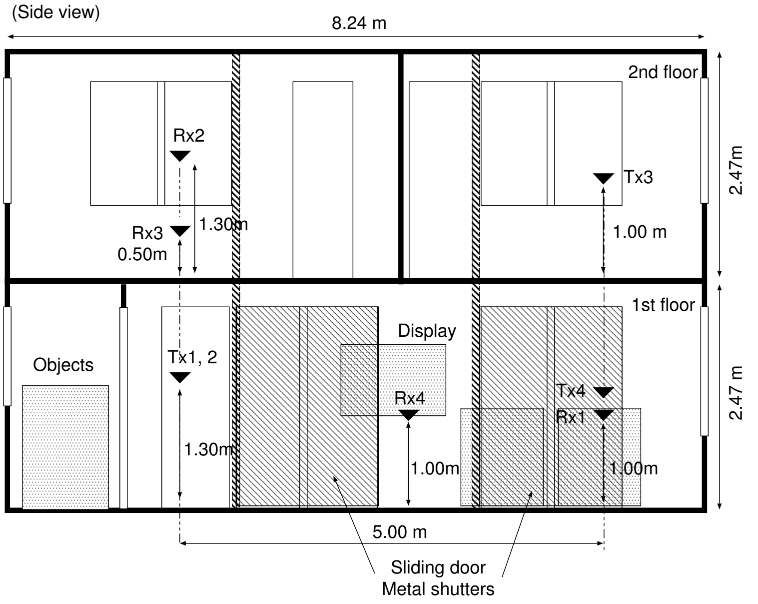

(c) Side view.

Figure 4.1 Floor plan of the measurement site.

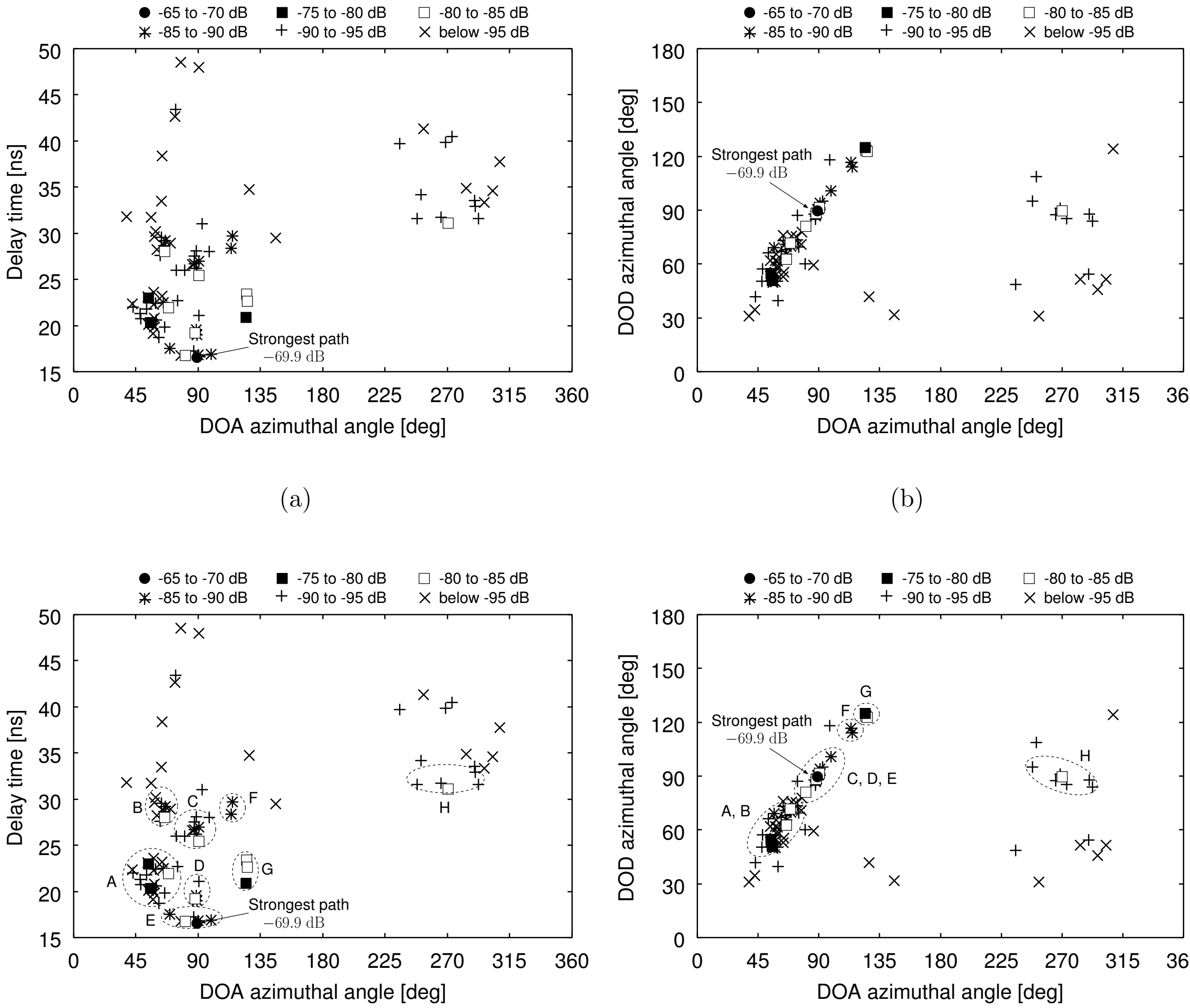

(a)

(b)

(c)

(d)

Figure 4.2 Examples of the multi-dimensional clustering: (a) and (b): Distribution of propagation paths on the DOA–delay and DOA–DOD domains; (c) and (d): clusterization results.

Table 4.2 Median of the root of the CRLB for parameter estimates in each scenario.

Scenario	DOD azimuthal angle [deg]	DOA azimuthal angle [deg]	DOA polar angle [deg]	Delay time [ns]
LOS (Room)	0.5	0.3	1.4	1.6×10^{-3}
OLOS (Room to corridor)	2.0	1.5	4.2	2.6×10^{-3}
NLOS (Room to corridor)	1.4	0.6	2.9	3.0×10^{-3}
NLOS (Inter-room)	0.7	0.6	1.8	1.5×10^{-3}
NLOS (Inter-floor)	2.4	2.2	4.3	7.2×10^{-3}
OLOS (Indoor to outdoor)	3.6	3.0	10.4	1.5×10^{-2}
NLOS (Indoor to outdoor)	2.7	2.9	11.2	1.1×10^{-2}

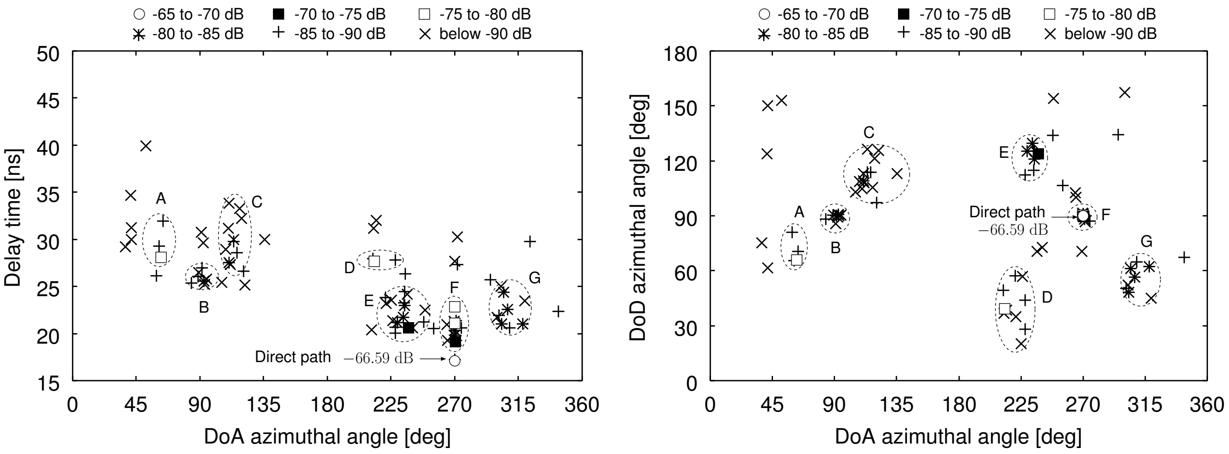

(a) Propagation path distribution on the DOA–delay domain.

(b) Propagation path distribution on the DOA–DOD domain.

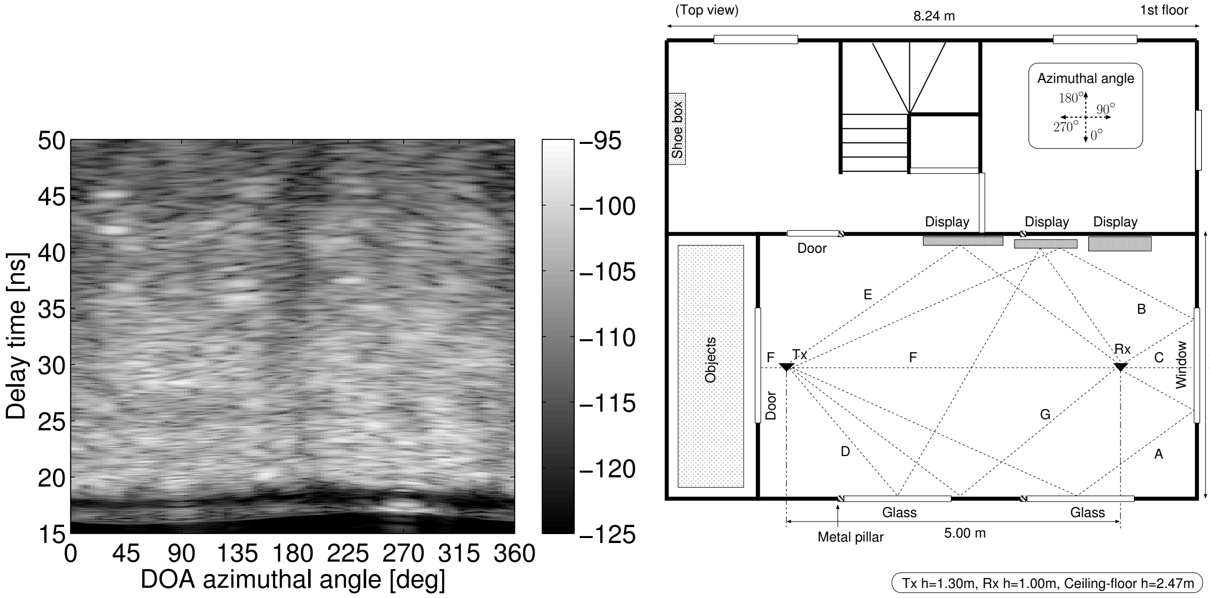

(c) Residual DOA–delay spectrum after the extraction of the propagation paths.

(d) Identification of the strongest paths within each cluster.

Figure 4.3 Measurement results from the LOS scenario.

Table 4.3 Properties of clusters in the LOS scenario: cluster angular and delay spread, power composition, minimum scattering loss, and identification of scatterer.

Cluster (# of paths)	DOA angular spread [deg]	Delay spread [ns]	% of power	Scattering loss [dB]	Identification of scatterer
A (3)	0.7	1.04	1.6	8.2	Sliding door and window
B (7)	3.3	0.46	2.0	10.1	Window and ceiling or floor
C (11)	3.6	1.66	2.5	10.4	Display and window
D (3)	4.8	0.06	2.8	5.9	Edge of the display and metal frame of the sliding door
E (9)	2.9	0.92	15.6	3.2	Display / small desks
F (13)	1.2	1.41	11.5	7.2	Wooden door / ceiling or floor
G (8)	5.7	1.32	4.6	11.1	Wall / glass / metal frame of the sliding door
Direct path	0	0	28.3	N/A	
Other paths	N/A	N/A	3.5	N/A	N/A
Residual	–	–	23.0	N/A	N/A

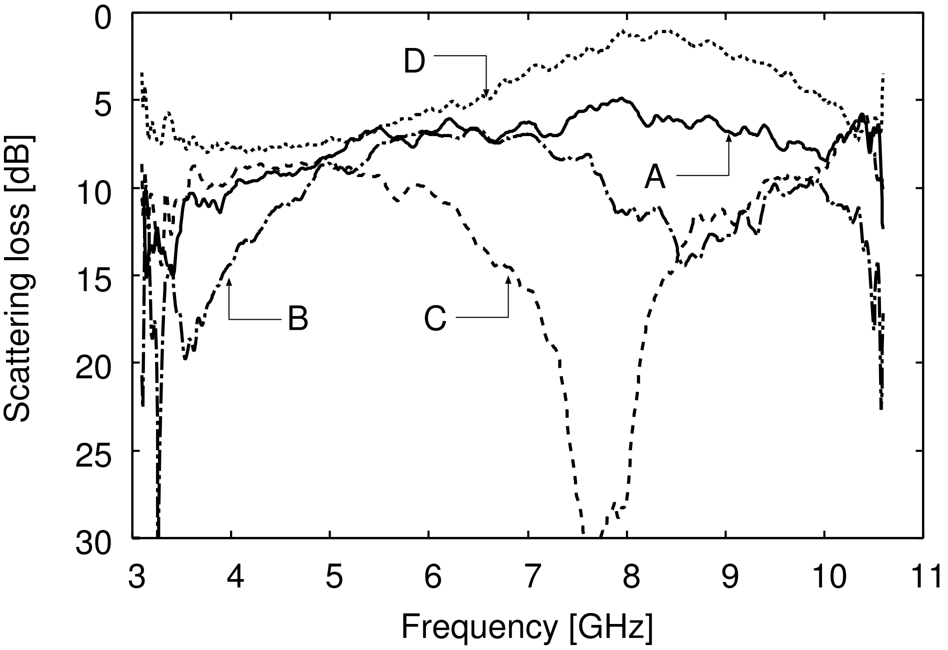

(a) Clusters A to D.

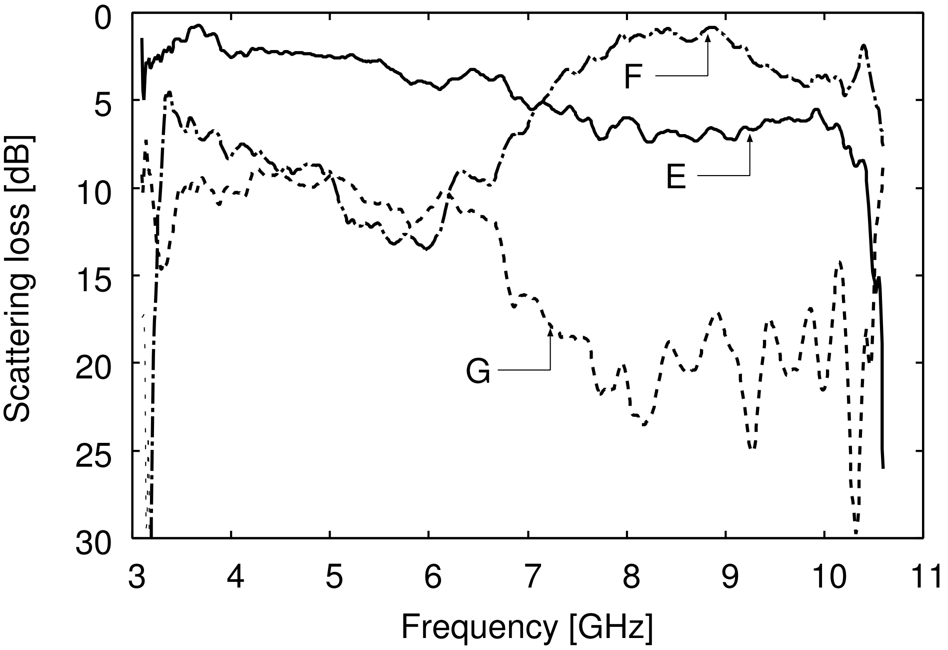

(b) Clusters E to G.

Figure 4.4 Frequency dependent characteristics of scattering loss revealing minimum value within each cluster.

Table 4.4 Properties of clusters in the inter-room scenario: cluster angular and delay spread, power composition, minimum scattering loss, and identification of scatterer.

Cluster (# of paths)	DOA angular spread [deg]	Delay spread [ns]	% of power	Scattering loss [dB]	Identification of scatterer
A (23)	6.0	1.28	11.7	10.5	Wall
B (8)	1.8	0.63	2.4	12.5	Wall and window
C (7)	3.3	0.82	3.7	13.0	Window
D (4)	0.8	0.49	4.9	13.0	Ceiling / floor
E (7)	3.4	0.15	31.1	3.6	Shortest delayed cluster
F (2)	0.3	0.66	1.3	14.5	Metal pillar and window
G (3)	0.4	1.14	8.4	9.0	Wall
H (5)	11.9	0.45	1.6	12.4	Window and wall
Other paths	N/A	N/A	3.4	N/A	N/A
Residual	–	–	28.2	N/A	N/A

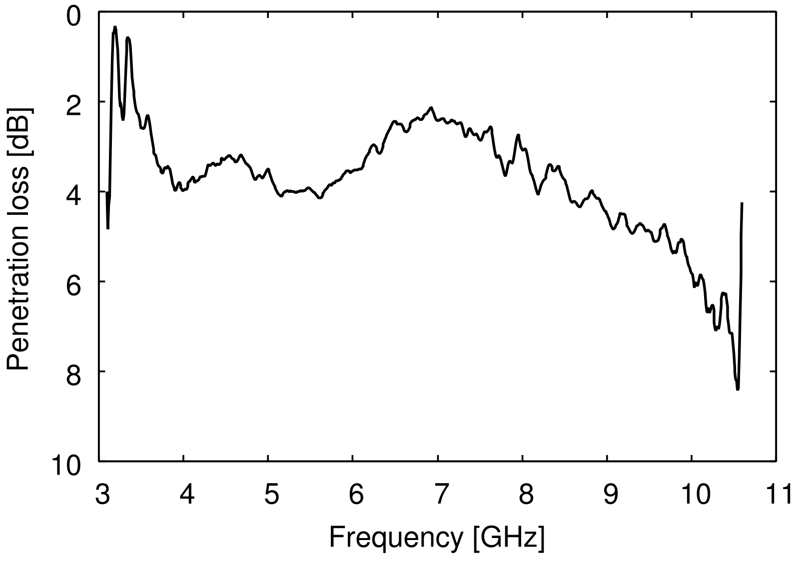

Figure 4.5 Attenuation due to the wall penetration.

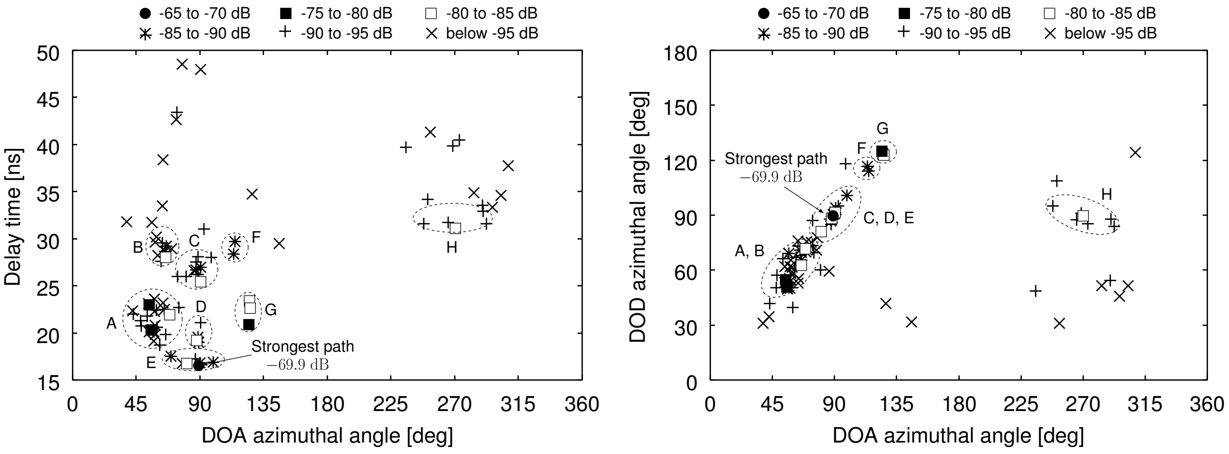

(a) Propagation path distribution on the DOA–delay domain.

(b) Propagation path distribution on the DOA–DOD domain.

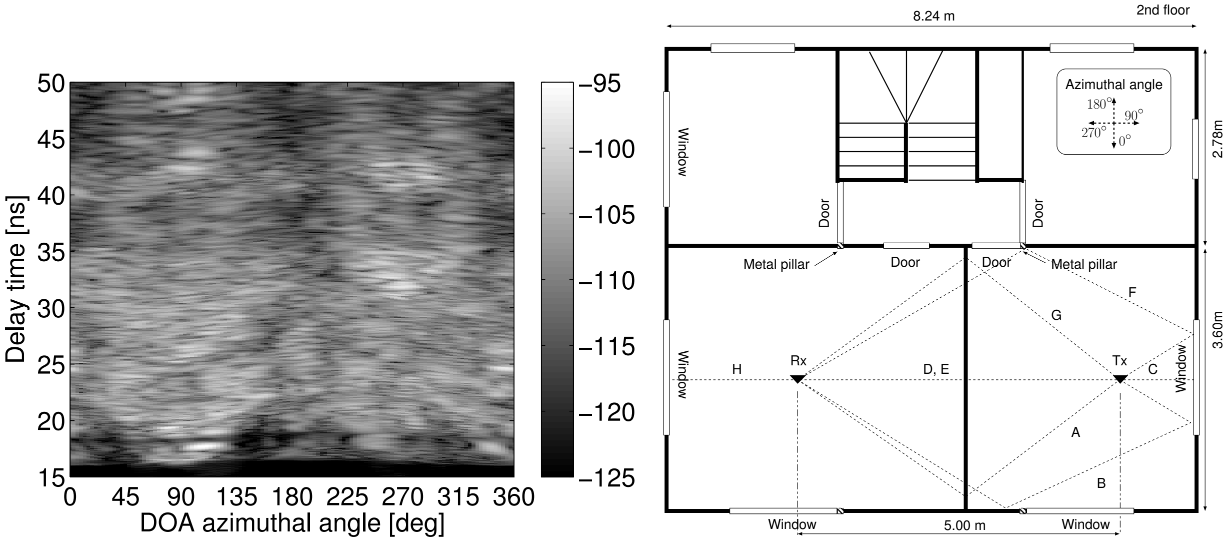

(c) Residual DOA–delay spectrum after the extraction of the propagation paths.

(d) Identification of the strongest paths within each cluster.

Figure 4.6 Measurement results from the inter-room scenario.

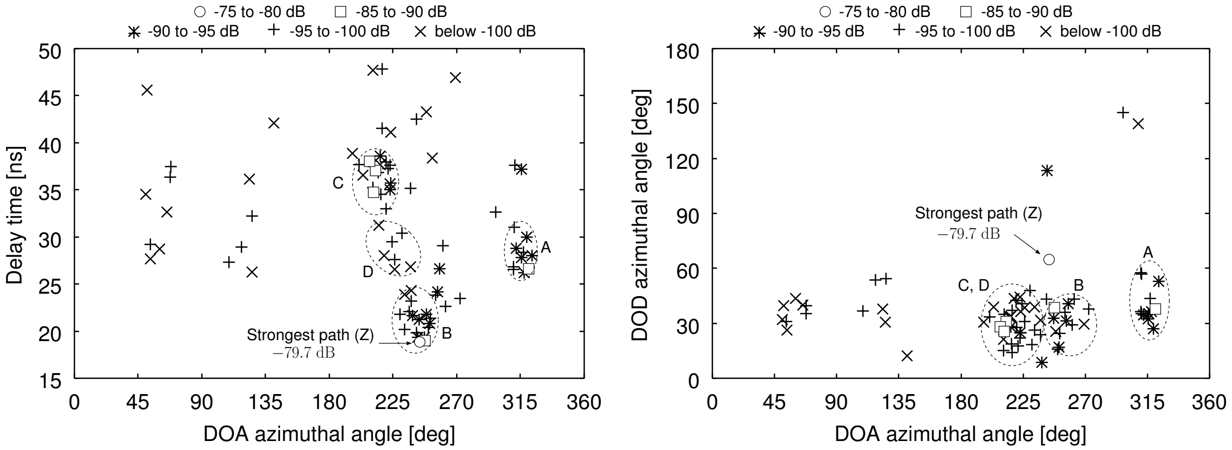

(a) OLOS scenario, DOA–delay domain.

(b) OLOS scenario, DOA–DOD domain.

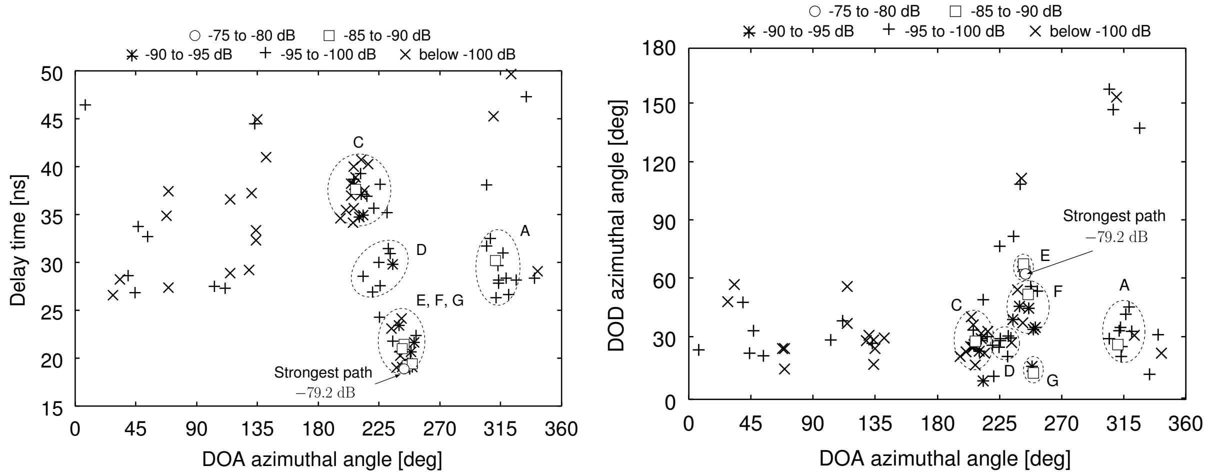

(c) NLOS scenario, DOA–delay domain.

(d) NLOS scenario, DOA–DOD domain.

Figure 4.7 Measurement results from the room-to-corridor measurment.

Table 4.5 Properties of clusters in the room-to-corridor scenario: cluster angular and delay spread, power composition, and minimum scattering loss.

Cluster (# of paths)		DOA angular spread [deg]	Delay spread [ns]	Cluster power [dB]	% of power	Scattering loss [dB]
A	OLOS (9)	3.9	1.33	−79.8	7.3	17.8
	NLOS (9)	3.5	1.65	−82.3	4.5	18.2
B	OLOS (10)	4.9	1.15	−80.3	6.4	18.4
C	OLOS (19)	5.7	1.39	−77.4	12.6	13.5
	NLOS (20)	6.2	1.35	−80.3	7.1	16.3
D	OLOS (7)	5.7	1.47	−88.5	1.0	24.6
	NLOS (5)	4.7	1.79	−88.9	1.0	25.7
E	NLOS (6)	2.0	1.03	−77.2	14.3	11.8
F	NLOS (10)	3.5	1.55	−79.9	7.8	20.4
G	NLOS (2)	0.4	0.50	−83.5	3.4	21.2
Z	OLOS	0	0	−79.7	8.7	12.2
Others	OLOS	–	–	−80.3	10.4	N/A
	NLOS	–	–	−79.5	8.6	N/A
Residual	OLOS	–	–	−71.5	49.0	N/A
	NLOS	–	–	−72.1	47.1	N/A

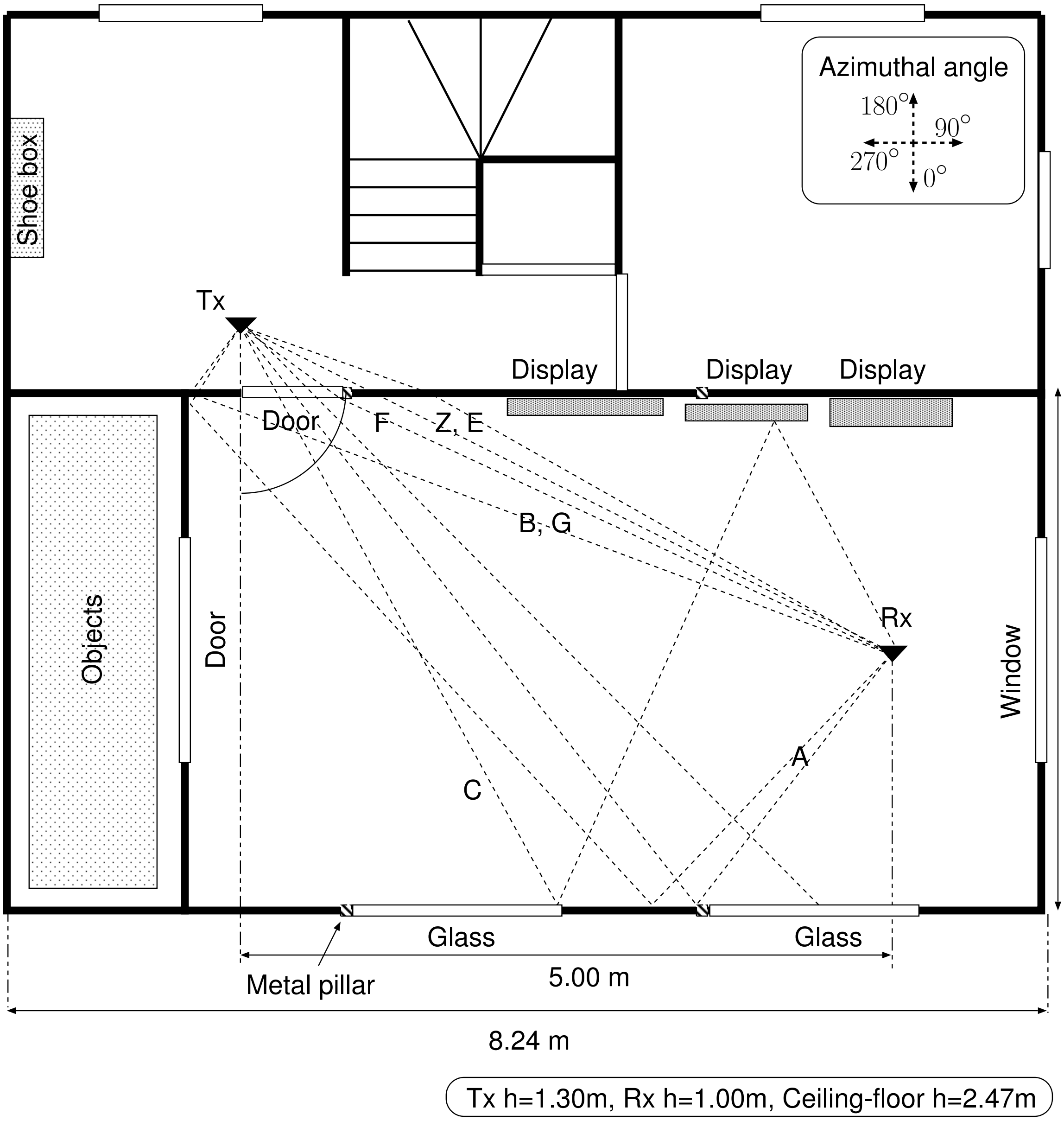

Figure 4.8 Identification of the strongest paths within each cluster for the room-to-corridor scenario.

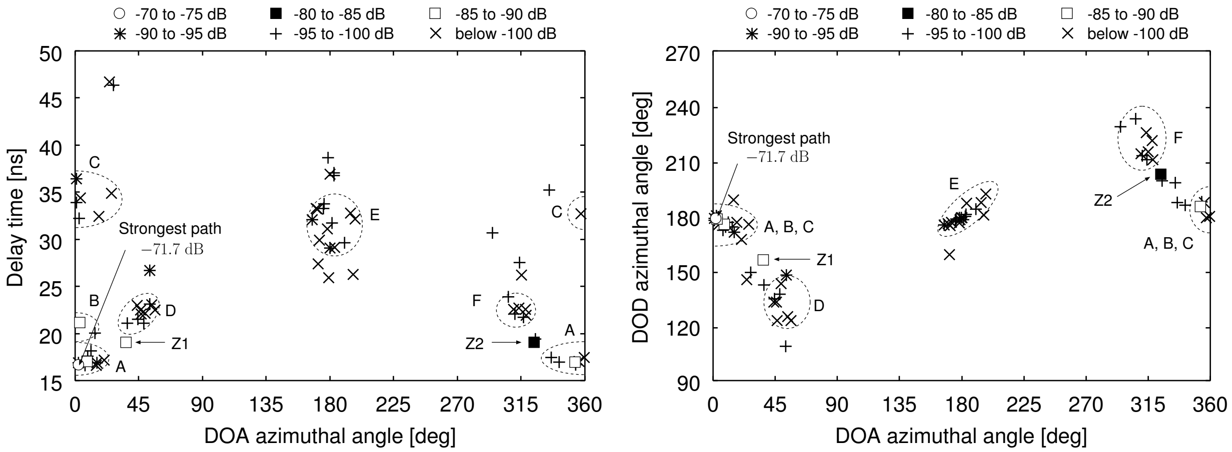

(a) OLOS scenario, DOA–delay domain.

(b) OLOS scenario, DOA–DOD domain.

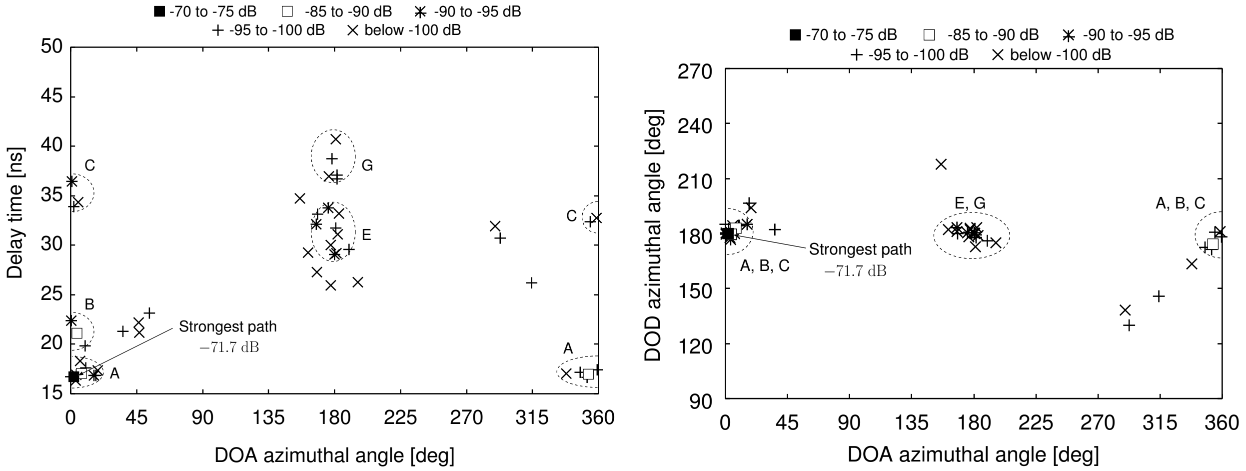

(c) NLOS scenario, DOA–delay domain.

(d) NLOS scenario, DOA–DOD domain.

Figure 4.9 Measurement results from the indoor-to-outdoor measurment.

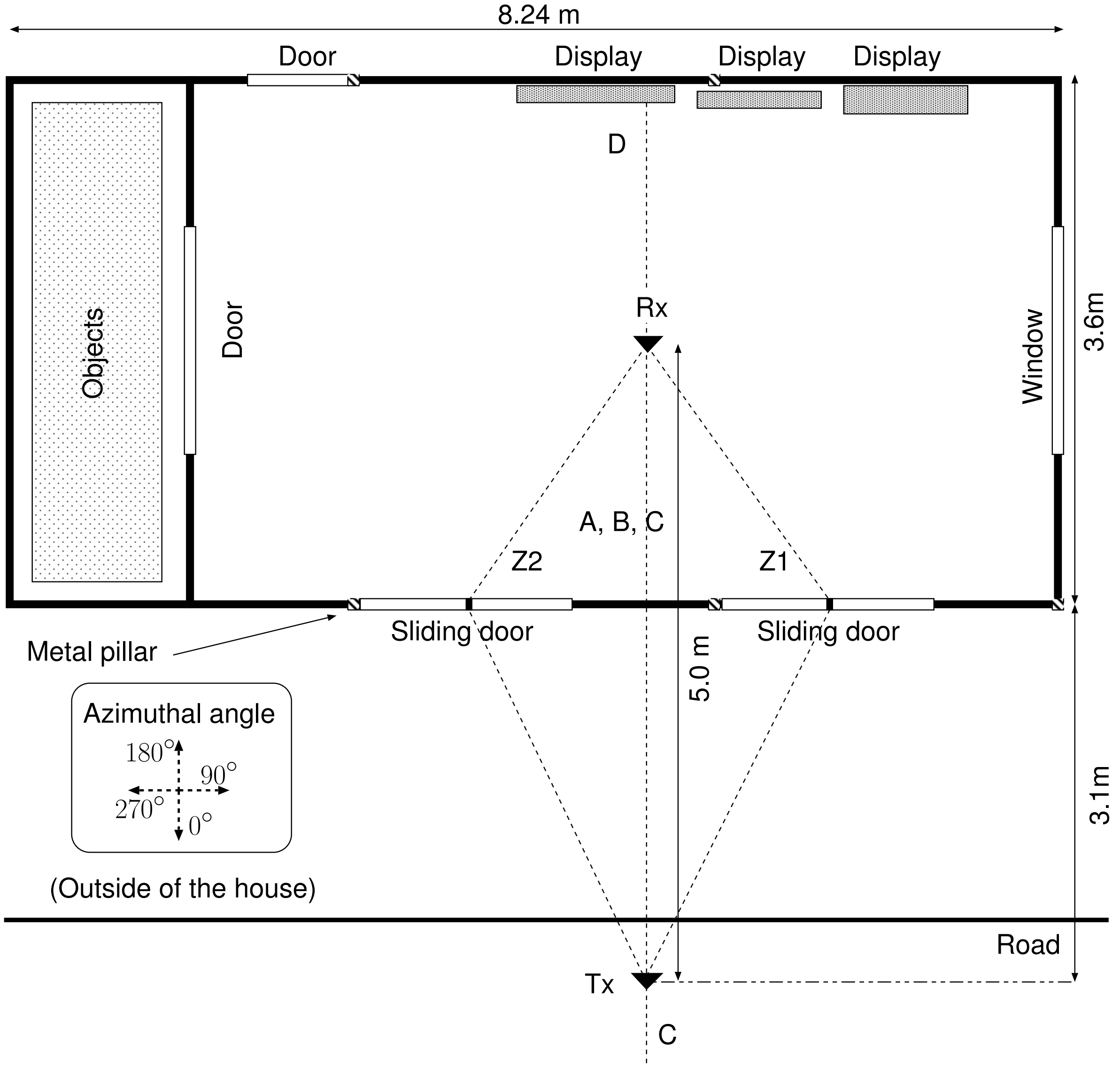

Figure 4.10 Identification of the strongest paths within each cluster for the indoor-to-outdoor scenario.

Table 4.6 Properties of clusters in the indoor-to-outdoor scenario: cluster angular and delay spread, power composition, and minimum scattering loss.

Cluster (# of paths)		DOA angular spread [deg]	Delay spread [ns]	Cluster power [dB]	% of power	Scattering loss [dB]
A	OLOS (14)	2.6	0.11	−69.0	58.3	5.3
	NLOS (18)	2.7	0.11	−69.0	67.6	5.3
B	OLOS (2)	4.0	0.41	−86.4	1.1	20.9
	NLOS (3)	2.5	0.74	−85.1	1.7	20.6
C	OLOS (7)	5.0	1.73	−85.9	1.2	19.7
	NLOS (6)	2.8	1.68	−86.1	1.3	19.4
D	OLOS (13)	7.3	1.83	−81.9	3.0	19.3
	NLOS (11)	6.4	1.85	−82.3	3.2	19.3
Z1	OLOS	0	0	−87.6	1.2	19.4
Z2	OLOS	0	0	−84.7	2.0	17.2
Others	OLOS	–	–	−80.6	4.1	N/A
	NLOS	–	–	−83.7	2.2	N/A
Residual	OLOS	–	–	−72.3	27.7	N/A
	NLOS	–	–	−73.7	22.5	N/A

Table 4.7 Cluster parameters in each scenario.

Scenario	N_{cluster}	σ_ϕ [deg]	σ_τ [ns]	K_{cluster} [dB]	PCT [%]	P_{dyn} [dB]
LOS (Room)	7	$0.8 \sim 6.3$	$0.06 \sim 1.66$	-2.1	77.0	29.2
OLOS (Room to corridor)	4	$3.9 \sim 10.8$	$0.90 \sim 1.47$	-4.8	51.0	24.0
NLOS (Room to corridor)	6	$0.4 \sim 6.6$	$0.50 \sim 1.79$	-4.3	52.9	25.5
NLOS (Inter-room)	8	$0.3 \sim 11.9$	$0.15 \sim 1.28$	-1.2	71.8	30.5
NLOS (Inter-floor)	9	$1.2 \sim 13.1$	$0.28 \sim 1.90$	-5.4	58.8	21.6
OLOS (Indoor to outdoor)	4	$1.7 \sim 7.3$	$0.11 \sim 1.85$	6.4	72.3	31.6
NLOS (Indoor to outdoor)	4	$1.3 \sim 6.4$	$0.11 \sim 1.83$	8.4	77.5	34.0

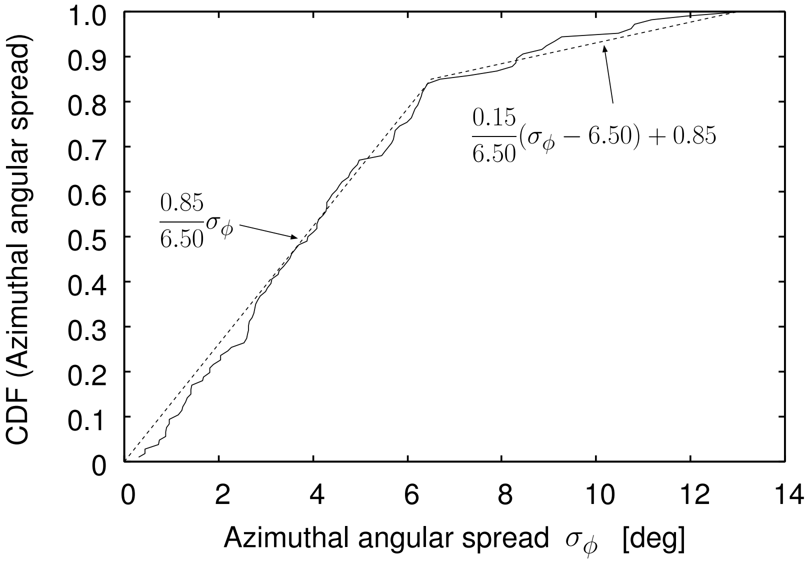

(a) Azimuthal domain.

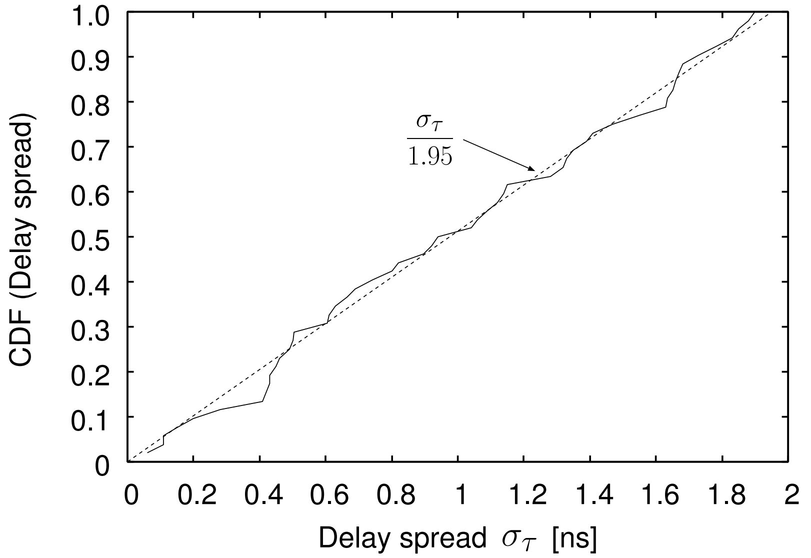

(b) Delay domain.

Figure 4.11 CDF of the standard deviation derived from spatial and temporal path positions within clusters. Fitting of the curve by linear functions is overlayed.

4.3.4 Modeling of the Diffuse Components

In all measurement scenarios, it was generally found from the measurements that some portion of the received power still remains even after sufficient number of propagation paths were subtracted. The existence of "unaccounted power" has also been reported by Win and Scholtz [24] and Molisch et al. [68]. Although the spectrum of diffuse components had no distinct peaks, it had a dynamic range of at least -15 dB above the noise level in every scenario. We found that the power angular-delay profile of the diffuse components showed some correlation with the power distribution of extracted propagation paths. However, if we look at the power delay profile, it turned out that the diffuse components can be modeled with a simple exponential distribution. This observation is consistent with the statement of Thomä et al. [53, 54]. Here we extracted model parameters of diffuse components by fitting with Eq. (4.9).

$$P(\tau) = P_0 \exp\left(-\frac{\tau - \tau_0}{\alpha}\right) \tag{4.9}$$

where τ denotes the delay time, and τ_0 is that of the first arrival path which depends on the Tx–Rx separation distance. P_0 is the peak power of the diffuse components, which is normally observed at delay time $\tau = \tau_0$. α is the decay constant in ns. The derived parameters are shown in Table 4.8. The total received power, P_{total}, is shown as well. The results reveal that P_0 is weak if P_{total} is small. α ranged from 11 to 17 depending on the scenario. It should be noted that these parameters are still affected by the characteristics of measurement antennas because antenna deconvolution was impossible in the power delay profile.

4.4 Summary

This Chapter investigated the multi-dimensional angular-delay characteristics of indoor radio channels in home environments. The environment under consideration covered a variety of scenarios, such as LOS, OLOS, and NLOS scenarios and indoor-to-outdoor channels. First, propagation paths were extracted in each scenario, and then they were classified into clusters using a heuristic multi-dimensional grouping method on the DOA azimuth–DOD azimuth–delay domain. Properties of the clusters were investigated in the following aspects: 1) identification of scattering process, such as reflection, diffraction, and penetration, 2) cluster angular spread, 3) cluster delay spread, 4) scattering coefficient, and 5) power composition. Using the results, comparison of cluster properties for different propagation environment, and stochastic modeling of the cluster properties was performed. The major outcomes corresponding to each investigation items are summarized as follows:

1. *Most of the strongest paths in clusters were specular reflections or specular diffractions.* It simultaneously implied that the spatial and temporal properties of clusters were not independent in one realization of cluster. It is convenient to use deterministic approaches, such as ray-tracing, to generate specific realizations of clusters.

Table 4.8 Parameters of diffuse components in each scenario.

Scenario	P_0 [dB]	α [ns]	P_{total} [dB]
LOS (Room)	−87.3	11.8	−58.8
OLOS (Room to corridor)	−93.2	16.4	−68.4
NLOS (Room to corridor)	−94.0	14.9	−68.8
NLOS (Inter-room)	−89.1	13.3	−62.1
NLOS (Inter-floor)	−98.0	12.2	−73.5
OLOS (Indoor to outdoor)	−93.8	17.2	−66.7
NLOS (Indoor to outdoor)	−95.3	16.1	−67.2

2. *Most of the cluster angular spread were less than* 6.5 *deg.* However, exceptionally, there were a few clusters revealing large cluster angular spread due to many paths penetrating walls, ceiling and floor. It can be seen that whether or not this kind of cluster is observable, depends on the structure inside walls and ceiling/floor. In our measurement scenario, reinforcings inside the wall and wooden floor/ceiling ended up with these clusters.

3. *The largest cluster delay spread was* 1.9 *ns.* As our channel sounding utilized UWB signals, the separation of clusters in the delay domain was much finer than other researches exploiting narrower bandwidth. As a result, the resultant cluster delay spread revealed small values with its median at 1 ns. For example, Chong et al. [30] reported 13.37, 19.09, 37.93 ns of cluster delay spread in LOS, OLOS, and NLOS scenarios respectively. Their measurement campaign utilized 120 MHz bandwidths with the center frequency at 5 GHz.

4. *Two kinds of formula to predict scattering coefficients were derived depending on the types of environment.* It was found that the scattering loss of propagation paths was much larger in most of the OLOS and NLOS channels than in LOS channel. Furthermore, we concluded that the frequency independence of scattering loss can be modeled as constant values. Using the proposed formula and the Friis' transmission formula,

path loss can be easily reconstructed.

5. *Many NLOS and OLOS scenarios revealed more diffused propagation environment than LOS scenario.* The diffuse scenario consisted of a huge number of weak paths having a wide range of angular and delay distributions. In such environments, the number of distinct propagation paths which can be well modeled by our UWB channel sounder was small. Under these environments, it was often the case that there was no cluster having dominant power.

The cluster parameters of LOS scenario was submitted to the IEEE802.15.4a channel modeling subcommittee as a contribution document. Furthemore, the cluster parameters of LOS and inter-room scenarios were approved as representative cluster parameters for home environments within the COST273 MIMO channel model [66]. The list of derived parameters are shown in Appendix I.

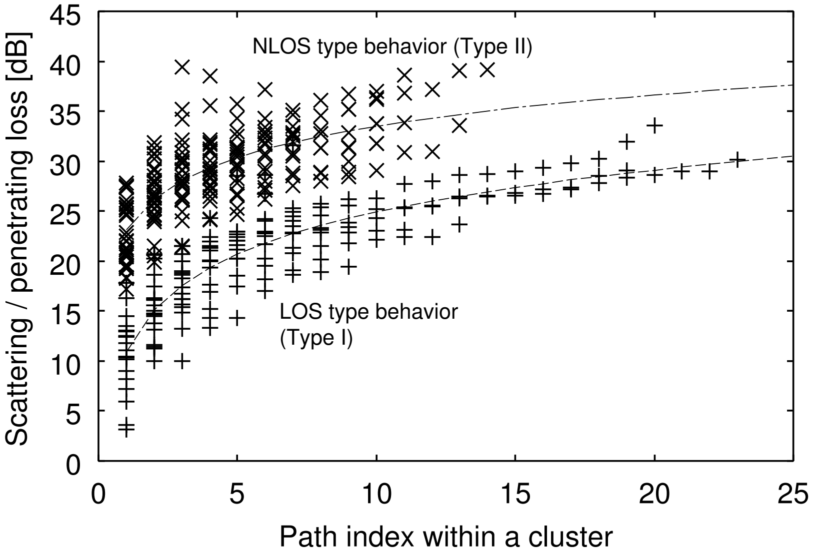

(a) LOS and NLOS type behaviours.

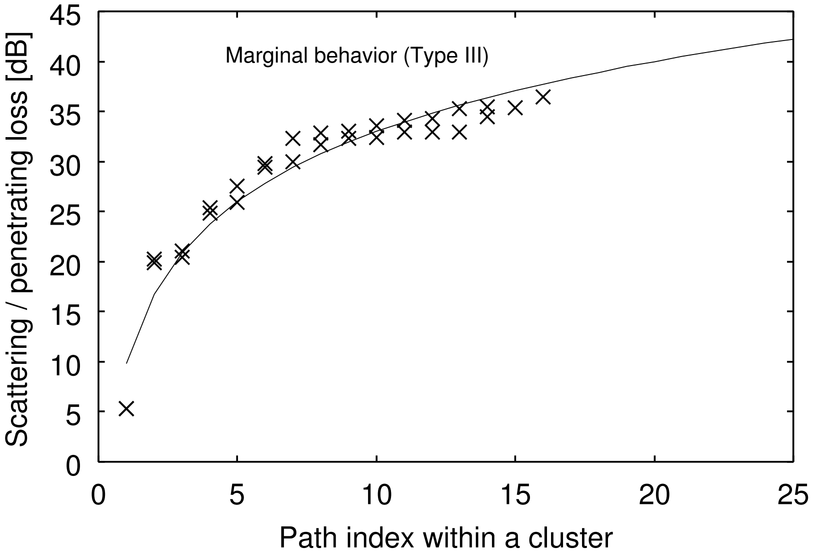

(b) Marginal behaviour between the LOS and NLOS natures. This characteristic is obtained from the strongest clusters in the indoor-to-outdoor measurement.

Figure 4.12 Results from modeling the scattering loss of paths within a cluster. The scattering losses are sorted in ascending order using its magnitude. Path index was given to each path depending on its order of magnitude. The fitted log-functions are overlayed for three types of characteristics.

Chapter5

Verification of UWB Double-Directional Propagation Modeling for Evaluating UWB Transmission Performance

It is essential to confirm the effectiveness of the propagation modeling results conducted in Chapter4 to increase the impact of the outcomes. In this Chapter, we assess the effectiveness of the propagation modeling results in terms of the evaluation of transmission performance in UWB systems. The assessment of the propagation modeling results from the double-directional channel sounding were investigated only for multi-antenna systems [65, 85]. These works reported that the propagation modeling results underestimated the channel capacity. For UWB double-directional spatio-temporal channel sounding and propagation modeling, it is also necessary to assess the applicability of the modeling results. However, there is no literature reporting this. The popular measure for the assessment is bit error probability (BEP) rather than the channel capacity in UWB systems, because UWB signals have a potential to realize high channel capacity due to abundant bandwidth.

Specifically, we investigates the comparison of BEP performances for 1) raw channel transfer function (or equivalently impulse responses) obtained in UWB double-directional spatio-temporal channel sounding, and 2) reconstructed channel transfer functions from the UWB propagation modeling results. Two scenarios were considered for the modeling: line-of-sight (LOS) and non-LOS (NLOS) scenarios. Data transmission simulations using raw channel data are generally called stored channel simulations (*e.g.*, [87, 88]). Simulation results revealed that the propagation modeling results were capable of predicting BEP performances of stored channel simulations accurately. This simultaneously justified the effectiveness of the UWB double-directional spatio-temporal channel sounding and propagation modeling. However, differences between the two characteristics were also observed mainly because of the limitation of propagation modeling. We will show that insufficient modeling of multipath components above a certain power level results in the different BEP performance. Issues related to the limitation and accuracy of the UWB double-directional spatio-temporal channel sounding and propagation modeling will also be discussed.

5.1 UWB Double-Directional Spatio-Temporal Channel Souding and Propagation Modeling

5.1.1 UWB Double-Directional Spatio-Temporal Channel Sounding

The UWB double-directional spatio-temporal channel sounding campaign was conducted in a wooden house. The floor plan of the measurement environment is shown in Fig. 5.1. The room was almost empty except for desks and displays equipped on the wall. Windows and sliding doors of the room were composed of glass and metal frames. Walls were made up of plaster boards, while ceiling and floor consisted of wood. In Fig. 5.1, the position of Tx and Rx antenna is shown. Tx and Rx antennas were mounted 1.30 and 1.00 m respectively above the floor. We measured two scenarios with different Tx positions in order to realize LOS and NLOS channels. Scenario I had a LOS to the Rx, while scenario II was NLOS because the door which separated the room and corridor was shut during the experiment. The Tx–Rx distance on the horizontal plane was 5.00 and 5.59 m in Scenarios I and II, respectively.

With the use of a vector network analyzer, we measured the channel transfer functions. Furthermore, by moving the antenna position at link ends, we obtained the spatial distribution of channel transfer functions. On the Tx side, 4 antenna positions which realized a synthetic linear array were used. The broad side of the Tx linear array was parallel to the x-axis, according to the coordinates defined in Fig. 5.1. The Rx side realized a 4×4 rectangular array on the horizontal plane. In total, $4 \times 4 \times 4 = 64$ spatial realizations of channel transfer functions were obtained. No moving object existed inside the room, so that the channel was kept quasi-static. Other measurement specifications are summarized in Table 5.1.

5.1.2 Propagation Modeling

The spatial transfer function distribution was then applied to a maximum-likelihood (ML) based multi-dimensional propagation parameters estimation algorithm [46]. The ML-based estimates direction-of-departure (DOD), direction-of-arrival (DOA), delay time (DT), and complex gain of propagation paths. The DT refers to the propagating time of each path from Tx to Rx. The algorithm first performs the path detection and then the propagation parameters are estimated as shown in Fig. 2.7(b) (see Chap. 2.4.2). In the parameter estima-

Table 5.1 Specifications of the UWB Double-Directional Spatio-Temporal Channel Sounding and Propagation Modeling.

Bandwidth	3.1 – 5.0 GHz.
Measurement equipment	Vector network analyzer (VNA), Spatial scanners at link ends.
Interelement spacing	48 mm on both sides of the link.
Estimated parameters	DOD azimuthal angle ϕ_{Tx}, DOA azimuthal and polar angles ϕ_{Rx} and θ, delay time τ, and frequency spectrum.
Parametric channel estimation algorithm	ML-based estimator for UWB signal [46].
Antennas	UWB monopole antennas [79].
Polarization	Vertical–Vertical.
Calibration	Internal function of VNA (port–port), Back-to-back at 1 m (antenna–antenna)
Signal-to-noise ratio at the receiving side	At least 20 dB.
Antenna data for deconvolution	Complex gain dependent on polar angles angles and frequency. Polar angles: from 0 to 160 deg, 5 deg step. Frequency: from 3.1 to 5.1 GHz, 0.5 GHz step.

tion, the DT of each path was first identified using the power delay profile (PDP), and then DOD and DOA were estimated with the help of DT. The PDP is defined as the ensemble average of 64 instantaneous channel impulse response (CIR) in an incoherent manner. The parameter estimation was done path by path, and then the array response of the detected path was reconstructed and was removed from the original data. The iteration of path detection, parameter estimation, and update of the original data was continued until there was no distinct path observed in the PDP. The accuracy of the parameter estimates depends mainly on the path detection. In UWB propagation modeling, the path detection using the PDP is especially advantageous because of its fine capability to resolve multipath components in the delay domain.

After the propagation parameters were estimated, directivities of the Tx and Rx antennas were compensated from the complex path gain by using the DOD and DOA information.

Tx and Rx antenna directivities were measured prior to the channel sounding in an anechoic chamber. We assumed that the gain of Tx and Rx antennas was constant on the azimuthal plane, and was dependent only on the polar angles. Thus the radiation pattern was measured only for polar angles. The antenna data samples were 33 in the polar angles and 5 in the frequency, resulting in 165 samples in total for each antenna. As the data samples covered only discrete points of polar and frequency, directivities of other points were calculated using the linear interporation of available samples. Ideally the complex path gain obtained from the antenna deconvolution expresses only propagation characteristics. However, complete antenna deconvolution requires full polarization measurement [27]. We used only the vertical polarization for measurement due to the limitation of the measurement apparatus, thus this would affect the accuracy of antenna deconvolution. Practically, however, the issue is not siginificant for antennas with high cross polarization discremination (XPD), and our monopole antennas [79] are the case. Rather, simplification of antenna patterns in the azimuthal angles might affect the accuracy more.

5.1.3 Propagation Modeling Results

Figure 5.2 shows the PDP derived from the raw channel data and the PDP reconstructed from the modeling results. In the reconstruction, we assumed the same antennas as we used in the measurement at both sides of the link. According to Fig. 5.2, the propagation modeling results did not reconstruct the original PDP properly. The strong multipath components which appeared in the short delayed areas were modeled well, while modeling weaker paths in the long delayed areas was more difficult. This was simply due to the dynamic range of the paths over the noise level. However, it was also found that paths with a high signal-to-noise ratio were not always detectable. For example, looking at the PDP of Scenario I, PDP from the propagation modeling results failed to reconstruct the responses with DT around 26 ns. This was probably because they were hidden by sidelobes of the adjacent peaks with higher power appearing around 23 and 28 ns. The same holds for the PDP obtained in Scenario II with DT around 26, 35, and 40 ns. It can be seen that the insufficient modeling occured at almost the same DT in two scenarios. This was due to the similar shape of PDP, since the Tx antenna positions were just 2.5 m apart between the two scenarios. This resulted in the overlapping of the obsereved propagation phenomena to some extent.

5.1.4 Modeling of the Residual Components

The propagation modeling could extract 75 % of the total received power in Scenario I, while it revealed a lower value in Scenario II, 55 %. The limited capability of power extraction was essentially due to the propagation modeling which was particularly accomplished by the ML-based algorithm in our case. As the algorithm requires an underlying signal model in estimating propagation parameters, such as the wavefront model of impinging waves, the accuracy of the signal model affects the amount of extracted power. According to the indoor propagation modeling results described in Chapter4, the more complicated the environment, the smaller the percentage of modeled power expected. The existence of residual power in parametric channel modeling has been reported by several researchers, such as Molisch et al. [65], Pal et al. [85], Thomä et al. [53], and Win and Scholtz [24].

PDP of the residual components from two scenarios are shown in Fig. 5.3. It can be seen from the figure that the PDP of the residual component is modeled as a concatination of several exponential distributions, which is a common modeling strategy in the delay domain as performed in the conventional Saleh and Valenzuela model [20]. Accordingly, the residual PDP was modeled in similar forms as Eq. (4.9),

$$P_{\mathrm{dif}}(\tau) = \frac{1}{\overline{G}} \sum_{n_{\mathrm{dif}}=1}^{N_{\mathrm{dif}}} P_{n_{\mathrm{dif}}} \exp\left(-\frac{\tau - \tau_{n_{\mathrm{dif}}}}{\alpha_{n_{\mathrm{dif}}}} \right), \tag{5.1}$$

where $\overline{G} = \overline{G}_{\mathrm{Tx}}\overline{G}_{\mathrm{Rx}}$ denotes the product of mean gain in Tx and Rx antennas, respectively. By dividing the PDP by the mean antenna gain, antenna deconvolution is conducted. Strictly speaking, angular information is required for proper antenna deconvolution, but we simplified the procedure by assuming that angular power spectrum follows the uniform distribution and antenna gain is constant over the whole solid angles with the mean antenna gain. With the simplification, we can treat the double-directional power angular-delay spectrum as the multiplication of independent power spectrum density in each domain,

$$P_{\mathrm{dif}}(\phi^{\mathrm{Tx}}, \phi^{\mathrm{Rx}}, \theta, \tau) = P_{\mathrm{dif}}(\phi^{\mathrm{Tx}}) P_{\mathrm{dif}}(\phi^{\mathrm{Rx}}) P_{\mathrm{dif}}(\theta) P_{\mathrm{dif}}(\tau). \tag{5.2}$$

In fact, the double-directional power angular spectrum of the residual components revealed complicated shapes so that modeling of the components requires sophisticated methods. However, it can also be seen that the angular power spectrum density approaches the uniform distribution as the number of data samples gets large, that is, the modeling becomes a stochastic approach.

In each scenario, obtained parameters of the PDP from Eq. (5.1) are shown in Table 5.2. The number of fitted exponential distribution was 3 and 2 in Scenarios I and II, respectively. The number of exponential distributions were determined manually by examining the goodness-of-fit of the modeled PDP with the residual PDP. Minimum-mean square error criterion was applied in determining model parameters. Different from the conventional Saleh and Valenzuela model, the decay exponent α of the first exponential distribution took negative values to represent the shape of PDP before the peak value. Since the region was in between the LOS component and reflected path with largest power, the power level increased with larger delay time. The shape was commonly observed in all the scenarios tested.

Finally, the residual components can be reconstructed by considering diffuse paths, which are generated based on the modeled results as follows:

1. Determine angular and delay properties of each diffuse path.
   Separation of diffuse paths were determined by the resolution of channel sounding and propagation modeling in the domain, *i.e.*,

$$
\begin{aligned}
\phi_{\mathrm{dif},i}^{\mathrm{Tx}} &= i\Xi_{\phi^{\mathrm{Tx}}} && \left(0 \le i \le \left\lfloor \frac{2\pi}{\Xi_{\phi^{\mathrm{Tx}}}} - 1 \right\rfloor\right) && (5.3)\\
\phi_{\mathrm{dif},i}^{\mathrm{Rx}} &= i\Xi_{\phi^{\mathrm{Rx}}} && \left(0 \le i \le \left\lfloor \frac{2\pi}{\Xi_{\phi^{\mathrm{Rx}}}} - 1 \right\rfloor\right) && (5.4)\\
\theta_{\mathrm{dif},i} &= i\Xi_{\theta} && \left(0 \le i \le \left\lfloor \frac{\pi}{\Xi_{\theta}} \right\rfloor\right) && (5.5)\\
\tau_{\mathrm{dif},i} &= \tau_1 + i\Xi_{\tau} && \left(0 \le i \le \left\lfloor \frac{\tau_{\max} - \tau_1}{\Xi_{\tau}} - 1 \right\rfloor\right) && (5.6)
\end{aligned}
$$

   where the operation of $\lfloor x \rfloor$ is the floor function which extracts the integer of the value x, Ξ represents the resolution in one domain, $\tau_{\max}$ is the maximum delay time which the channel sounding could estimate (in the present case, 106 ns), and τ_1 denotes the base delay which normally corresponds to the delay time of the first arrival path. According to Table 2.1, which shows the angular and delay resolution, $\Xi_{\phi^{\mathrm{Tx}}} = \Xi_{\phi^{\mathrm{Rx}}} = 20$ deg, $\Xi_{\theta} = 40$ deg, and $\Xi_{\tau} = 1/1.9$ ns in the present case. The number of diffuse paths in the multi-dimensional angular domain L_{dif} becomes

$$
L_{\mathrm{dif}} = \left(\left\lfloor \frac{2\pi}{\Xi_{\phi^{\mathrm{Tx}}}} - 1 \right\rfloor\right) \left(\left\lfloor \frac{2\pi}{\Xi_{\phi^{\mathrm{Rx}}}} - 1 \right\rfloor\right) \left\lfloor \frac{\pi}{\Xi_{\theta}} \right\rfloor. \tag{5.7}
$$

2. Determine the complex amplitude of each diffuse path.
   Power of each diffuse path is obtained based on the modeled residual components, Eq. (5.1). Assuming that the power spectrum in the angular domains are modeled as a uniform distribution, the power of each path is denoted by

$$
P_{\mathrm{dif}}(\phi_{\mathrm{dif},i}^{\mathrm{Tx}}, \phi_{\mathrm{dif},i}^{\mathrm{Rx}}, \theta_{\mathrm{dif},i}, \tau_{\mathrm{dif},i}) = \frac{P_{\mathrm{dif}}(\tau_{\mathrm{dif},i})}{L_{\mathrm{dif}}}. \tag{5.8}
$$

   In the present case, we assumed that the amplitude and phase of each diffuse path are constant over the considered bandwidths, *i.e.,* $3.1 - 5.0$ GHz, and thus, has the following complex amplitude s_{dif},

$$
s_{\mathrm{dif}}(f, \phi_{\mathrm{dif},i}^{\mathrm{Tx}}, \phi_{\mathrm{dif},i}^{\mathrm{Rx}}, \theta_{\mathrm{dif},i}, \tau_{\mathrm{dif},i}) = \sqrt{\frac{P_{\mathrm{dif}}(\tau_{\mathrm{dif},i})}{L_{\mathrm{dif}}}} \exp(\mathrm{j}\xi), \tag{5.9}
$$

   where ξ is a random phase taking values between 0 and 2π.

Using the information of diffuse paths generated above, transfer function and channel impulse responses can be reconstructed by the same manner as propagation paths, which were extracted by the ML-based estimator.

Table 5.2 Model parameters of the residual PDP.

	Scenario I ($N_{\mathrm{dif}} = 3$)			Scenario II ($N_{\mathrm{dif}} = 2$)		
	$P_{n_{\mathrm{dif}}}$ [dB]	$\alpha_{n_{\mathrm{dif}}}$ [ns]	$\tau_{n_{\mathrm{dif}}}$ [ns]	$P_{n_{\mathrm{dif}}}$ [dB]	$\alpha_{n_{\mathrm{dif}}}$ [ns]	$\tau_{n_{\mathrm{dif}}}$ [ns]
$n_{\mathrm{dif}} = 1$	−79.0	−4.1	16.92	−90.4	−8.0	18.64
$n_{\mathrm{dif}} = 2$	−74.2	8.6	23.16	−83.7	11.3	30.93
$n_{\mathrm{dif}} = 3$	−92.8	12.7	65.10	N/A	N/A	N/A

The transmission simulation described in the next section used three sets of CIRs comprised of 64 spatial realizations each: 1) CIR calculated from the raw data, 2) CIR reconstructed from the propagation modeling results without diffuse paths, and 3) CIR from propagation modeling results with the consideration of diffuse paths. In deriving the CIR, we applied a threshold to eliminate the noise and to investigate effective PDP described in Sect. IV–B. Where the amplitude of the CIR was below the threshold, the value was padded with zeroes.

5.2 UWB Transmission Simulation

In this simulation, we considered 4-ary PPM and bi-phase DS-UWB systems which were actually implemented in a UWB testbed [9, Sect. 2.1]. Both modulations used a root-raised cosine (RRC) pulse as a unit pulse which spanned bandwidth from 3.1 to 5.0 GHz. Duration of the RRC pulse, T_{d}, was set either to 2.4 or 4.8 ns. In DS-UWB, a spread sequence of $[+1\ +1\ +1\ -1\ -1\ +1\ -1]$ was used. Each chip of the spread sequence was represented by the RRC pulse, leading to the frame length of $7T_{\mathrm{d}}$. Information was mapped on the polarity of the spread sequences. Differential encoding was used to map information bits to waveforms. It enabled us to combat the inversion of waveform polarity due to propagation channels, which degrades the BEP performance. In Fig. 5.4, the frame format of data and training sequences are shown. The data frame of PPM contained guard time, and each symbol was sent twice. Thus the frame length of the PPM was $16T_{\mathrm{d}}$. In both modulations, the training sequence consisted of 1334 frames, and was sent before sending the data stream so that the receiver was synchronized with the transmitter. In PPM, the position of the guard time in the training sequence was different from that in the data sequence, and only “00” was transmitted. In the DS-UWB system, the training sequence consisted only of the symbol “0”. To simplify the simulation conditions, channel coding was not taken into account.

The transmitted waveform was convolved with the CIR derived either from the raw data or the propagation modeling results, and then inputted to the Rx side. In the receiver, a correlation receiver was implemented. After the received signal was quantized by the A/D converter, the receiver demodulated the signal into symbols by correlating the received signal with a reference waveform, and finding a maximum output. The reference waveform was the same as the transmitted waveform correspoding to each symbol.

The simulation flow is depicted in Fig. 5.5. The flow emulates the architecture of the UWB testbed. We assumed that the RRC pulse was transmitted from the RF frontend defined at point "A" of Fig. 5.5. This compensated for characteristics of power amplifier and RF filter in the transmitter. On the receiving side, we multiplied the receiving waveform from the Rx antenna by the transfer function of an RF filter and a low-noise amplifier (part "B" in Fig. 5.5) which was actually measured from the UWB testbed. We also measured the noise level of the Digital Sampling Oscilloscope equipped in the receiver of the UWB testbed, and used it in our transmission simulations.

5.3 Simulation Results

Here we define two BEP for the evaluation: 1) 64 BEP obtained from 64 spatial realizations in one scenario which we will call "local BEP", and 2) averaged BEP over the local BEP which will be referred to as "average BEP". This section highlights the results of the transmission simulation and subsequent discussions based on the aforementioned two types of BEP. We first start from a comparison of BEP results from stored channel simulations and that from propagation modeling results without considering the diffuse paths, in order to observe the effect of the residual components in the data transmission simulation.

5.3.1 Average BEP

Figures 5.6 and 5.7 show the average BEP characteristics dependent on energy per bit, E_b/N_0, for Scenarios I and II, respectively. In each figure, two sets of curves corresponding to $T_\mathrm{d} = 2.4$ and 4.8 ns are shown. The threshold level of the CIR was set to -100 dB in both scenarios. For comparison, the BEP curve assuming additive white gaussian noise (AWGN) channel is overlayed.

Every figure shows that the average BEP is decreasing with the increase of E_b/N_0 when $T_\mathrm{d} = 4.8$ ns. In contrast, when $T_\mathrm{d} = 2.4$ ns, the average BEP curve revealed a floor effect in the higher E_b/N_0 areas. This was due to the intersymbol interference (ISI) which tended to be more severe when the symbol length was short. The only exception was that the PPM results from the stored channel simulations in Scenario II revealed floor effect even when $T_\mathrm{d} = 4.8$ ns.

When comparing the average BEP characteristics from the stored channel simulations and those from propagation modeling results, the following observations were obtained:

1. In Scenario I, $T_\mathrm{d} = 4.8$ ns, the average BEP from propagation modeling results was always less than that of the stored channel simulations. The difference in the slope of two curves was attributed to the limited capability of the propagation modeling to

extract the received power. As we discussed in Section II using the PDP, the propagation modeling successfully characterized the LOS components, while other multipath components were not properly modeled. This caused the difference of fading statistics between raw and reconstructed channels, and the average BEP from propagation modeling results approached the characteristics of the AWGN channel where no multipath component existed. The same held in DS-UWB result from Scenario II, $T_\mathrm{d} = 4.8$ ns case.

2. In PPM results in Scenario II with $T_\mathrm{d} = 4.8$ ns, the average BEP curve from the stored channel simulations showed the floor effect in high E_b/N_0, while the effect was not found in the average BEP from propagation modeling results. The difference was also due to the limited performances of the propagation modeling. It was found that only 3 out of 64 local BEP revealed the floor effect in the stored channel simulations, while all the local BEP from propagation modeling results decreased to 0. As a result, the three "nonzero" local BEP caused the difference. The same observation held for the DS-UWB in Scenario I, $T_\mathrm{d} = 2.4$ ns.
3. Other than the differences mentioned in 1) and 2), the average BEP from propagation modeling results was close to that from stored channel simulations. Particularly, the error floor occured in the high E_b/N_0 areas was accurately determined regardless of modulation schemes in most cases. In DS-UWB results from Scenario II, $T_\mathrm{d} = 4.8$ ns, two curves revealed irregular characteristics where they crossed with one another around $E_\mathrm{b}/N_0 = 12$ dB. This was due to the fluctuating slope of BEP curves, which was observed particularly when the number of channel realizations was limited as our simulations.

To summarize, predicting the average BEP performances was accurately performed using propagation modeling results when ISI oriented errors were dominant, or when the transmission data rate was sufficiently low that the system did not suffer from ISI. In contrast, differences resulted in two curves when some of the local BEP were subjected to ISI, while the others were ISI free. This is obviously due to the absence of the diffuse paths in the transmission simulation.

The limited capability of the propagation modeling in extracting power, *i.e.,* 75 and 55 % of the modeled received power in Scenarios I and II respectively, affected only to the slight decrease of E_b/N_0 compared to the stored channel simulations. The difference of E_b/N_0 is summarized in Table 5.3. The loss of E_b/N_0 was less than 0.8 dB, which means that the propagation modeling characterized most of the multipath components that contributed to the energy capture of the receiver.

When comparing the results from two scenarios, Scenario II (NLOS) revealed worse average BEP performances than in Scenario I (LOS), which was the expected results due to the absence of LOS component. It resulted in a less steep slope of the average BEP curve when the system was ISI free, and a higher error floor when ISI occured.

Table 5.3 Degradation of receiving E_b/N_0 in the transmission simulation using propagation modeling results. Diffuse paths were not taken into account.

Modulation format	PPM		DS-UWB	
T_d [ns]	4.8	2.4	4.8	2.4
Scenario I [dB]	0.2	0.1	0.3	0.3
Scenario II [dB]	0.5	0.6	0.6	0.8

Figure 5.8 illustrates the dependence of error floor on the pulse duration for a specific scenarios. Regardless of modulation schemes, it is generally shown that the narrower pulse duration gives rise to the higher error floor (*e.g.,* [65]). However, if we look at an error floor at a specific pulse duration in Fig. 5.8, the next wider/narrower pulse duration does not always lead to the lower/higher error floor. An extreme case is that even if error floor falls to zero at one pulse duration, the wider pulse duration gave nonzero error floor. The observations hold irrespective of the type of channels. This is due to the fact that our transmission simulation used deterministic channels, the shape of PDP affected the results. In contrast, the theoretical consideration used many realization of channels, or a simple shape of PDP such as exponential distribution, revealed a monotonical increase of error floor with narrower pulse duration [65]. It can be concluded that the error floor is sensitive to the shape of PDP.

The next two subsections give further analyses and observation on the difference and agreement between the average BEP characteristics from the stored channel simulations and propagation modeling results.

5.3.1.1 Interference Quotient

The interference quotient [65] is defined as a power ratio between the intergrated power of PDP over a certain window, T, and the power that is not counted in the integration. Mathematical notation is as follows:

$$Q(T) = 10\log_{10}\left(\frac{P_\mathrm{max}}{P_0 - P_\mathrm{max}}\right) \text{ [dB]} \tag{5.10}$$

where P_0 is the total received power, and P_max is defined as

$$P_\mathrm{max} = \max_t\left(\int_t^{t+T} P(\tau)f(\tau)\mathrm{d}\tau\right), \tag{5.11}$$

$P(\tau)$ is a PDP and $f(\tau)$ is a weighting function explained later. When T is the symbol length, the interference quotient can be seen as a measure to express the power contributing to the symbol detection relative to the power affecting to the ISI. The larger the interference quotient, the less likely that ISI occurs. The weighting function reflects the frame format of the transmitted signal as follows.

$$\begin{aligned} f_{\mathrm{PPM}}(\tau) &= \begin{cases} 1 & (4T_{\mathrm{d}} \leq \tau < 12T_{\mathrm{d}}) \\ 0 & (0 \leq \tau < 4T_{\mathrm{d}},\ 12T_{\mathrm{d}} \leq \tau < 16T_{\mathrm{d}}) \end{cases} \\ f_{\mathrm{DS}}(\tau) &= 1 \quad (0 \leq \tau \leq 7T_{\mathrm{d}}) \end{aligned}$$

Zeroes are inserted in $f_{\mathrm{PPM}}(\tau)$ because the transmitted PPM signal has a guard time as shown in Fig. 5.4.

The results are summarized in Tables 5.4 and 5.5 for Scenarios I and II, respectively. The results revealed that larger interference quotients were always observed in the reconstructed channel models. This implies that the PDP which may influence the ISI was less modeled compared to the PDP contributing to the desired signal.

Table 5.4 The interference quotient of the PDP derived from raw data (original PDP) and channel modeling results (reconstructed PDP) for Scenario I.

Modulation format	PPM		DS-UWB	
T_{d} [ns]	4.8	2.4	4.8	2.4
Original PDP	12.2	5.4	17.4	10.5
Reconstructed PDP	16.8	8.0	22.4	15.3

Table 5.5 The interference quotient of the PDP derived from raw data (original PDP) and channel modeling results (reconstructed PDP) for Scenario II.

Modulation format	PPM		DS-UWB	
T_{d} [ns]	4.8	2.4	4.8	2.4
Original PDP	4.7	8.0	11.1	2.7
Reconstructed PDP	5.8	3.6	17.0	4.4

5.3.1.2 Effective PDP

To relate the properties of PDP and the transmission performance, we here introduce a notion of effective PDP, which is defined as a part of the PDP that determines the average BEP performance. We can see that insufficient modeling of the effective PDP resulted in the difference of BEP characteristics. The effective PDP was identified by deriving average BEP with several levels of threshold applied to CIR from the raw data. The threshold level was -100 dB in the previous subsection, and we name it "original curve" as a baseline for the comparison. In this analysis, the threshold was set from -95 to -70 dB with 5 dB step.

Figure 5.9 shows the results of the average BEP characteristics with different threshold levels for PPM and DS-UWB systems in Scenario I. We showed the average BEP curves only for several threshold levels to keep the figure clear. From the results, it was found that the shape of the original curve maintained until a certain threshold level. However, the shape became different above that level, which means that the PDP below that level affected the average BEP performance. We see that the original curve changed when the average BEP was more than twice, or less than half of the original curve at any E_b/N_0. From Fig. 5.9, it can be seen that higher threshold level generally gave rise to lower average BEP. However, the average BEP exceptionally increased with a higher threshold in PPM, $T_\mathrm{d} = 2.4$ ns case. This stemmed from the specific shape of the PDP and the signal format of PPM. Nevertheless, the highest threshold level which maintained the original curve identified the area of effective PDP. For example, looking at Fig. 5.9(a), the original curve maintained a threshold level of -90 dB in $T_\mathrm{d} = 4.8$ ns, while the shape deviated from the original curve when the threshold was -85 dB. Thus we can conclude that the effective PDP was above -90 dB. Relating the effective PDP with the average BEP, which are shown in Fig. 5.6(a), the average BEP from propagation modeling results deviated from the original curve due to the imperfect modeling of effective PDP which lay above -90 dB. Accuracy of PDP modeling below -90 dB actually did not matter for the difference of two BEP curves. The reconstructed PDP from propagation modeling results (see Fig. 5.2(a)) shows that effective PDP with the DT around 26, 33, and 50 ns, and the peak which appeared at 68 ns were insufficiently modeled though they were above -90 dB, and this was the major reason for the difference of the average BEP characteristics. The threshold level is summarized in Table 5.6. Results from Scenario II are also shown. It was found that the effective PDP differed depending on the modulation formats and the symbol length. Applying the results to the PDP depicted in Fig. 5.2, we can see in Scenario I that the insufficient modeling of PDP around 26 and 33 ns mostly affected the differences of the average BEP performance, while insufficient modeling of PDP around 26, 35, and 40 ns had an impact in Scenario II. The effective PDP of Scenario II for DS-UWB system was above -80 and -95 dB in $T_\mathrm{d} = 2.4$ and 4.8 ns, respectively. In $T_\mathrm{d} = 2.4$ ns case, the effective PDP were properly modeled according to Fig. 5.2(b) so that the resultant BEP from propagation modeling results was almost identical to the stored channel simulations (see Fig. 5.7(b)). In contrast, when $T_\mathrm{d} = 4.8$ ns, the effective PDP was insufficiently modeled. As the transmission was free from ISI, the insufficient modeling appeared in the steeper slope of the BEP curve compared to the stored channel simulations.

In this way, the effective PDP provides essential understanding on the relationship between channel properties and transmission performance. Note that the threshold level which determines the effective PDP is the most appropriate value for the threshold in deriving delay spread [65].

Table 5.6 Threshold Values for the Effective PDP.

Modulation format	PPM		DS-UWB	
T_d [ns]	4.8	2.4	4.8	2.4
Scenario I: Threshold [dB]	−90	−75	−90	−85
Scenario II: Threshold [dB]	−85	−90	−95	−80

5.3.2 Local BEP

Finally, we discuss the accuracy of local BEP derived from the propagation modeling results. Figure 5.10 shows the scattered plot of the local BEP derived from the stored channel simulations and propagation modeling results. The results are from Scenario I, and their mean E_b/N_0 of the stored channel simulations was 2.4 dB in PPM and 5.3 dB in DS-UWB, where the average BEP was almost identical for two simulations. In the figure, there are 64 scattered points each derived from spatial realizations, which are ideally identical with each other, thus on the 100% line. In contrast to the agreement of average BEP, we can see from the figure that the local BEP from propagation modeling results did not always accurately determine the result of stored channel simulations. More than 70 % of the local BEP from propagation modeling results was within ±50 % deviation of the local BEP from stored channel simulations, but a few local BEP from propagation modeling results deviated by more than 200 or 50 % of the local BEP from stored channel simulations. The deviation stemmed from the insufficient accuracy of the propagation modeling in characterizing the envelope and phase of the CIR. As the propagation modeling was performed using multi-dimensional power angular-delay profile, which was a coherent summation of 64 CIR, the accuracy of CIR reconstructed by propagation modeling results was not tolerable as that of the power angular-delay profile. We found that the deviation in two types of local BEP was much larger in Scenario II, where less received power was modeled than in Scenario I. It was also found that the deviation was more significant in high E_b/N_0 areas, where BEP was more sensitive to the shape of CIR.

It is also worth noting that the local BEP performances varied drastically when antenna positions were half the wavelength apart from the original position. It was often observed that the change of antenna position resulted in 10 times larger or smaller local BEP than the original local BEP. We can see that the local BEP is sensitive to the small scale fading.

5.3.3 BEP Results with the Diffuse Paths

It was found that the transmission simulation without considering the diffuse paths often resulted in insufficient agreement with the stored channel simulations. Next we present BEP results when diffuse paths were taken into account in the transmission simulation. Figures 5.11 and 5.12 illustrates the average BEP characteristics obtained in two scenarios. It can be clearly seen that the agreement of the modeled channels with the stored channel simulations improved by including diffuse paths irrespective of modulation format, environment under consideration, and symbol rates. Since the diffuse paths supplemented the reflected paths which was not modeled as propagation paths, the BEP results improved the agreement with the stored channel simulations as follows: 1) when BEP is ISI free, the slope of the BEP curve was less steeper, and 2) when BEP suffered from the error floor due to ISI, the error floor levels increased. Furthemore, agreement of E_b/N_0 also improved as shown in Table 5.7. The maximum degradation of E_b/N_0 was 0.3 dB, which was obviously less than when diffuse paths were not taken into account. It must be noted, however, that the agreement of the local BEP did not improve even with diffuse paths. This is again attributed to the fact that the modeling of residual components was performed using PDP and power angular profile as we did for the propagation paths. Reconstructed CIR from the modeling results was still not accurate enough to obtain CIR from raw data.

Table 5.7 Degradation of receiving E_b/N_0 in the transmission simulation using propagation modeling results with diffuse paths.

Modulation format	PPM		DS-UWB	
T_d [ns]	4.8	2.4	4.8	2.4
Scenario I [dB]	0.1	0.1	0.0	0.0
Scenario II [dB]	0.1	0.3	0.2	0.1

5.4 Summary

This Chapter investigated the applicability of UWB propagation modeling results for evaluating BEP performance. We considered two specific modeling examples: LOS and NLOS channels. The major findings are summarized as follows:

1. *This Chapter identified the items that affected the accuracy of the UWB double-directional spatio-temporal channel sounding and propagation modeling.* The items consisted of two folds: the antenna deconvolution and the model-based propagation parameter estimation algorithm. In our case, the former item was related to the insufficient treatment

of the polarization, and the latter issue resulted in the limited percentage of power extraction.

2. Next this Chapter *demonstrated that the BEP simulations taking into account only propagation paths were not always able to predict the average BEP performances* as accurately as stored channel simulations mainly due to the limitations discussed in 1). The antenna deconvolution issue had little effect in our BEP analysis because a) we used antennas with high XPD in the UWB double-directional spatio-temporal channel sounding, and b) we assumed the same antennas as measurements in reconstructing CIR from propagation modeling results. Rather, the limited capability to extract multipaths influenced the insufficient agreement more. Particularly, the effect appeared in the steeper slope of the average BEP curve when ISI free. While inaccurate prediction of error floor levels resulted when some of the local BEP suffered from ISI while the rest was ISI free. In contrast, the agreement was better when ISI oriented errors were dominant, or when the transmission data rate was sufficiently low. It corresponds to the situation where the symbol length was much longer or shorter than the delay dispersion of channels. The results strongly suggested to include the residual components into BEP simulations.

3. Thirdly, this Chapter *showed that the BEP performance prediction improved by taking the diffuse paths into account.* Modeling of the residual components were done using PDP, and we assumed that the residual components had uniform distribution over tha angular domains. Based on the model, the residual components were simulated as diffuse paths by means of the Monte-Carlo simulations. By including the diffuse paths, it was confirmed that the agreement of BEP from reconstructed channels and stored channels were much better in all the simulated we tested, irrespective of environment under consideration, modulation format, and symbol length. The demonstrated results suggested the propagation modeling method to separately treat the propagation paths and continuous angular and delay spectrum.

4. Finally, this Chapter *found that the local BEP was not as accurate as the average BEP characteristics.* This was because the propagation modeling utilized multi-dimensional power angular-delay profile, not the CIR, to determine DOD, DOA, and DT. The accuracy did not improve even considering the diffuse paths, because the modeling of residual components were also done in the same manner. The limited modeling capability in power extraction affected the accuracy of local BEP prediction seriously.

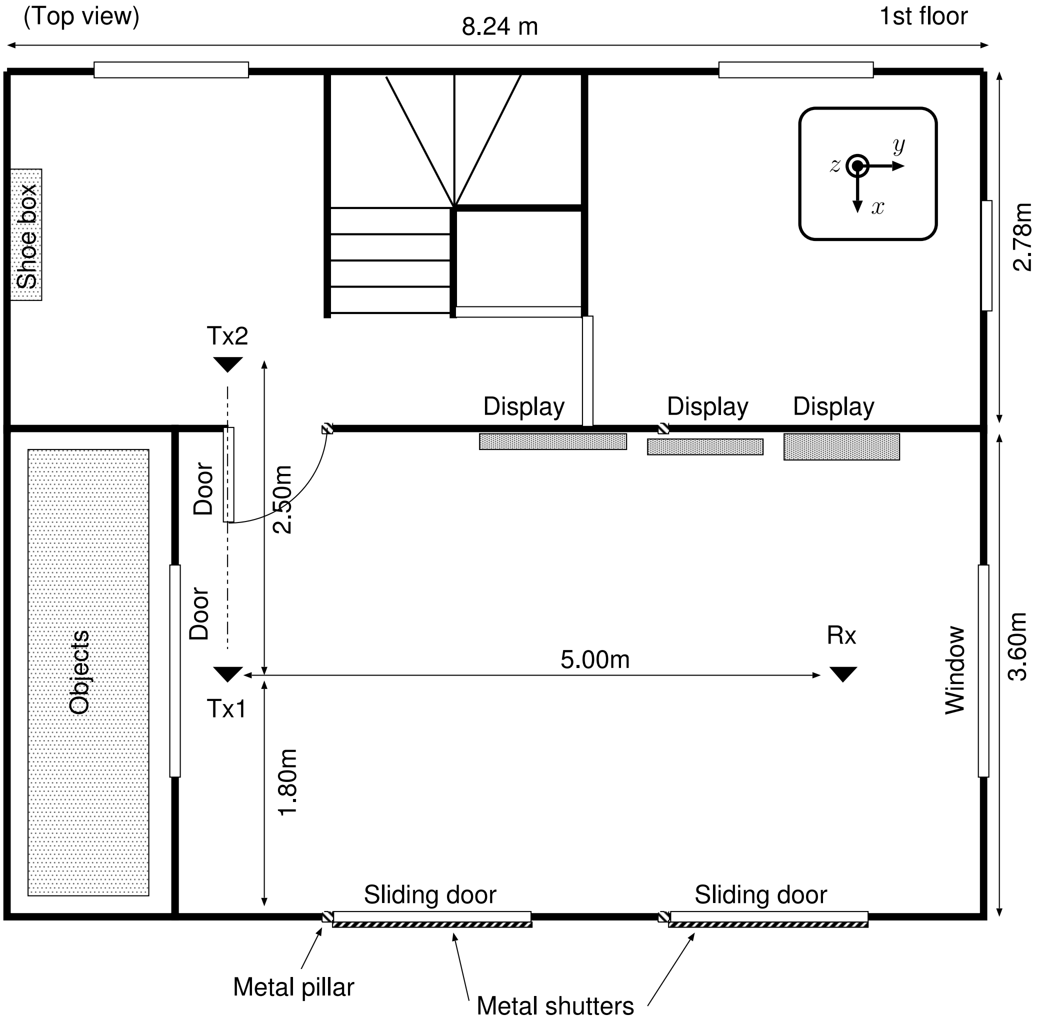

Figure 5.1 Floor plan of the UWB double-directional spatio-temporal channel sounding campaign in a home environment.

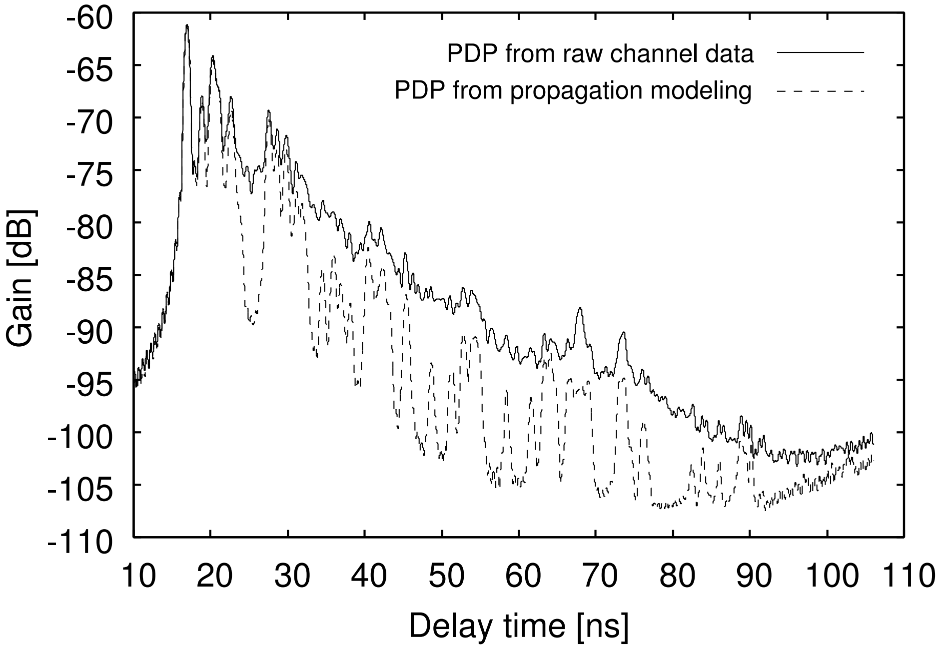

(a)

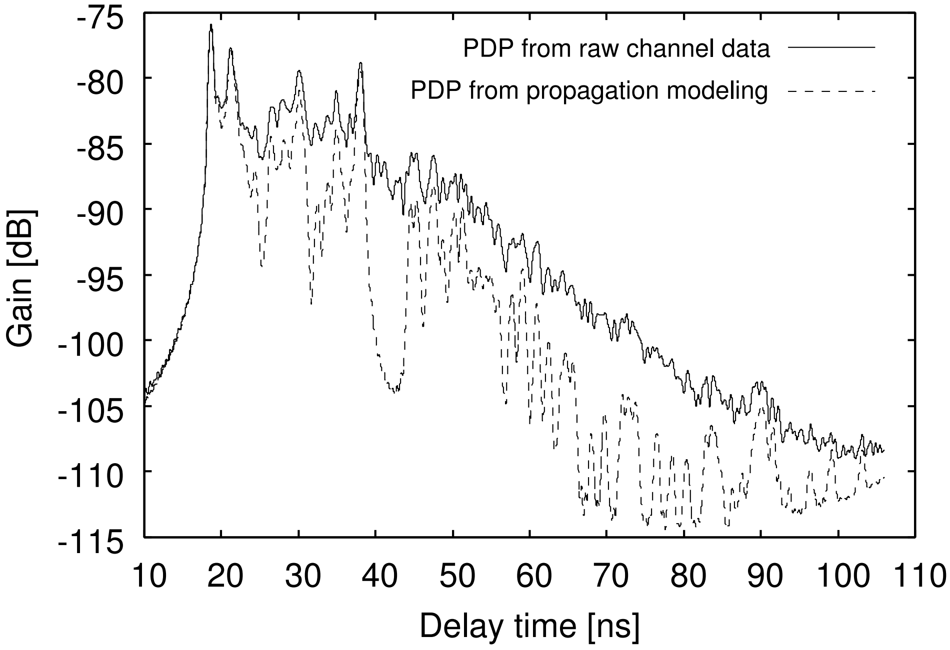

(b)

Figure 5.2 PDP derived from raw channel data (solid line). PDP reconstructed from the propagation modeling results is overlayed (dashed line): (a) Scenario I and (b) Scenario II.

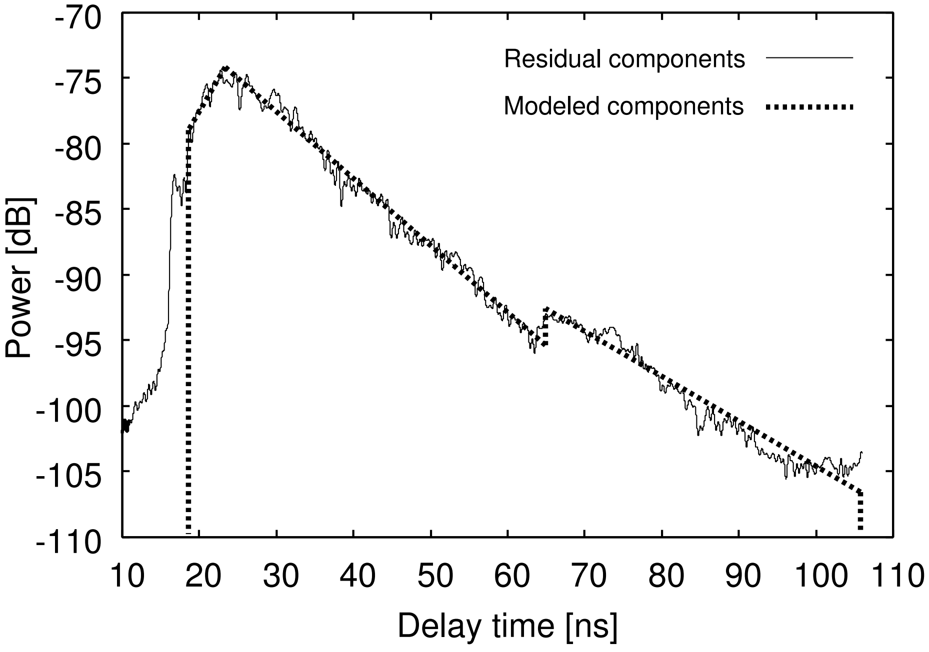

(a)

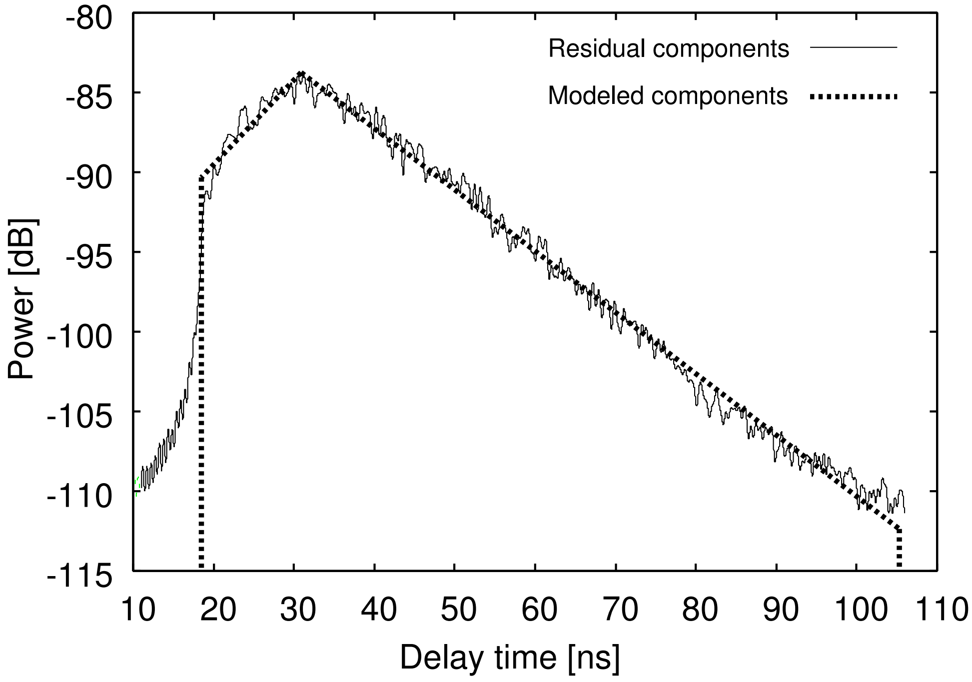

(b)

Figure 5.3 PDP of the residual components and its modeling results using the concatination of several exponential distributions: (a) Scenario I and (b) Scenario II.

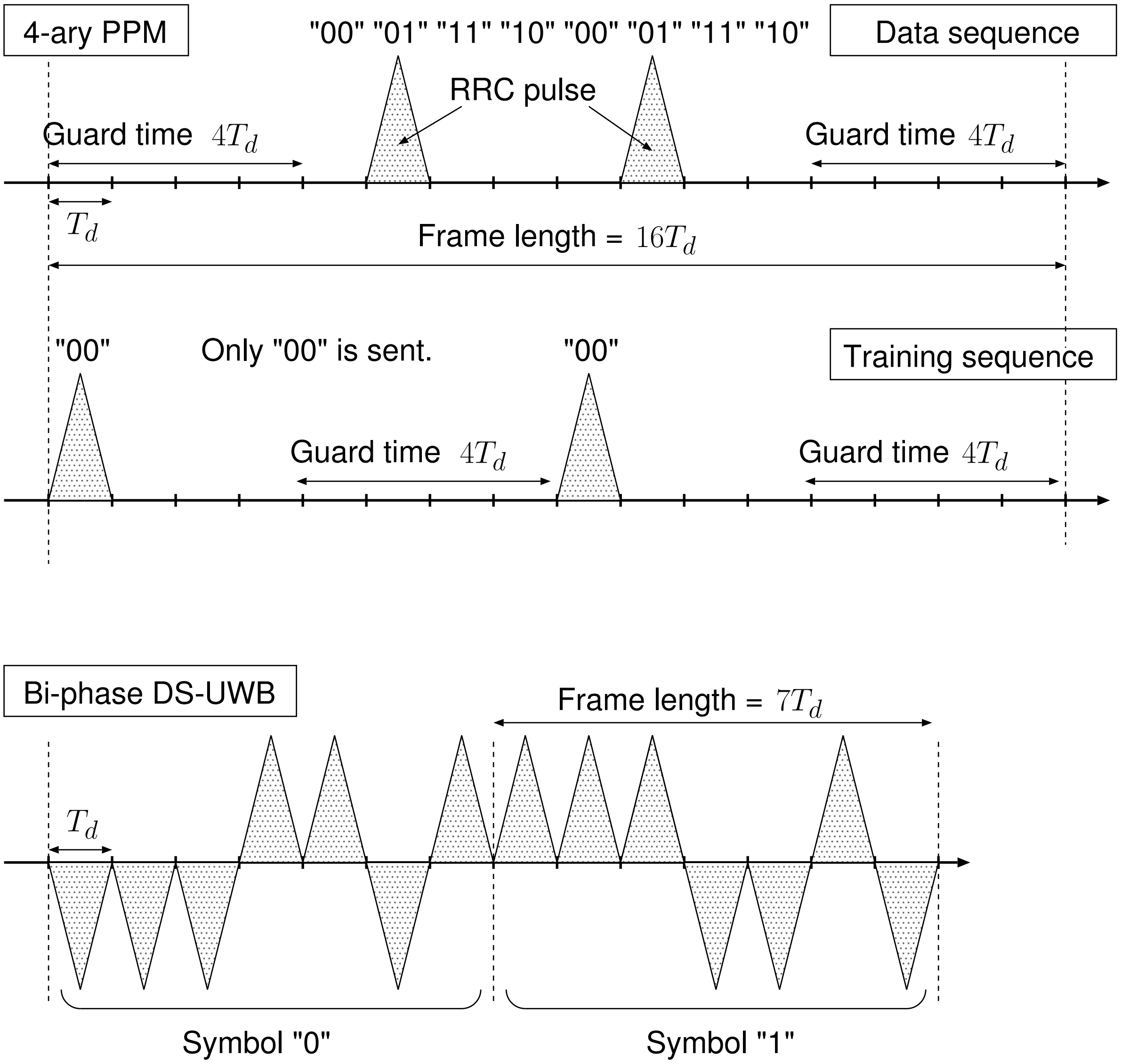

Figure 5.4 Frame format of the UWB transmission simulations for 4-ary PPM and bi-phase DS-UWB systems.

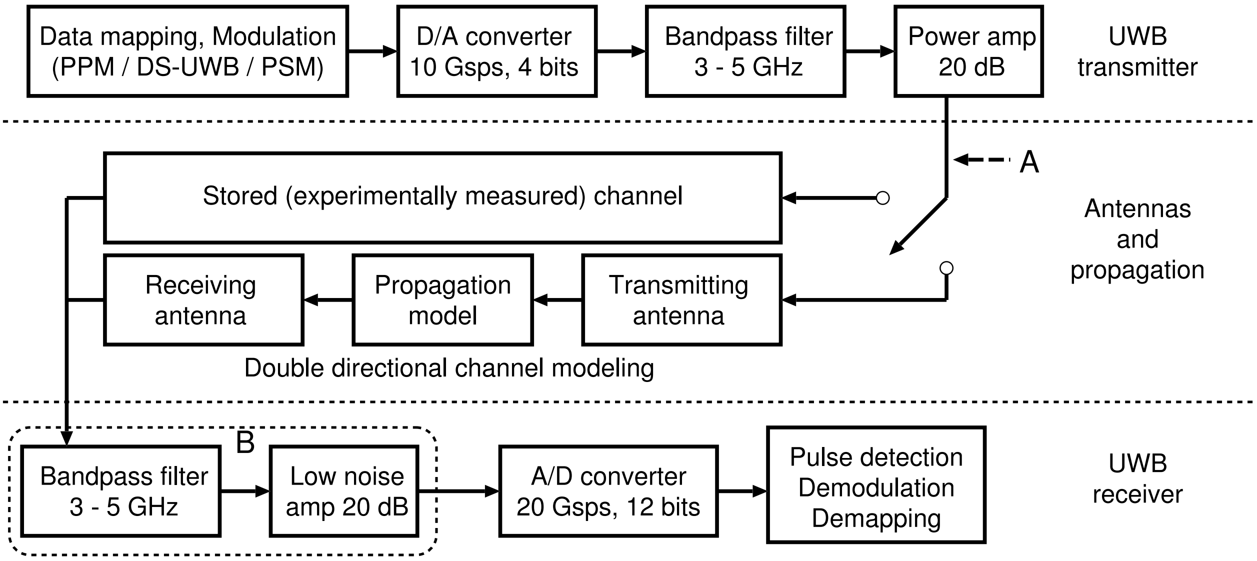

Figure 5.5 Block diagram of the UWB transmission simulation using stored channels and propagation modeling results. The flow was actually implemented in the UWB testbed [9, Sect. 2.1].

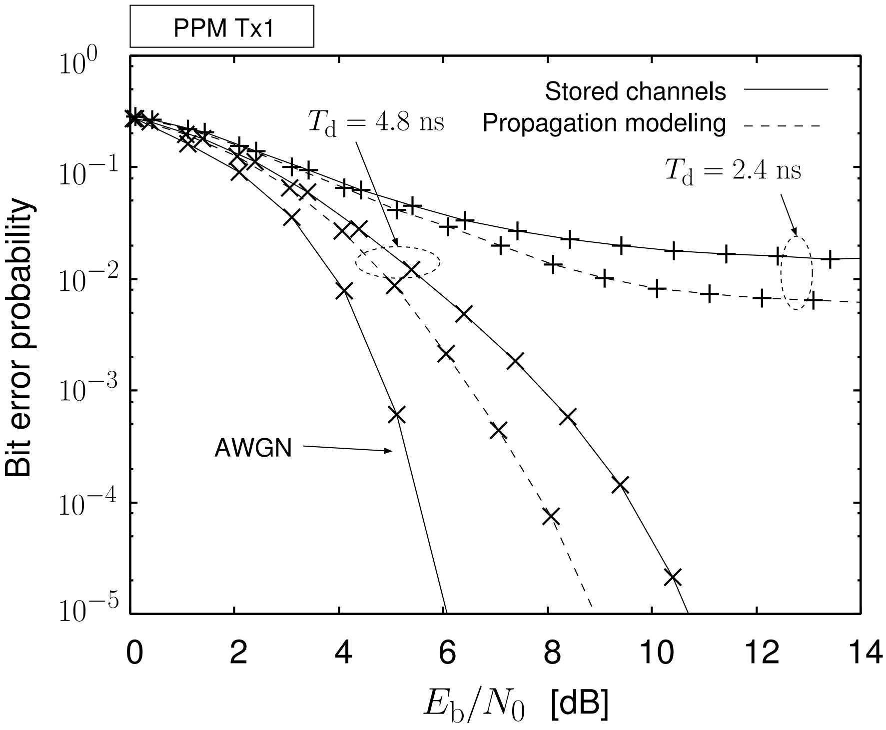

(a)

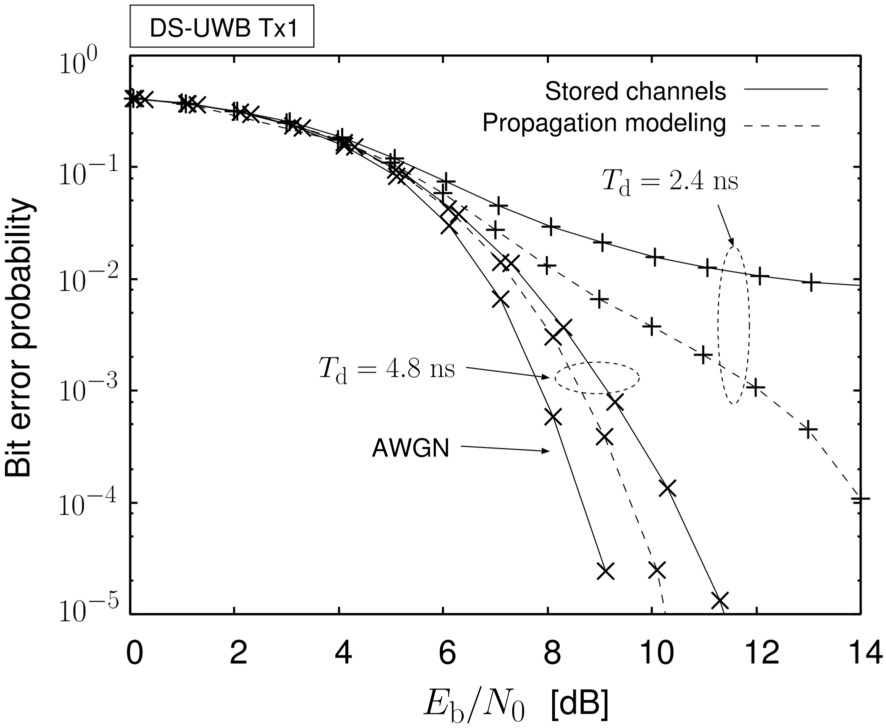

(b)

Figure 5.6 E_b/N_0 versus average BEP for Scenario I: (a) 4-ary PPM and (b) bi-phase DS-UWB.

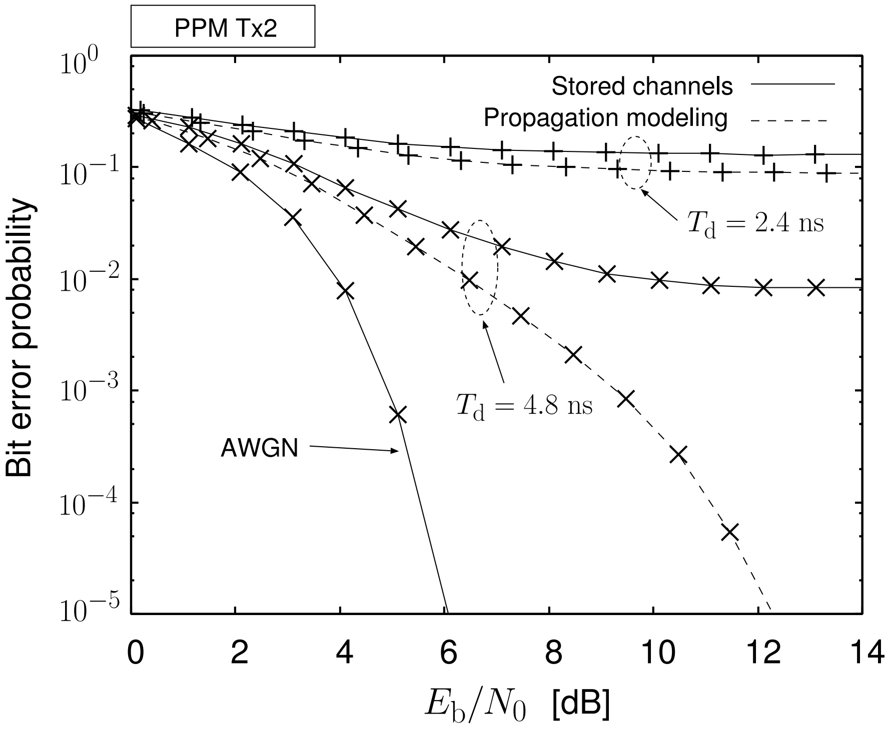

(a)

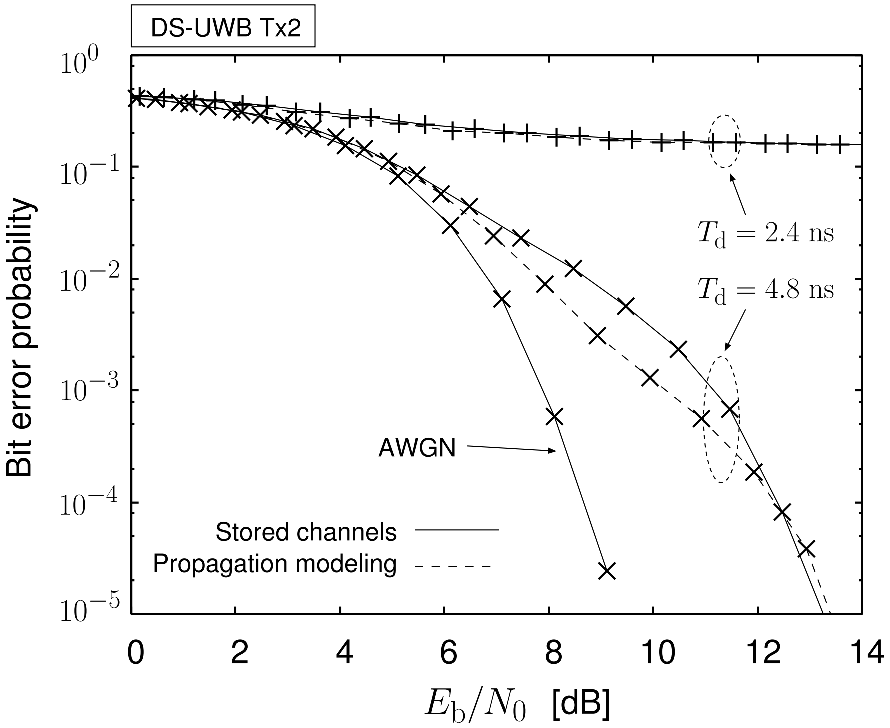

(b)

Figure 5.7 E_b/N_0 versus average BEP for Scenario II: (a) 4-ary PPM and (b) bi-phase DS-UWB.

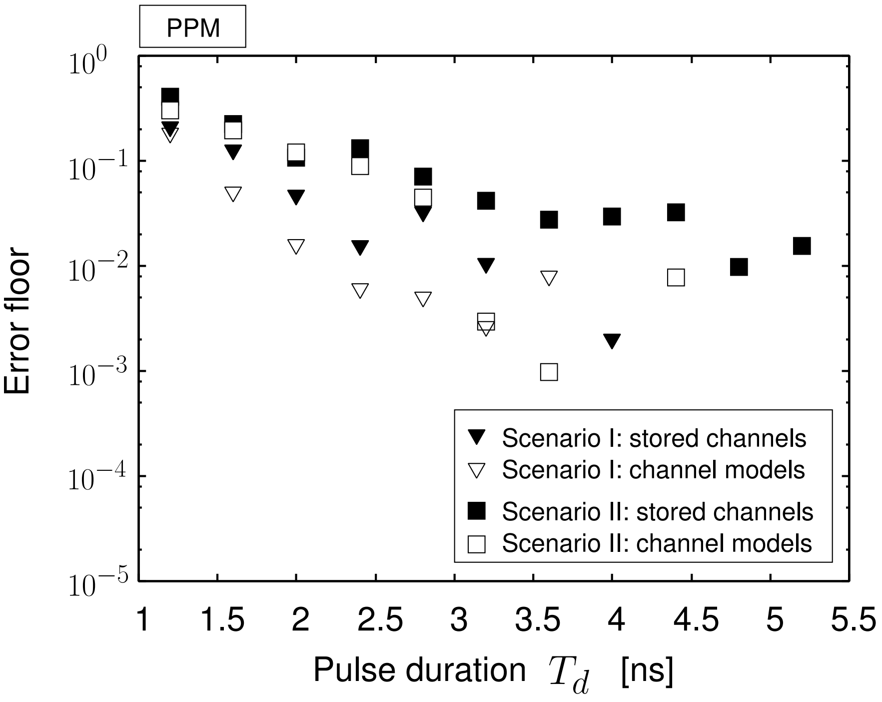

(a) PPM.

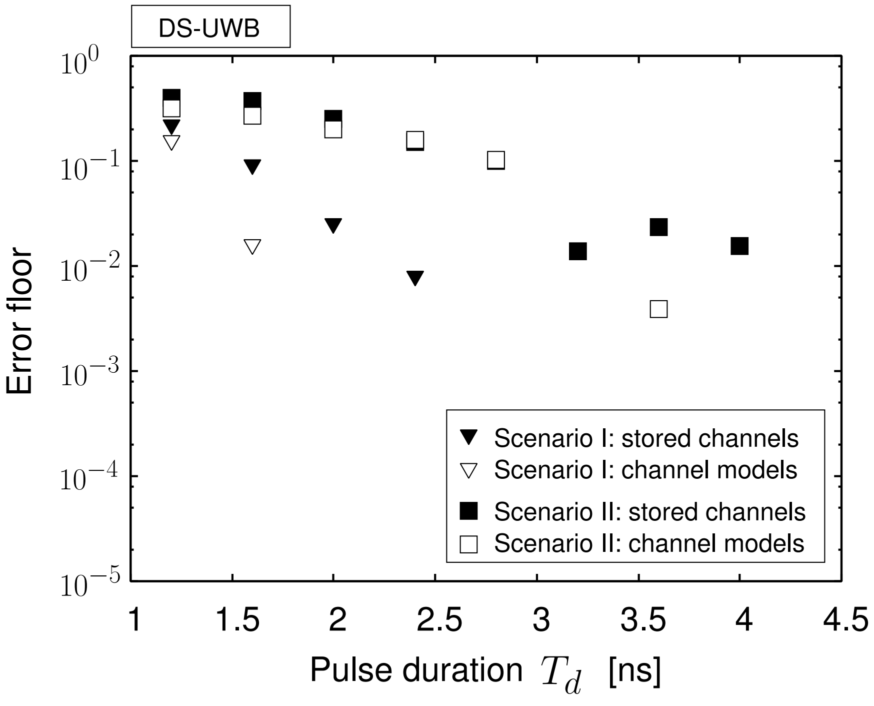

(b) DS-UWB.

Figure 5.8 Error floor of PPM and DS-UWB simulations versus pulse duration T_d in two measurement scenarios.

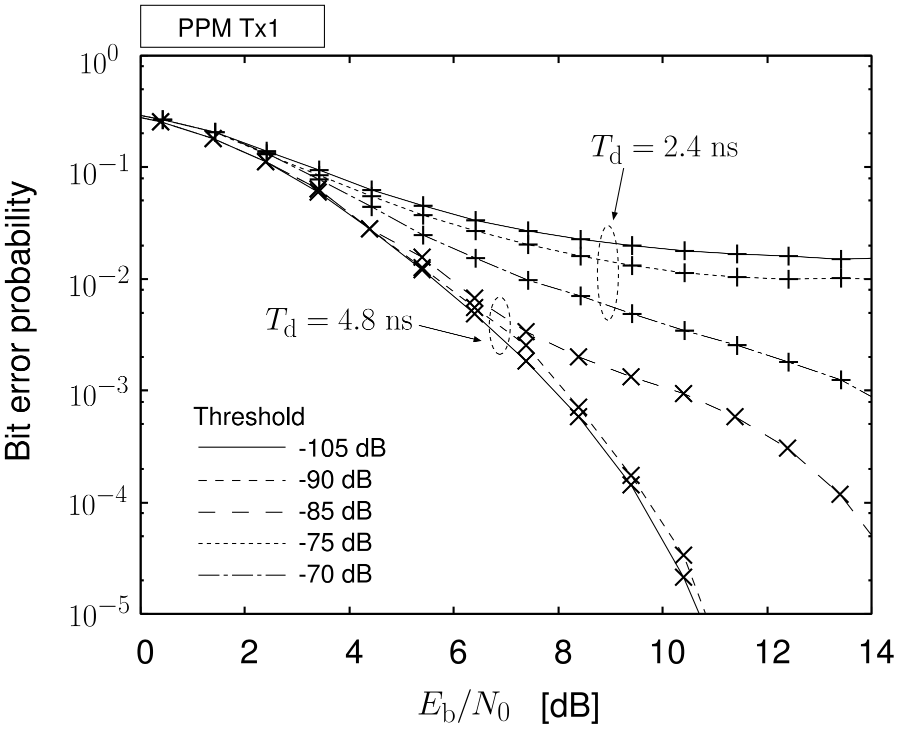

(a)

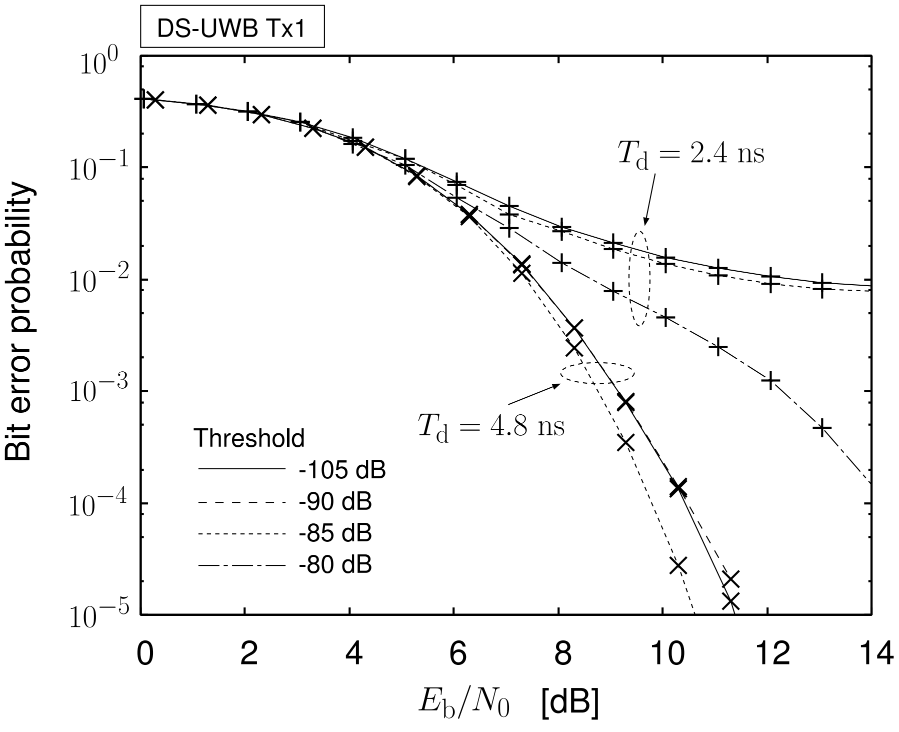

(b)

Figure 5.9 Average BEP characteristics for different threshold level of CIR. Considered channel was Tx1–Rx (Scenario I), and the analysis is for raw channel data: (a) 4-ary PPM and (b) DS-UWB.

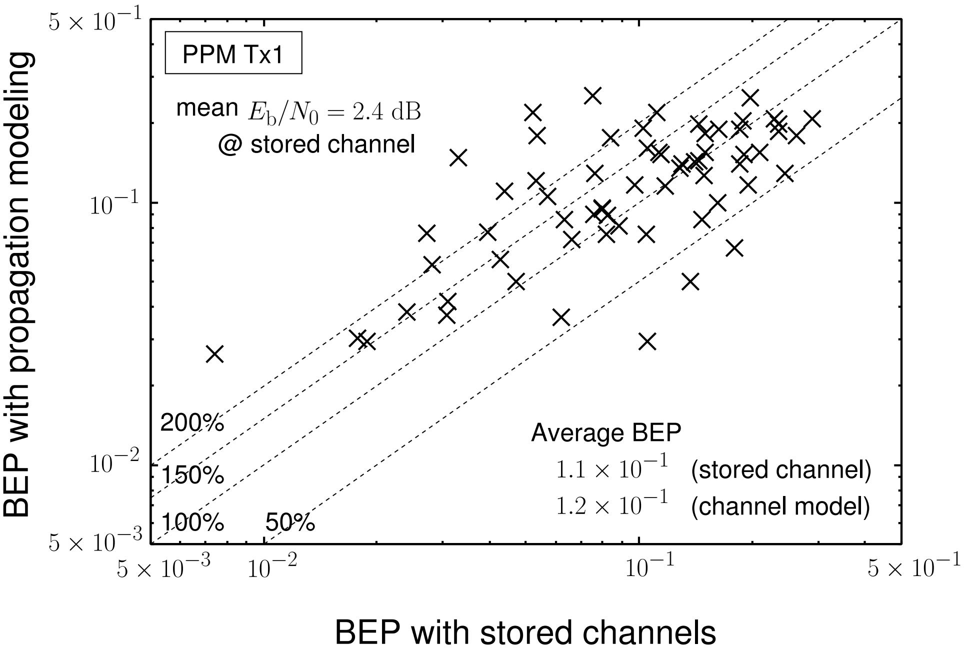

(a)

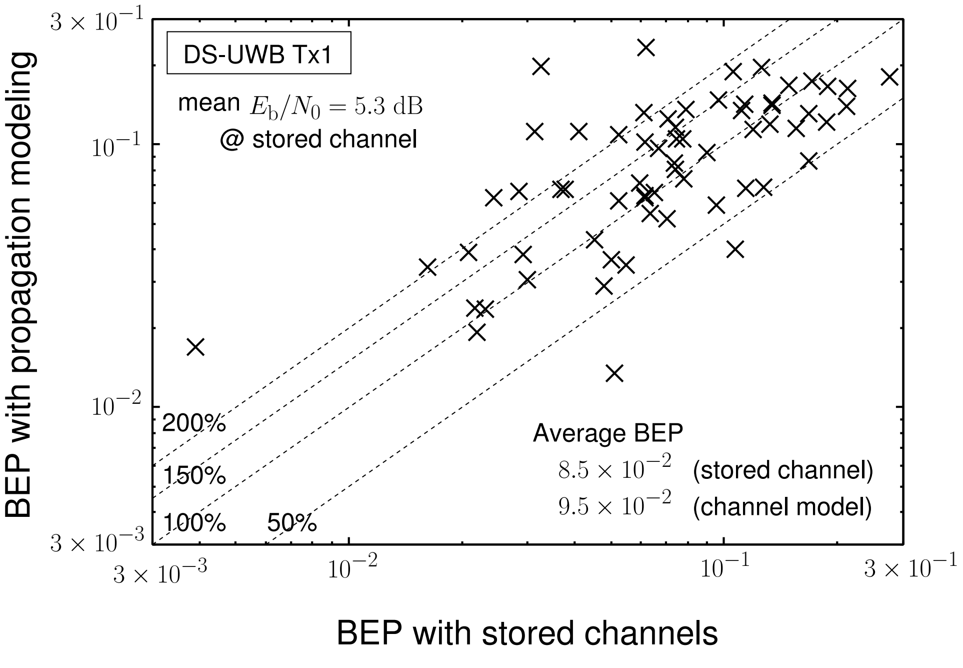

(b)

Figure 5.10 Scattered plot of the local BEP using stored channels versus that from propagation modeling results. Considered channel was Tx1–Rx (Scenario I): (a) 4-ary PPM and (b) DS-UWB.

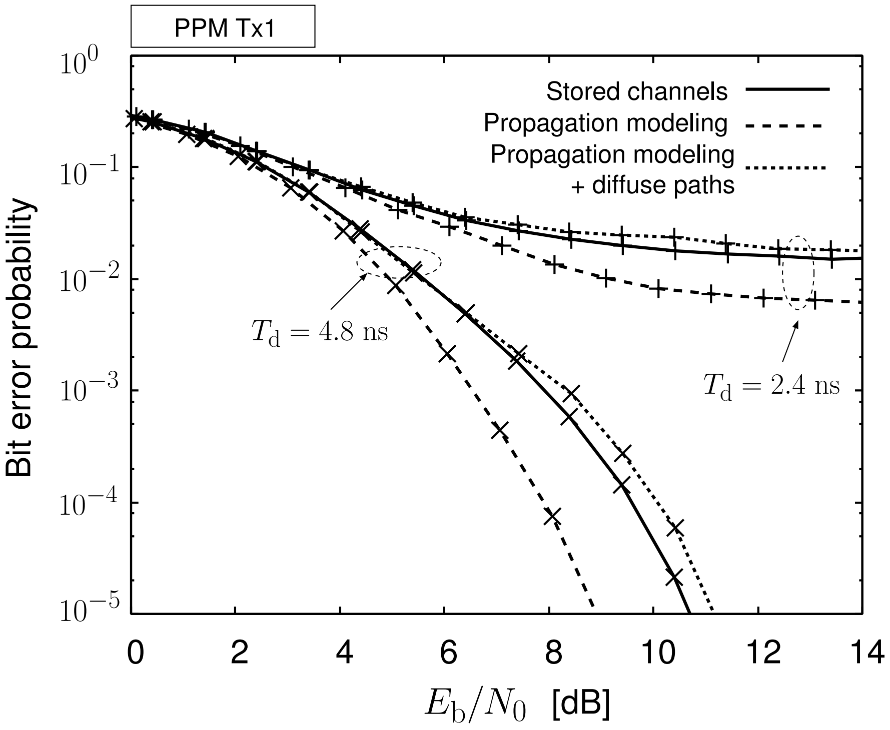

(a)

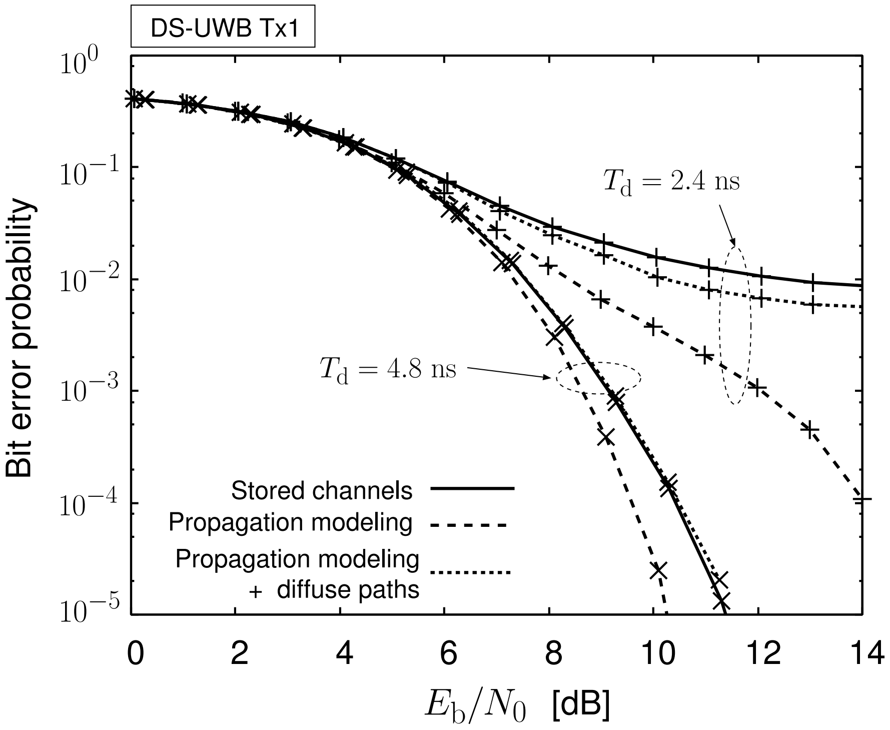

(b)

Figure 5.11 BEP performance considering the diffuse paths in Scenario I: (a) 4-ary PPM and (b) DS-UWB.

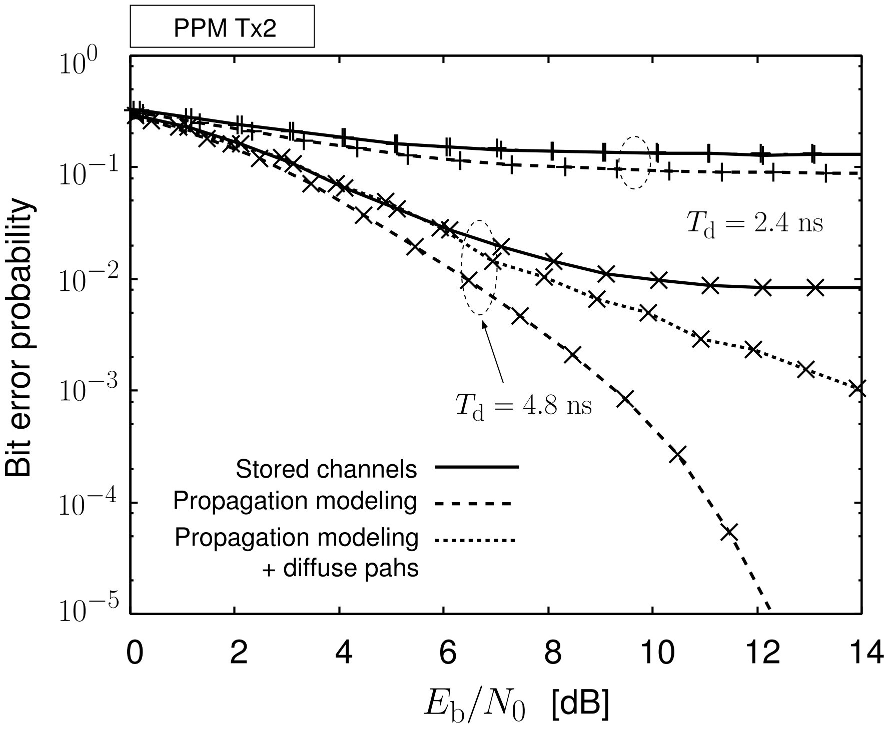

(a)

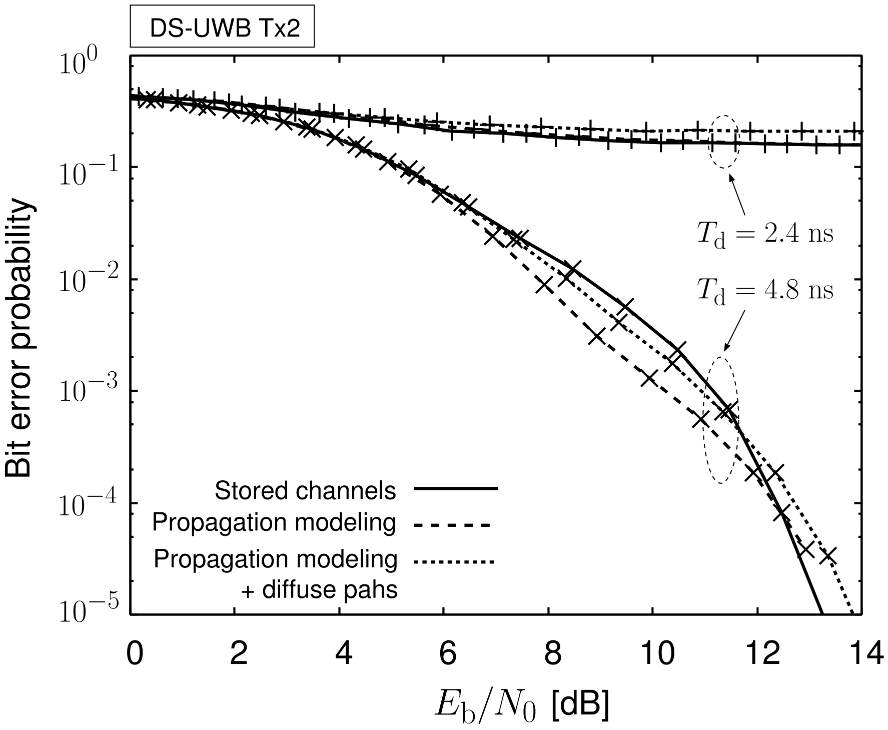

(b)

Figure 5.12 BEP performance considering the diffuse paths in Scenario II: (a) 4-ary PPM and (b) DS-UWB.

Chapter6

Conclusion

This thesis covered a comprehensive set of discussions related to high-resolution radio wave propagation modeling in indoor environments. The trigger of this study was to establish a channel sounding method achieving far better angular and delay resolution of propagation paths to characterize rich multipaths in short-range wireless communications. Improving the delay resolution using the UWB signal had a potential to fulfil this requirement. At the beginning of our research, the regulation activities on spectrum mask and radio license for UWB systems also just started. This activity made our research activity meaningful with respect to the contribution to a specific wireless system. Furthermore, next generation WLAN systems gave another possibility where our channel sounding and propagation modeling could contribute to. The next WLAN systems take into account MIMO systems to increase data rates without expanding the use of frequency resources. This is specifically realized by exploiting spatial (angular) information at both link ends, thus multi-element antennas are installed at the terminals. The potential of MIMO systems created a demand to treat propagation channels and antenna properties separately, since the antenna design should be optimized under various propagation environment. Here the double-directional channel sounding concept was invented, but it simultaneously improved path resolution because it utilized full angular information. As such, demands for short-range wireless communication begun to emerge, and the wireless systems have started to flourish into diverse kinds of applications nowadays. The applications are not only for high-data rate communications, but also for low-data rate communications such as networks for home security and for medical purposes. Given the innovations of wireless systems, we believe that high-resolution characterization and modeling of indoor radio wave propagation will play an important role in realizing further facilitation of wireless systems.

With the aim to conduct high-resolution channel sounding and propagtion modeling, we first developed a UWB double-directional channel sounder. In Chapter2, the measurement apparatus realizing the UWB double-directional channel sounder was given. As a propagation modeling method, a parametric channel estimation method was employed, since the treatment of multipath propagation using a set of discrete paths was intuitively so simple that made the subsequent analyses easier. Furthemore, we incorporated the spherical wavefront model with the parametric channel estimation algorithm for pursing better fitting of the signal model into physical propagation phenomena. A set of criteria expressing the fundamental performances of the channel sounder, such as angular and delay resolution, and accuracy of parameter estimates, were presented.

Chapter3 examined the proposed UWB double-directional channel sounder by an anehoic chamber test, because the anechoic chamber could realize “a prior known” propagation environment. The test validated that the performances of the channel sounder worked as we expected through the theoretical formulation presented in Chapter2. The achieved angular and delay resolution was 10 deg and 0.67 ns respectively, which had not been realized in the microwave band before our research. The spherical wavefront outperformed the conventional plane wavefront model so that the possibility to increase model-order for improvement of propagation modeling results were suggested. Derived parameters by the parametric channel modeling algorithm was found to be accurate enough to encourage further channel sounding and propagation modeling in a realistic multipath environment.

Eventually channel sounding and propagation modeling were conducted to characterize multipath environments in Chapter4. The site we considered for measurement was a Japanese wooden house, where many short-range wireless systems might be installed in the future. As majority of channel measurement and modeling campaigns had been performed in office and hall environments, our measurement campaigns revealed a distinguished value in channel models. Accordingly, the modeling results were contributed to two channel modeling activities: 1) COST273 MIMO channel model, and 2) IEEE802.15.4a channel model. In the former model, our parameters were approved as a representative parameter sets for home environments, which are to be used all over the world. The parameters we contributed to the standard channel models were based on the cluster treatment of propagation paths. Specifically, in light of physical propagation phenomena, such as reflection, diffraction, and penetration, the following cluster parameters were investigated: cluster angular and delay spread, scattering coefficients, power composition of clusters. It is obvious that the results presented in Chapter4 had more meaning than just contributing to the standardized channel models. The results could also be used to strengthen deterministic channel simulation methods, such as ray-tracing.

Finally, in Chapter5, we assessed the UWB transmission performance using the propagation modeling results. Popular modulation formats of UWB systems, namely DS-UWB and PPM, were considered to derive BEP. The BEP results revealed that the transmission simulation using propagation modeling results were not always capable of simulating BEP characteristics accurately. This was mainly due to the residual components that were not modeled as propagation paths using the parametric channel estimator. Further investigation revealed that the accuracy of BEP prediction improved by considering the residual components into simulations as diffuse paths. This suggested that the propagation modeling should be performed separately for discrete propagation paths and continuous multi-dimensional power angular/delay spectrum.

6.1 Future Research Topics

Progress of channel sounding methods and propagation modeling approaches have been providing many important insights for further improvement, innovation and challenges. In this last section of the thesis, we summarize several topics that should be further investigated in the future from our research point of view.

6.1.1 Propagation Modeling Methods

The parametric channel modeling requires an underlying signal model to fit the measured data. If the signal model is not accurate, the parametric channel modeling can characterize only a limited part of measured data. Basically increasing the model-order can achieve better fitting of the data, and the spherical wavefront was the realization which we took. However, it also has several drawbacks: 1) the spherical wavefront is still not sufficient to model the real physical phenomena properly. Even a simple diffraction yielded by the uniform theory of diffraction (*e.g.*, [71]) cannot be exaclty modeled as spherical wavefronts. 2) the spherical wavefront is incompatible with the simultaneous DOD and DOA estimation as we pointed out in Chapter2. It is possible to conduct the double-directional channel sounding with the spherical wavefront by concatinating two single directional channel sounding as reported in [17, 41, 52], but coupling of propagation paths extracted on Tx and Rx sides were quite hard except for dominant propagation paths.

Another aspect that requires further consideration is the better modeling of residual components. As suggested in Chapter5, it is essential to model the components for accurate evaluation of transmission performance. Although we modeled the components in the delay domain, and treated the angular characteristics using a uniform distribution, the modeling should be performed in a refined way; that is, modeling in the double-directional angular-delay domain is necessary for better accuracy. One potential solution for this issue have been proposed by Ribeiro et al. [89]. It proposed to characterize the multi-dimensional power angular-delay profile by a superposition of a certain distribution. In contrast to the plane and spherical wavefronts which assumed propagation path as the dirac delta function on the angular-delay domain, the modeling assumed that each propagation path had a certain range of distribution in angular and delay domains. The research actually utilized the von Mise distribution to express the path distribution. Although there are discussions as to the physical meaning of the path distribution, it can be a powerful tool to characterize angular-delay profile of propagation channels without considering the separated propagation paths and diffuse components.

6.1.2 Complex Antenna Directivity Measurement Covering UWB Bands

In the propagation modeling procedure, the antenna deconvolution largely affects the accuracy of resultant propagation modeling. Ideal antenna deconvolution requires complex antenna directivity covering whole solid angles for all polarization states. Thus far, there was no measurement apparatus realizing such a kind of measurement. The main issues to be tackled for the development of the apparatus realizing the 3-D polarimetric antenna pattern measurement are: 1) development of polarimetric sensors covering wide frequency range, and 2) development of a mechanical structure which enables the measurement of the whole solid angle. Particularly, the cylindrical near-field measurement can be a feasible solution for antennas of our interests. The cylindrical antenna directivity evaluation reveals the poorest performance towards $\pm z$ directions, but this is not a significant problem for the antennas having nulls towards the directions. The near-field antenna directivity evaluation requires an additional signal processing algorithm to convert the measured data into a far-field pattern, and the algorithm can be realized using a simple Fourier transform as far as electrically small antennas are concerned.

6.1.3 Frequency Dependence of Propagation Channels

The measurement results reported in this thesis was basically done with the full bandwidth in the microwave band, from 3.1 to 10.6 GHz. However, the standardization activities of UWB transmission systems [10, 11] decided to use only part of the frequency bands for the purpose of the coexistence with systems in service. The recently announced radio license for UWB systems in Japan [6] also prohibits the use of 5 GHz band in order to protect WLAN systems. The use of UWB band was eventually divided into low- and high-bands spanning below 5 GHz and above 6 GHz, respectively. The first deployment of UWB systems uses the low-band, and the high-band is left for the potential band when exploring additional frequency resouces in the future. Reflecting these situations, propagation characteristics should be investigated for different frequency bands. Propagation modeling for the low-band is a much more urgent issue than the high-band, but analysis in high-band and the comparison of propagation characteristics between low- and high-bands are also emerging tasks.

6.1.4 Area Propagation Measurement and Modeling

In WLAN and WPAN systems, it is expected that mobile terminals move around inside an environment, and therefore, investigation of dynamic propagation channel properties is important. However, as our channel sounding campaigns were conducted only in one spatial point in a certain scenario, modeling results were not able to be used for the dynamic propagation modeling. It is highly suggested that the UWB double-directional channel sounding cover more environments, and wider areas in the environment. The area propagation measurement and modeling enables us to investigate how propagation paths change if the antenna terminal moves to different positions. It simultaneously helps us generalize dominant propagation phenomena, and the result is a versatile tool to simulate wireless communication systems in indoor environments. Furthermore, in the stochastic modeling point of view, sufficient data samples can be assured by the area propagation measurement and modeling, contributing to the increase of reliability of modeling results.

Reference

[1] http://ieee802.org/11/ .

[2] http://ieee802.org/15/ .

[3] S. Gecizi, Z. Tian, G. B. Giannakis, Z. Sahinoglu, H. Kobayashi, A. F. Molisch, and H. V. Poor, "Location via ultra-wideband radios," *IEEE Commun. Mag.,* vol. 22, no. 4, pp. 70–84, 2005.

[4] Federal Communications Commission, "Revision of part 15 of the commission's rules regarding ultra-wideband transmission systems," *First Report and Order*, FCC 02–48, Apr. 2002.

[5] http://www.tele.soumu.go.jp/j/freq/ (In Japanese).

[6] http://www.soumu.go.jp/s-news/2006/060327_3.html (In Japanese).

[7] Y. Suzuki and T. Kobayashi, "Ultra wideband signal propagation in desktop environments," *IEICE Trans. Fundamentals*, vol. E88–A, no. 9, p. 2272–2278, Sep. 2005.

[8] T. Kobayashi, "Measurements and characterization of ultra wideband propagation channels in a passenger-car compartment," *IEICE Trans. Fadamentals*, vol. E89–A, no. 11, pp. 3089–3094, Nov. 2006.

[9] K. Takizawa, H. B. Li, I. Nishiyama, J. Takada, and R. Kohno, "Overview of research, development, standardization, and regulation activities in NICT UWB Project," *IEICE Trans. Fundamentals*, vol. E89–A, no. 11, pp. 2996–3005, Nov. 2006.

[10] M. Welborn et al., "DS-UWB physical layer submission to 802.15 task group 3a (04/137r)," IEEE P802.15-04/137r3, Mar. 2004.

[11] A. Batra et al., "Multi-band OFDM physical layer submission to 802.15 task group 3a (04/268r)," IEEE P802.15-03/268r3, Nov. 2003.

[12] T. Kobayashi and S. Koya, "Overview of research and development in ultra wideband wireless systems," *IEICE Trans. Fundamentals,* vol. J86–A, no. 12, pp. 1264–1273, Dec. 2003 (In Japanese).

[13] A. F. Molisch, "Ultrawideband propagation channels–theory, measurement, and modeling," *IEEE Trans. Veh. Tech.,* vol. 54, no. 5, pp. 1528–1545, Sep. 2005.

[14] K. Kalliola, H. Laitinen, L. I. Vaskelainen and P. Vainikainen, "Real-time 3D spatial–temporal dual-polarized measurement of wideband radio channel at mobile station," *IEEE Trans. Instrum. Meas.*, vol. 49, no. 2, pp. 439–448, Apr. 2000.

[15] B. H. Fleury, X. Yin, K. G. Rohbrandt, P. Jourdan, and A. Stucki, "Performance of a high-resolution scheme for joint estimation of delay and bidirection dispersion in the radio channel," in *Proc. IEEE 55th Vehicular Technology Conference (VTC 2002 Spring)*, May 2002.

[16] Y. Xuefeng, B. H. Fleury, P. Jourdan, and A Stucki, "Polarization estimation of individual propagation paths using the SAGE algorithm," in *Proc. 14th Int. Symp. Personal, Indoor and Mobile Radio Commun. 2003 (PIMRC 2003)*, vol. 2, pp. 1795–1799, Beijing, China, Sep. 2003.

[17] K. Kalliola, H. Laitinen, P. Vainikainen, M. Toeltsch, J. Laurila, and E. Bonek, "3-D double-directional radio channel characterization for urban macrocellular applications," *IEEE Trans. Antennas Propagat.*, vol. 51, no. 11, pp. 3122–3133, Nov. 2003.

[18] V. Kolmonen, J. Kivinen, L. Vuokko, and P. Vainikainen, "5.3-GHz MIMO channel sounder," *IEEE Trans. Instrm. Meas.*, vol. 55, no. 4, pp. 1263–1269, Aug. 2006.

[19] M. Ghoraishi, J. Takada, and T. Imai, "Identification of scattering objects in microcell urban mobile propagation channel," *IEEE Trans. Antennas Propagat.*, vol. 54, no. 11, pt. 2, pp. 3473–3480, Nov. 2006.

[20] A. A. M. Saleh and R. A. Valenzuela, "A statistical model for indoor multipath propagation," *IEEE J. Select. Areas Commun.*, vol. 5, no. 2, pp. 128–137, Feb. 1987.

[21] B. H. Fleury, M. Tschudin, R. Heddergott, D. Dahlhaus, and K. I. Pedersen. "Channel parameter estimation in mobile radio environments using the SAGE algorithm," *IEEE J. Select. Areas Commun.*, vol. 17, no. 3, pp. 434–449, Mar. 1999.

[22] R. J. Cramer, R. A. Scholtz, and M. Z. Win, "Evaluation of an ultra-wide-band propagation channel," *IEEE Trans. Antennas Propagat.*, vol. 50, no. 5, pp. 561–570, May 2002.

[23] D. Cassioli, M. Z. Win, and A. F. Molisch, "The ultra-wide bandwidth indoor channel: from statistical model to simulations," *IEEE J. Select. Areas Commun.*, vol. 20, No. 5, pp. 1247–1257, Aug. 2002.

[24] M. Z. Win and R. A. Scholtz, "Characterization of ultra-wide bandwidth wireless indoor channels: a communication-theoretic view," *IEEE J. Select. Areas Commun.*, vol. 20, no. 9, pp. 1613–1627, Dec. 2002.

[25] D. Cassioli and A. Durantini, "Statistical characterization of UWB indoor propagation channels based on extensive measurement campaigns," in *Proc. Int. Conf. Wireless Personal and Multimedia Communications 2004 (WPMC '04)*, vol. 1, pp. 236–240, Abano Terme, Italy, Sep. 2004.

[26] D. Cassioli, A. Durantini, and W. Ciccognani, "The role of path loss on the selection of the oeprating bands of UWB systems," in *Proc. IEEE Int. Symp. Personal, Indoor and Mobile Radio Communications (PIMRC 2004)*, pp. 2787–2791, Barcelona, Spain, Sep. 2004.

[27] R. S. Thomä, D. Hampicke, A. Richter, G. Somerkorn, A. Schneider, U. Trautwein, and W. Wirnitzer, "Identification of time-variant directional mobile radio channels," *IEEE Trans. Instrum. and Meas.*, vol. 49, no. 2, pp. 357–364, Apr. 2000.

[28] M. Steinbauer, A. F. Molisch, and E. Bonek, "The double directional radio channel," *IEEE Antennas and Propagat. Mag.*, vol. 43, no. 4, pp. 51–63, Aug. 2001.

[29] K. Sakaguchi, J. Takada, and K. Araki, "A novel architecture for MIMO spatio-temporal channel sounder," *IEICE Trans. Electron.*, vol. E85–C, no. 3, pp. 436–441, Mar. 2002.

[30] C. C. Chong, C. M. Tan, D. I. Laurenson, S. McLaughlin, M. A. Beach, and A. R. Nix, "New statistical model wideband spatio-temporal channel model for 5-GHz band WLAN systems," *IEEE. J. Select. Areas Commun.*, vol. 21, no. 2, pp. 139–150, Feb. 2003.

[31] R. Zetik, R. Thomä, and J. Sachs, "Ultra-wideband real-time channel sounder design and application," presented in *URSI Int. Symp. Electromagnetic Theory*, Pisa, Italy, May 2004.

[32] T. Zwick, D. Hampicke, A. Richter, G. Sommerkorn, R. S. Thomä, and W. Wiesbeck, "A novel antenna concept for double-directional channel measurements," *IEEE Trans. Veh. Tech.* , vol. 53, no. 2, pp. 527–537, Feb. 2004.

[33] A. J. Johansson, J. Karedal, F. Tufvesson, and A. F. Molisch, "MIMO channel measurements for personal area networks," in *Proc. 61st IEEE Veh. Tech. Conf. 2005 (VTC 2005 Spring)*, vol. 1, pp. 171–176, Stockholm, Sweden, May 2005.

[34] C. M. Tan, C. M. Chin, M. L. Sim, and M. A. Beach, "Modelling the general dependency between directions of arrival and departure for an indoor MIMO channel," in *Proc. 63rd IEEE Veh. Tech. Conf. 2006 (VTC 2006 Spring)*, vol. 6, pp. 2878–2882, Melbourne, Australia, May 2006.

[35] K. Sivasondhivat, J. Takada, M. Landmann, I. Ida, and Y. Oishi, "Street dependency propagation at MS based on urban macrocellular measurement," in *Proc. 1st European Conf. Antennas & Propagat. (EuCAP 2006)*, Nice, France, Nov. 2006.

[36] Q. H. Spencer, B. D. Jeffs, M. A. Jensen, and A. L. Swindlehurst, "Modeling the statistical time and angle of arrival characteristics of an indoor multipath channel," *IEEE J. Select. Areas Commun.*, vol. 18, no. 3, pp. 347–359, Mar. 2000.

[37] H. Suzuki and A. S. Mohan, "Measurement and prediction of high spatial resolution indoor radio channel characteristic map", *IEEE Trans. Veh. Technol.*, vol. 49, no. 4, pp. 1321–1333, July 2000.

[38] R. D. Tingley and K. Pahlavan, "Space-time measurement of indoor radio propagation," *IEEE Trans. Instrum. and Meas.*, vol. 50, no. 1, pp. 22–31, Feb. 2001.

[39] J. Kunisch and J. Pamp, "Measurement results and modeling aspects for the UWB radio channel," in *Proc. IEEE Conf. on Ultra Wideband Systems and Technologies 2002 (UWBST 2002)*, pp. 19–23, Baltimore, MD, USA, May 2002.

[40] J. Keignart and N. Daniele, "Subnanosecond UWB channel sounding in frequency and temporal domain," in *Proc. IEEE Conf. on Ultra Wideband Systems and Technologies 2002 (UWBST 2002)*, pp. 19–24, Baltimore, MD, USA, May 2002.

[41] K. Haneda and J. Takada, "High-resolution estimation of NLOS indoor MIMO channel with network analyzer based system," in *Proc. 14th Int. Symp. Personal, Indoor, and Mobile Radio Commun. 2003 (PIMRC 2003)*, pp. 675–679, Beijing, China, Sep. 2003.

[42] A. Alvarez, G. Valera, M. Lobeira, R. Torres, and J. L. Garcia, "New channel impulse response model for UWB indoor system simulations," in *Proc. IEEE 57th Vehicular Technology Conference (VTC 2003 Spring)*, vol. 1, pp. 1–5, Jeju, Korea, Apr. 2003.

[43] A. S. Y. Poon and M. Ho, "Indoor multiple antenna channel characterization from 2 to 8 GHz," *2003 IEEE Int. Conf. on Commun.*, GC27-3, Anchorage, AK., May 2003.

[44] J. Karedal, S. Wyne, P. Almers, F. Tufvesson, and A. F. Molisch, "Statistical analysis of the UWB channel in an industrial environment," in *Proc. 60th IEEE Veh. Tech. Conf. 2004 (VTC 2004 Fall)*, vol. 1, pp. 25–30, Los Angels, CA, Sep. 2004.

[45] S. S. Ghassemzadeh, R. Jana, C. Rice, W. Turin, and V. Tarokh, "Measurement and modeling of an ultra-wide bandwidth indoor channel," *IEEE Trans. Commun.*, vol. 52, no. 10, pp. 1786–1796, Oct. 2004.

[46] K. Haneda, J. Takada, T. Iwata, Y. Wakinaka, and T. Kunishima, "Exeprimental determination of propagation paths for ETC system–Equipment development and field test–," *IEICE Trans. Fundamentals*, vol. E87–A, no. 11, pp. 3008–3015, Nov. 2004.

[47] J. Karedal, S. Wyne, P. Almers, F. Tufvesson, and A. F. Molisch, "UWB channel measurements in an industrial environment," in *Proc. IEEE Global Telecommunication Conference 2004 (IEEE GLOBECOM '04)*, pp. 3511–3516, vol. 6, Dallas, TX, Nov. 2004.

[48] C. C. Chong and S. K. Yong, "A generic statistical-based UWB channel model for high-rise apartments," *IEEE Trans. Antennas Propagat.*, vol. 53, no. 8, pp. 2389–2399, Aug. 2005.

[49] J. Medbo, M. Riback, H. Asplund, and J. Berg, "MIMO channel characteristics in a small macrocell measured at 5.25 GHz and 200 MHz bandwidth," in *Proc. 62nd IEEE Veh. Tech. Conf. 2005 (VTC 2005 Fall)*, vol. 1, pp. 372–376, Dallas, Tx, Sep. 2005.

[50] J. Medbo, F. Harrysson, H. Asplund, and J. E. Berg, "Measurements and analysis of a MIMO macrocell outdoor-indoor scenario at 1947 MHz," in *Proc. 59th IEEE Veh. Tech. Conf. 2004 (VTC 2004 Spring)*, no.1, pp. 261–265, Milan, Italy, May 2004.

[51] Y. Rikuta, S. Fujita, F. Ohkubo, H. Hosoya, K. Hamaguchi, J. Takada, and T. Kobayashi, "Indoor channel measurement of 26 GHz band UWB communication systems," in *Proc. 2006 Int. Conf. Ultra-Wideband (ICUWB 2006)*, T2B–4, Waltham, MA, Sep. 2006.

[52] H. Tsuchiya, K. Haneda, and J. Takada, "Investigation of ultra-wideband propagation channel based on a cluster scheme," *IEICE Trans. Fundamentals*, vol. E89–A, no. 11, pp. 3095–3102, Nov. 2006.

[53] R. S. Thomä, M. Landmann, G. Sommerkorn, and A. Richter, "Multidimensional high-resolution channel sounding in mobile radio," in *Proc. 21st IEEE Instrum. Meas. Tech. Conf. 2004 (IMTC 04)*, vol. 1, pp. 257–262, Como, Italy, May 2004.

[54] R. S. Thomä, M. Landmann, A. Richter, and U. Trautwein, *Multidimensional High-Resolution Channel Sounding.* in *Smart Antennas in Europe – State-of-the-Art*, EURASIP Book Series, Hindawi Publishing Corporation, New York, USA, 2005.

[55] R. O. Schmidt, "Multiple emitter source location and signal parameter estimation," *IEEE Trans. Antennas Propagat.*, vol. AP–34, no. 3, Mar. 1986.

[56] R. Roy and T. Kailath, “ESPRIT – Estimation of signal parameters via rotational invariance techniques,” *IEEE Trans. Acoust., Speech, Signal Processing*, vol. 37, no. 7, pp. 984–995, July 1989.

[57] M. Haardt and J. A. Nossek, “Simultaneous schur decomposition of several nonsymmetric matrices to achieve automatic pairing in multidimensional harmonic retrieval problems,” *IEEE Trans. Signal Processing*, vol. 46, no. 1, pp. 161–169, Jan. 1998.

[58] A. P. Dempster, N. M. Laird, and D. B. Rubin, “Maximum likelihood from incomplete data via the EM algorithm,” *J. Royal Statist. Soc., Ser.B*, vol. 39, no. 1, pp. 1–38, 1977.

[59] J. A. Fessler and A. O. Hero, “Space-alternating generalized expectation maximization algorithm,” *IEEE Trans. Signal Processing*, vol. 42, pp. 2664–2677, Oct. 1994.

[60] S. Haykin, *Communication Systems*, John Wiely & Sons, New York, 2001 (4th Ed.).

[61] D. Gesbert, M. Shafi, D. S. Shiu, P. Smith, and A. Naguib, “From theory to practice: an overview of MIMO space-time coded wireless systems,” *IEEE J. Select. Areas Commun.*, vol. 21, no. 2, pp. 281–302, Apr. 2003.

[62] V. Erceg et al. “IEEE P802.11 wireless LANs TGn channel models,” IEEE P802.11-03/940r4, May 2004.

[63] J. Foerster et al. “Channel modeling sub-committee report (final),” IEEE P802.15-02/490r1-SG3a, Feb. 2003.

[64] A. F. Molisch et al. “IEEE 802.15.4a channel model – final report,” IEEE P802.15-04/662r0-SG4a, Nov. 2004.

[65] A. F. Molisch, D. Cassioli, C. C. Chong, S. Emami, A. Fort, B. Kannan, J. Karedal, J. Kunisch, H. G. Schantz, K. Siwiak, and M. Z. Win, “A comprehensive standardized model for ultrawideband propagation channels,” *IEEE Trans. Antennas Propagat.*, vol. 54, no. 11, Nov. 2006.

[66] L. M. Correia (eds.), *Towards mobile broadband multimedia networks – COST 273; European co-operation in mobile radio research,* Elsevier, Oxford, UK, May 2006.

[67] http://www.lx.it.pt/cost273/ .

[68] A. F. Molisch, “A generic model for MIMO wireless propagation channels in macro- and microcells,” *IEEE Trans. Signal Processing*, vol. 52, no. 1, Jan. 2004.

[69] L. M. Correia (eds.), *Wireless flexible presonalised communications,* John Wiley & Sons, Chichester, UK, 2001.

[70] F. Tehoffo-Talom, B. Uguen, E. Plouhinec, and G. Chassay, “A site-specific tool for UWB channel modeling,” in *Proc. 2004 International Workshop on Ultra Wideband Systems Joint with Conference on Ultra Wideband Systems and Technologies (UWBST & IWUWBS 2004)*, pp. 61–65, Kyoto, Japan, May 2004.

[71] L. B. Felsen and N. Marcuvitz, *Radiation and Scattering of Waves*, IEEE Press, Piscataway, NJ, USA, 1994.

[72] H. Budiarto, K. Horihata, K. Haneda, and J. Takada, “Polarimetric measurement of non-specular wave scattering from building surface roughness,” in *IEEE Antennas Wireless Propagat. Lett.*, vol. 2, no. 16, pp. 242–245, 2003.

[73] P. Pongsilamanee and H. L. Bertoni, “Specular and nonspecular scattering from building facades,” *IEEE Trans. Antennas and Propagat.,* vol. 52, no. 7, pp. 1879–1889, July 2004.

[74] H. Budiarto, K. Haneda, and J. Takada, “Prediction model for the estimation of non-specular wave scattering characteristics on building surfaces,” in *Proc. Int. Symp. Antennas and Propagation 2004 (ISAP ’04)*, pp. 749–752, Sendai, Japan, Aug. 2004.

[75] http://ultra.usc.edu/uwb_database/ .

[76] S. Promwong, J. Takada, P. Supanakoon, M. Chamchoy, A. Pradabphon, and P. Tangtisanon, “Distortion analysis of UWB pulse caused by trapezoidal antenna,” in *Proc. 26th Electrical Eng. Conf. (EECON26)*, pp. 1494–1499, Chaam, Thailand, Nov. 2003

[77] R. C. Qiu and I. T. Lu, “Wideband wireless multipath channel modeling with path frequency dependence,” in *Proc. 1996 IEEE Int. Conf. Commun. (ICC 96)*, vol. 1, pp. 277–281, Dallas, TX, USA, June 1996.

[78] A. Ohmae, M. Takahashi, and T. Uno, “Loclization of sources in the finite distance using MUSIC algorithm by the spherical mode vector,” *Technical report of IEICE*, AP2003–64/SAT2003–56/MW2003–70/OPE2003-57, July 2003 (In Japanese).

[79] T. Taniguchi, A. Maeda, and T. Kobayashi, “Development of an omnidirectional and low-VSWR ultra wideband antenna,” *Int. J. Wireless & Opt. Commun.*, vol. 3, no. 2, pp. 145–157, 2006.

[80] H. T. Friis, “A note on a simple transmission formula,” in *Proc. IRE*, vol. 34, no. 5, pp. 254–256, May 1946.

[81] K. Sulonen, P. Suvikunnas, L. Vuokko, J. Kivinen, and P. Vainikainen, “Comparison of MIMO antenna configurations in picocell and microcell environments,” *IEEE J. Select. Areas Commun.*, vol. 21, no. 5, pp. 703–712, June 2003.

[82] S. Wyne, P. Almers, G. Eriksson, J. Karedal, F. Tufvesson, and A. F. Molisch, "Outdoor to indoor office MIMO measurements at 5.2 GHz," in *Proc. 60th IEEE Veh. Tech. Conf. 2004 (VTC 2004 Fall)*, vol. 1, pp. 101–105, Los Angels, CA, Sep. 2004.

[83] P. Almers, F. Tufvesson, P. Karlsson, and A. F. Molisch, "The effect of horizontal array orientation on MIMO channel capacity," in *Proc. 57th IEEE Veh. Tech. Conf. 2003 (VTC 2003 Spring)*, vol. 1, pp. 34–38, Jeju, Korea, Apr. 2003.

[84] A. F. Molisch, M. Steinbauer, M. Toeltsch, E. Bonek, and R. S. Thomä, "Capacity of MIMO systems based on measured wireless channels," *IEEE J. Select. Areas Commun.*, vol. 20, no. 3, pp. 561–569, Apr. 2002.

[85] A. Pal, C. M. Tan, and M. A. Beach, "Comparison of MIMO channels from multipath parameter extraction and direct channel measurements," in *Proc. 14th Int. Symp. Personal, Indoor and Mobile Radio Commun. 2004 (PIMRC 2004)*, vol. 3, pp. 1574–1578, Barcelona, Spain, Sep. 2004.

[86] R. Vaughan, and J. B. Andersen, *Channels, Propagation and Antennas for Mobile Communications.* London: The IEE, 2003.

[87] K. Takizawa, S. Fujita, Y. Rikuta, K. Hamaguchi, and R. Kohno, "Measurement based performane evaluation of a 26 GHz band UWB communication system," in *Proc. 64th IEEE Veh. Tech. Conf. 2006 (VTC 2006 Fall)*, Montreal, Canada, RAT14–3, Sep. 2006.

[88] J. Keignart, C. Abou-Rjeily, C. Delaveaud, and N. Daniele, "UWB SIMO channel measurements and simulations," *IEEE Trans. Microwave Theory Tech.*, vol. 54, no. 4, pp. 1812–1819, Apr. 2006.

[89] C. Ribeiro, A. Richter, and V. Koivunen, "Stochastic maximum likelihood estimation of angle- and delay domain propagation parameters," in *Proc. 16th Int. Symp. Personal Indoor and Mobile Radio Commun. (PIMRC '05)*, C05–05, Berlin, Germany, Sep. 2005.

[90] A. Kainulainen, L. Vuokko, and P. Vainikainen, "Polarization behavior in different urban radio environments at 5.3 GHz," TD(05)018, Bologna, Italy, Jan. 2005.

AppendixI

COST273 MIMO Channel Model Parameters in Home Environments

The propagation modeling results derived by our mesurement campaigns were approved as a representative channel parameter of home environments in the COST273 MIMO channel model. The parameters constituting the channel model can be classified into the following two categories:

1. External parameters

   This parameter specifies general properties of the environment under consideration. Antenna position, room size, and path loss are categorized in this parameter. Throughout a simulation run, this value is kept fixed.

2. Stochastic parameters

   This parameter includes properties of 1) shadowing, 2) power of LOS path, 3) cluster parametes, such as the number of clusters, cluster motion, cluster angular/delay spread, and cluster coupling factor between link ends, 4) diffuse components, 5) polarization, and 6) auto-correlation distances. Most of these parameters are defined by probability density functions (PDF), and parameters are generated using the PDF in each realization of propagation channels.

In the following, the derived parameters are summarized. Parameters in LOS and NLOS scenarios are shown in Tables I.1 to I.5 and Tables I.6 to I.10, respectively. Detailed description of the MIMO stochastic channel model should be referred to [66].

The parameter list is still not complete, since some channel parameters were not able to be analyzed by the measured data taken in our channel sounding. Some parameters which were not available from our measurement results were complemented with results from other measurements and channel models, such as the one reported by Kainulainen et al. [90], IEEE802.15.4a channel model [64], and COST259 channel model [69]. Parameters

Table I.1 External parameters in LOS scenario.

Parameter	Values and comments
f_c [Hz]	6.85×10^9 (Note: UWB measurements covering from 3.1 to 10.6 GHz)
h_{BS} [m]	1.3
h_{MS} [m]	1.0
$\overrightarrow{r}_{\mathrm{BS}}$ [m]	[0.0, 0.0, 1.3]
$\overrightarrow{r}_{\mathrm{MS}}$ [m]	[5.0, 0.0, 1.0]
N_{ant}, d_{ant}, $\overrightarrow{r}_{\mathrm{array}}$ [.,m,m]	BS: 4 element ULA MS: 4×4 horizontal URA Inter-element spacing: 0.048 [m]
ϕ_{ant} [pdf]	A uniform distribution over $[0, 2\pi]$
P_{L} [dB]	$P_L(d,f) = 43.9 + 17.9\log_{10}(d) + 22.4\log_{10}\left(\frac{f}{f_{\mathrm{c}}}\right)$, where d is distance between Tx to Rx [64]
A_{room} [m×m]	6.85×3.6
N_{floor}	0
ρ_{refl} [dB]	yes

for path loss, shadowing, and polarizations were complemented from the literatures. The auto-correlation distances represent the dynamic properties of propagation channels, but we were neither able to analyze it using our measured data, nor find complemental parameters in other measurement and modeling results. It is obvious that further UWB double directional channel sounding and propagation modeling is necessary to supply values for the empty parameters.

Table I.2 Stochastic parameters in LOS scenario.

Parameter	Values and comments
visibility region	
$pdf_{\text{cluster}}(n)$	7
R_{C} [m]	2 (Educational guess)
L_{C} [m]	0.5 (Educational guess)
cluster movement	
$\mu_{\text{C},v}$ [m/s]	0 optional: up to 4 [m/s]
$\sigma_{\text{C},v}$ [dB]	0
cluster power	
k_τ [dB/ns]	0.20
τ_{B} [ns]	50
Line of sight	
d_{co} [m]	10
R_{L} [m]	2 (Educational guess)
L_{L} [m]	0.5 (Educational guess)
μ_{K} [dB]	-2.1
σ_{K} [dB]	3 [69]
average number of clusters	7
marginal DOA pdf	N/A (Number of samples was too small.)
marginal DOD pdf	N/A (Number of samples was too small.)
pdf of the delay of clusters	$p(T_l \vert T_{l-1}) = \Lambda \exp\{-\Lambda(T_l - T_{l-1})\}$ (Poisson Process) T_l is a delay time of l-th cluster, $\Lambda = 0.047$ [64]
number of MPCs per cluster	3 to 13 (average: 8)
pdf of the power distribution of the MPCs within cluster	$p(x) = \frac{1}{\sqrt{2\pi}\sigma} \exp\{-\frac{(x-m)^2}{2\sigma^2}\}$ $(x < 0)$ Log-normal distribution, $m = -9.54$, $\sigma = 5.26$ [dB]. Power is normalized by the strongest path in clusters, i.e., 0 dB path always exists.
percentage of power in the diffuse radiation [dB]	-6.38 (Compared to the total received power)
PDP of the diffuse radiation	$f_{\text{diff}} = P_0 \exp(-\frac{\tau}{\Gamma_{\text{diff}}})$ P_0: 33 dB smaller power of the LOS path $\Gamma_{\text{diff}} = 10.9$, τ [ns] in excess delay.

Table I.3 Stochastic parameters for angular spread, delay spread, and shadowing in LOS scenario.

Parameter	Values and comments
delay spread	
μ_τ [ns]	0.98
σ_τ [dB]	-2.85
angular spread at BS	
$\mu_{\phi\mathrm{BS}}$ [°]	3.35
$\sigma_{\phi\mathrm{BS}}$ [dB]	2.54
$\mu_{\theta\mathrm{BS}}$ [°]	8.76
$\sigma_{\theta\mathrm{BS}}$ [dB]	5.84
angular spread at MS	
$\mu_{\phi\mathrm{MS}}$ [°]	3.35
$\sigma_{\phi\mathrm{MS}}$ [dB]	2.54
$\mu_{\theta\mathrm{MS}}$ [°]	8.76
$\sigma_{\theta\mathrm{MS}}$ [dB]	5.84
shadowing	
σ_S [dB]	2.22 [64]
autocorrelation distances	
L_S [m]	N/A
L_τ [m]	N/A
$L_{\phi\mathrm{BS}}$ [m]	N/A
$L_{\theta\mathrm{BS}}$ [m]	N/A
$L_{\phi\mathrm{MS}}$ [m]	N/A
$L_{\theta\mathrm{MS}}$ [m]	N/A
cross-correlations	
ρ	N/A
$\rho_{\mathrm{BS-BS}}$	N/A

Table I.4 Parameters for polarization in LOS scenario.

Parameter	Values and comments
μ_{XPD} [dB]	5
σ_{XPD} [dB]	2.5
μ_{VVHH} [dB]	0.6
σ_{VVHH} [dB]	2.5 (Educational guess from [90])
μ_{VHHV} [dB]	0.5
σ_{VHHV} [dB]	2.5 (Educational guess from [90])

Table I.5 Parameters for MIMO in LOS scenario.

Parameter	Values and comments
N_{discr} [.]	100
$\sigma_{\text{P\_path}}$ [dB]	N/A
p_{power} [pdf]	N/A
Q_{diff} [dB]	-5.25 (Diffuse power divided by the power of discrete propagation paths)
$f_{\text{diff}}(\tau, \phi_{\text{BS}}, \theta_{\text{BS}}, \phi_{\text{MS}}, \theta_{\text{MS})}$	$f_{\text{diff}} = P_0 \exp{(-\frac{\tau}{\Gamma_{\text{diff}}})}$ P_0: 33 dB smaller power of the LOS path $\Gamma_{\text{diff}} = 10.9$, τ [ns] in excess delay.
coupling matrix	
N_{nz} [.]	1 or 2
f_{coupl}	$\begin{array}{ccccccc} 1 & 0 & 0 & 0 & 0 & 0 & 0 \\ 0 & 1 & 0 & 0 & 0 & 0 & 0 \\ 0 & 0 & 1 & 0 & 0 & 0 & 0 \\ 0 & 0 & 0 & 1 & 0 & 0 & 0 \\ 0 & 0 & 0 & 0 & 1 & 0 & 0 \\ 0 & 0 & 0 & 0 & 0 & 0.85 & 0.15 \end{array}$ (Typical value)
temporal variations for ad-hoc	
$Q_{\text{temp\_rice}}$ [pdf]	N/A

Table I.6 External parameters in NLOS scenario.

Parameter	Values and comments
f_c [Hz]	6.85×10^9 (Note: UWB measurements covering from 3.1 to 10.6 GHz)
h_{BS} [m]	1.3
h_{MS} [m]	1.0
$\overrightarrow{r}_{\text{BS}}$ [m]	[0.0, 0.0, 1.3]
$\overrightarrow{r}_{\text{MS}}$ [m]	[5.0, 0.0, 1.0]
N_{ant}, d_{ant}, $\overrightarrow{r}_{\text{array}}$ [.,m,m]	BS: 4 element ULA MS: 4×4 horizontal URA Inter-element spacing: 0.048 [m]
ϕ_{ant} [pdf]	A uniform distribution over $[0, 2\pi]$
P_{L} [dB]	$P_L = 48.7 + 45.8 \log_{10}(d) + 30.6 \log_{10}\left(\frac{f}{f_{\text{c}}}\right)$, where d is distance between Tx to Rx [64]
A_{room} [m×m]	6.85×3.6
N_{floor}	0
ρ_{refl} [dB]	yes

Table I.7 Stochastic parameters in NLOS scenario.

Parameter	Values and comments
visibility region	
$pdf_{\mathrm{cluster}}(n)$	8 (Typical value)
R_{C} [m]	2 (Educational guess)
L_{C} [m]	0.5 (Educational guess)
cluster movement	
$\mu_{\mathrm{C},v}$ [m/s]	0 optional: up to 4 [m/s]
$\sigma_{\mathrm{C},v}$ [dB]	0
cluster power	
k_τ [dB/ns]	0.18
τ_{B} [ns]	55
Line of sight	
d_{co} [m]	–
R_{L} [m]	–
L_{L} [m]	–
μ_{K} [dB]	–
σ_{K} [dB]	–
average number of clusters	8
marginal DOA pdf	N/A (Number of samples was too small.)
marginal DOD pdf	N/A (Number of samples was too small.)
pdf of the delay of clusters	$p(T_l \mid T_{l-1}) = \Lambda \exp\{-\Lambda(T_l - T_{l-1})\}$ (Poisson Process) T_l is a delay time of l-th cluster, $\Lambda = 0.12$ [64]
number of MPCs per cluster	2 to 23 (average: 7)
pdf of the power distribution of the MPCs within cluster	$p(x) = \frac{1}{\sqrt{2\pi}\sigma} \exp\{-\frac{(x-m)^2}{2\sigma^2}\}$ $(x < 0)$ Log-normal distribution, $m = -9.54$, $\sigma = 5.26$ [dB]. Power is normalized by the strongest path in clusters, i.e., 0 dB path always exists.
percentage of power in the diffuse radiation [dB]	-5.50 (Compared to the total received power)
PDP of the diffuse radiation	$f_{\mathrm{diff}} = P_0 \exp\left(-\frac{\tau}{\Gamma_{\mathrm{diff}}}\right)$ P_0: 38 dB smaller power of the LOS path $\Gamma_{\mathrm{diff}} = 12.4$, τ [ns] in excess delay.

Table I.8 Stochastic parameters for angular spread, delay spread, and shadowing in NLOS scenario.

Parameter	Values and comments
delay spread	
μ_τ [ns]	0.88
σ_τ [dB]	-3.11
angular spread at BS	
$\mu_{\phi \mathrm{BS}}$ [°]	4.52
$\sigma_{\phi \mathrm{BS}}$ [dB]	5.07
$\mu_{\theta \mathrm{BS}}$ [°]	6.07
$\sigma_{\theta \mathrm{BS}}$ [dB]	4.86
angular spread at MS	
$\mu_{\phi \mathrm{MS}}$ [°]	4.52
$\sigma_{\phi \mathrm{MS}}$ [dB]	5.07
$\mu_{\theta \mathrm{MS}}$ [°]	6.07
$\sigma_{\theta \mathrm{MS}}$ [dB]	4.86
shadowing	
σ_S [dB]	3.51 [64]
autocorrelation distances	
L_S [m]	N/A
L_τ [m]	N/A
$L_{\phi \mathrm{BS}}$ [m]	N/A
$L_{\theta \mathrm{BS}}$ [m]	N/A
$L_{\phi \mathrm{MS}}$ [m]	N/A
$L_{\theta \mathrm{MS}}$ [m]	N/A
cross-correlations	
ρ	N/A
$\rho_{\mathrm{BS-BS}}$	N/A

Table I.9 Parameters for polarization in NLOS scenario.

Parameter	Values and comments
μ_{XPD} [dB]	5
σ_{XPD} [dB]	2.5
μ_{VVHH} [dB]	0.6
σ_{VVHH} [dB]	2.5 (Educational guess from [90])
μ_{VHHV} [dB]	0.5
σ_{VHHV} [dB]	2.5 (Educational guess from [90])

Table I.10 Parameters for MIMO in NLOS scenario.

Parameter	Values and comments
N_{discr} [.]	100
$\sigma_{\text{P\_path}}$ [dB]	N/A
p_{power} [pdf]	N/A
Q_{diff} [dB]	−4.06 (Diffuse power divided by the power of discrete propagation paths)
$f_{\text{diff}}(\tau, \phi_{\text{BS}}, \theta_{\text{BS}}, \phi_{\text{MS}}, \theta_{\text{MS})}$	$f_{\text{diff}} = P_0 \exp{(-\frac{\tau}{\Gamma_{\text{diff}}})}$ P_0: 38 dB smaller power of the LOS path $\Gamma_{\text{diff}} = 12.4$, τ [ns] in excess delay.
coupling matrix	
N_{nz} [.]	1 or 3
f_{coupl}	$\begin{matrix} 1 & 0 & 0 & 0 & 0 & 0 & 0 & 0 \\ 0 & 1 & 0 & 0 & 0 & 0 & 0 & 0 \\ 0 & 0 & 1 & 0 & 0 & 0 & 0 & 0 \\ 0 & 0 & 0 & 1 & 0 & 0 & 0 & 0 \\ 0 & 0 & 0 & 0 & 1 & 0 & 0 & 0 \\ 0 & 0 & 0 & 0 & 0 & 0.56 & 0.31 & 0.13 \end{matrix}$ (Typical value)
temporal variations for ad-hoc	
$Q_{\text{temp\_rice}}$ [pdf]	N/A

AppendixII

List of Publications and Awards

Journal Papers

K. Haneda, J. Takada, and T. Kobayashi, “Cluster properties investigated from a series of ultra wideband double directional propagation measurements in home environments,” *IEEE Trans. Antennas Propagat.*, vol. 54, no. 12, pp. 3778–3788, Dec. 2006.

———, “A parametric UWB propagation channel estimation and its performance validation in an anechoic chamber,” *IEEE Trans. Microwave Theory Tech.*, vol. 54, no. 4, pp. 1802–1811, Apr. 2006.

———, “Double directional ultra wideband channel characterization in a line-of-sight home environment,” *IEICE Trans. Fundamentals*, vol. EA–88, no. 9, pp. 2264–2271, Sep. 2005.

International Conferences

K. Haneda, J. Takada, and T. Kobayashi, “Applicability of UWB double directional propagation modeling for evaluating UWB transmission performance,” in *IEEE 65th Vehicular Technology Conference (VTC 2007 Spring)*, Dublin, Ireland, Apr. 2007, accepted.

———, “Double directional cluster properties investigated from a series of UWB propagation channel measurements in home environments,” in *Proc. XXVIIIth URSI General Assembly*, F03–1, New Delhi, India, Nov. 2005.

———, “Double directional LOS channel characterization in a home environment with ultra wideband signal,” in *Proc. 7th Int. Symp. Wireless and personal and Multimedia Commun. 2004 (WPMC 04),* pp. 214–218, Abano Therme, Italy, Sep. 2004.

———, “Clusterization analysis of spatio-temporal UWB radio channel for line-of-sight and non-line-of-sight indoor home environments,” in *Proc. Joint COST273/284 Workshop on Antennas and Related System Aspects in Wireless Commun.,* pp. 123–128, Gothenburg, Sweden, June 2004.

———, “Experimental evaluation of a SAGE algorithm for ultra wideband channel sounding in an anechoic chamber,” in *Proc. Int. Workshop on Ultra Wideband Systems Joint with Conf. on Ultra Wideband Systems and Technologies (Joint UWBST & IWUWBS 2004)*, pp. 66–70, Kyoto, Japan, May 2004.

K. Haneda and J. Takada, “An application of SAGE algorithm for UWB propagation channel estimation,” in *Proc. IEEE Conf. Ultra Wideband Systems and Technologies (UWBST 2003)*, pp. 483–487, Reston, VA, USA, Nov. 2003.

Contribution to Channel Modeling Activities

COST273 Channel Model

K. Haneda, J. Takada, and T. Kobayashi, “On the cluster properties in UWB spatio-temporal residential meaasurements,” presented in *COST273 12th Management Committee Meeting,* TD(05)66, Bologna, Italy, Jan. 2005.

———, “Double directional ultra widenband channel characterization in a line-of-sight home environment,” presented in *COST273 11th Management Committee meeting*, TD(04)160, Duisburg, Germany, Sep. 2004.

———, “An application of SAGE algorithm for UWB propagation channel estimation,” presented in *COST273 8th Management Committee Meeting,* TD(03)182, Prague, Czech Republic, Sep. 2003.

IEEE 802.15.4a Channel Model

K. Haneda, J. Takada, and T. Kobayashi, “Spatio-temporal UWB propagation channel characterization,” IEEE 802.15-04-0112-01-004a, Orlando, FL, USA, Mar.

2004.

Domestic Conferences (all in Japanese)

K. Haneda, J. Takada, and T. Kobayashi, “Applicability of UWB double directional propagation modeling for evaluating UWB transmission performance,” IEICE Tech. Rep., WBS2006–27, Oct. 2006.

———, “A hybrid deterministic and stochastic double directional channel model for indoor radio wave propagation,” IEICE Society Conf., AS–1–7, Sep. 2005.

———, “Representative channel parameters extracted from a series of ultra wideband propagation experiments in a Japanese wooden house,” IEICE General Conf., ABS–1–7, Mar. 2005.

———, “Spatio-temporal characterization of line-of-sight and room-to-room propagation in home environments with ultra wideband signal,” URSI-F Meeting, Mar. 2004.

———, “Experimental evaluation of a UWB channel sounding system in an anechoic chamber,” IEICE Tech. Rep., WBS2003–86, Dec. 2003.

K. Haneda and J. Takada, “A study on estimating UWB propagation channels,” IEICE Tech. Rep., WBS2003–42, July 2003.

Awards

Student Paper Award of 7th Int. Symp. Wireless, Personal and Multimedia Commun. 2004 (WPMC04), Sep. 2004.